Title

Simulation of Flow Control using Dielectric-Barrier-Discharge (DBD) Plasma Actuators

Author

Zhu, Zihao

Publication Date

2023

UNIVERSITY OF CALIFORNIA,
IRVINE

Simulation of Flow Control using Dielectric-Barrier-Discharge (DBD) Plasma Actuators

DISSERTATION

submitted in partial satisfaction of the requirements
for the degree of

DOCTOR OF PHILOSOPHY

in Mechanical and Aerospace Engineering

by

Zihao Zhu

Dissertation Committee:
Professor Feng Liu, Chair
Professor William Sirignano
Professor Dimitri Papamoschou

2023

DEDICATION

To my professor, colleagues, family and friends

TABLE OF CONTENTS

LIST OF FIGURES

LIST OF TABLES

ACKNOWLEDGMENTS

I would like to first thank my advisor Prof Feng Liu, for providing me with an amazing work environment. Without his patience and guidance, I could not successfully progress in my PhD research. His knowledge and vision guided me through the most difficult times.

I would also like to thank Prof Said Elgobashi for providing me with the SIMPLE algorithm, without which I could not simulate the flow field around a square cylinder.

Thank Suzen and Huang for providing me with the plasma body force model. This model allowed me to simulate the plasma effect as a source term and successfully coupled it with the Navier Stokes equation.

VITA

Zihao Zhu

EDUCATION

PhD in Mechanical and Aerospace Engineering **2023**
University of California-Irvine *Irvine, California*

Master of Science in Aerospace Engineering **2017**
University of Maryland-College Park *College Park, Maryland*

Bachelor of Engineering in Aerospace Engineering **2015**
Beihang University *Beijing, China*

RESEARCH EXPERIENCE

Using ANSYS to simulate the creeping process of a turbine blade **2015/01–2015/06**
Beihang University *Beijing, China*

Transforming an unstructured triangular mesh into an unstructured quadrilateral mesh **2016/09–2017/08**
University of Maryland-College Park *College Park, Maryland*

Simulating the flutter process of Windecker aircrafts **2018/09–2019/12**
University of California-Irvine *Irvine, California*

Simulating the flow around a square cylinder under plasma control **2019/12–2021/08**
University of California-Irvine *Irvine, California*

Simulating the flow around a circular cylinder under plasma control **2021/08–now**
University of California-Irvine *Irvine, California*

TEACHING EXPERIENCE

Teaching Assistant **2019–now**
University of california-Irvine *Irvine, california*

List of courses:
Introduction to Fluid Mechanics
Viscous and compressible Flow
Compressible Flow
Introduction to Thermodynamics
Applied Engineering Thermodynamics

REFEREED JOURNAL PUBLICATIONS

Flow around a circular cylinder controlled by asymmetric plasma actuation — **In preparation**
Physics of Fluids Journal

Numerical simulation of the flow around a square cylinder under plasma actuator control — **2021**
Physics of Fluids Journal

REFEREED CONFERENCE PUBLICATIONS

Quad-gen: An indirect method to create all- quadrilateral grids — **2019**
AIAA Scitech

ABSTRACT OF THE DISSERTATION

Simulation of Flow Control using DBD Plasma Actuators

by

Zihao Zhu

Doctor of Philosophy in Mechanical and Aerospace Engineering

University of California, Irvine, 2023

Professor Feng Liu, Chair

The Dielectric Barrier Discharge (DBD) plasma actuator is a commonly used flow control device. This device is capable of ionizing air using a high-frequency and high-voltage AC power source, creating positive ions and negative electrons. The ions travel in the direction of the external electric field, inducing a jet along the wall. This jet can delay the boundary layer separation, increase the lift-to-drag ratio, and suppress the fluctuations in the wake. The DBD plasma actuator has many advantages, such as ease of installation, fast-acting capabilities, and high energy efficiency. Additionally, it requires no moving mechanical parts, making it one of the most efficient active control methods. While numerous papers have studied the application of the plasma actuator, only a few have explored its fundamental physics and the detailed mechanisms responsible for its flow control effectiveness. This research is divided into two parts. The first part examines the fundamental physics behind the ionization process, investigating how plasma is created by the high-power and high-frequency AC power source. The second part delves into the fundamental physics of plasma control on flat plates and conical bodies. In this research, the plasma effect is simulated by a mathematical model and treated as a source term when coupled with the 2D Navier-Stokes equations. This model has some parameters that require calibration based on

experimental results.

The first case examines the plasma-induced flow field on a flat plate under duty-cycle control. In this scenario, a single DBD plasma actuator is installed on the surface of a flat plate. The air is initially quiescent and the flow field is solely induced by the plasma actuator. In this case, essential parameters are obtained for the plasma body force model through calibration with available experimental data, thereby providing a fully-developed model. The simplicity of this case makes it perfect for the calibration process.

The second case examines the flow field around a square cylinder under plasma control, where a pair of DBD plasma actuators are installed on different parts of the square cylinder. The fully developed plasma model is integrated into the SIMPLE algorithm as a source term. During the simulation, the incoming flow velocity is always set to $1m/s$, and the flow fields at $Re = 100$ and $Re = 200$ are simulated under three different installation configurations. In the first configuration, a pair of plasma actuators is installed on the front surface of the cylinder, generating two induced jets moving away from each other. In the second configuration, one actuator is placed on the top while another one is installed on the bottom of the cylinder, inducing two jets in the stream wise direction. In the third configuration, a pair of plasma actuators is installed on the rear surface of the cylinder, with two jets moving toward each other. After detailed analysis, we found that the third configuration produces the best flow control results, completely suppressing lift fluctuations and significantly reducing the time-averaged drag coefficient when the plasma body force is strong enough.

In the third case, the plasma effect is simulated using a self developed plasma body force model, while the flow field is simulated by solving the Reynolds-Averaged Navier-Stokes (RANS) Equations with the Spalart-Allmaras (SA) one-equation turbulence model. This case is divided into three steps. In the first step, a new plasma body force model tailored for circular surfaces is developed to replicate the experimental flow field around a circular cylinder. In the second step, the flow fields under different steady-state actuation signals are simulated and the results are analyzed in detail. In the third step, the flow fields

under unsteady actuations with varying duty-cycle frequencies and duty-cycle ratios are simulated. For both steady and unsteady actuation, the simulation results are compared with available experimental data. In addition to the findings reported in Hui's 2022 experiment, the simulation results unveil three significant new discoveries. First, the friction force on the surface of the circular cylinder responds instantly to the plasma actuation signal, whereas the momentum of the flow within the measurement window exhibits a time delay. Second, the momentum in the cross-stream direction forms an arc-like shape during one duty-cycle period, while the momentum in the streamwise direction remains relatively constant. Third, the time-accurate momentum exhibits only one peak within a duty-cycle period, while the pressure and friction forces exhibit multiple peaks. Furthermore, the magnitude of the pressure force greatly surpasses that of the friction force.

Chapter 1

Introduction

1.1 Background of Flow Control

Flow control plays a significant role in modern technology, with applications including boundary layer separation delay, lift-to-drag ratio increase, noise cancellation, and de-icing. There are two types of flow control methods: passive control and active control. Passive control typically involves modifying the geometry of a structure, while active control is achieved by adding an actuator to the surface of the structure. Active control systems usually require an energy input and an actuation signal. They can be further categorized into two types: predetermined control and interactive control. In predetermined control, an actuation signal is applied to the actuator without considering the state of the flow field. In interactive control, there are two subcategories: feed forward control and feedback control. In a feed forward control system, a sensor is typically placed upstream of the actuator, and the actuation signal is adjusted based on predicted results. In a feedback control system, a sensor is usually positioned downstream of the actuator and the measured outputs are compared with the desired outputs. If the output deviates from the desired values, the actuation signal is

adjusted to minimize the difference between the actual and planned output.

There are two ways to study flow control, simulation methods and experimental methods. In the past, experimental methods have been the most common way to study flow control. Lately, due to the rise of computational power, more and more simulation studies have been conducted as well. Comparing to experimental studies, simulation studies have many unique advantages such as being cheaper, safer and not being limited by lab space or experimental equipment. They can also simulate parameters that are hard to directly measure experimentally, such as the velocity field in the vicinity of the wall, the pressure field away from the wall, and the body force field. When conducted properly, simulation methods can also have much higher resolutions compared to experimental methods.

1.1.1 Passive Flow Control

The most effective passive control methods include vortex generators[1], porous interfaces[2] and bilateral splitter plates[3]. Figure 1.1 shows an example of a vortex generator, which is usually designed to delay the separation point on the surface of an airfoil. Due to the viscous dissipation in the boundary layer, the kinetic energy in the free stream is much higher than the kinetic energy inside the boundary layer. The vortex generator can create vortices that are able to mix the high energy fluid in the free stream with the low energy fluid in the boundary layer, thus putting more kinetic energy into the boundary layer. Due to the increased kinetic energy in the boundary layer, flow separation can only occur further downstream where the adverse pressure gradient is stronger. This device can keep the boundary layer attached to the surface of the geometry for a longer distance.

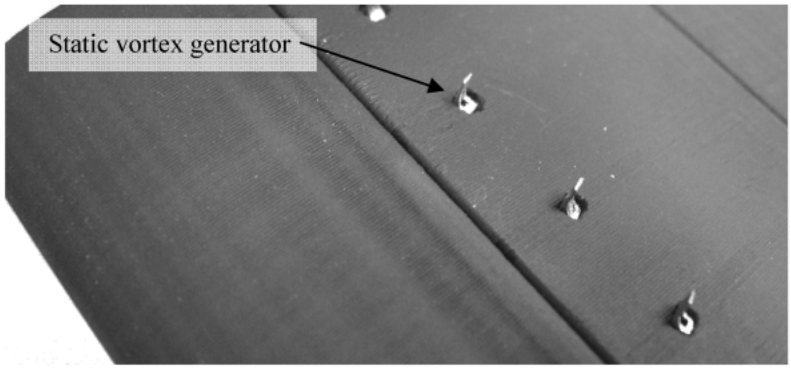

Figure 1.1: Photo of a vortex generator[1]

Another commonly employed method is the porous interface, as demonstrated by Bruneau and Mortazavi[2] in their study of flow control around a square cylinder. In this paper, a porous material was inserted between the cylinder surface and the surrounding flow field. This porous interface served to separate the flow field from the cylinder surface and create an intermediate flow region that could help diminish the boundary layer effects. Since the boundary layer was a primary contributor to the formation of large vortices, reducing the influence of the boundary layer through the porous interface can effectively reduce wake oscillations. Figure 1.2 provides a sketch of the porous interface, which resembles a thin sheet of paper positioned between the solid surface and the flow field.

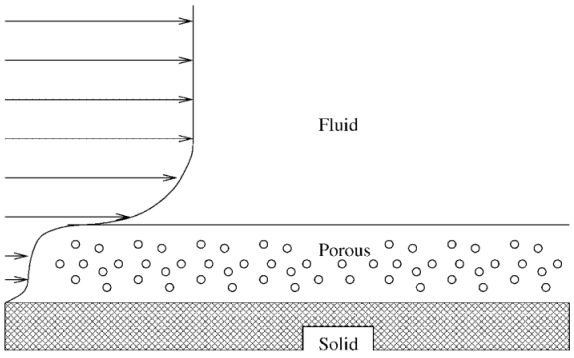

Figure 1.2: Structure of the porous interface[2]

Figure 1.3 shows the implementation of a splitter plate, which consists of two parallel plates

positioned at the leading and trailing edges of the circular cylinder in the direction of the incoming flow. This device can effectively suppress wake fluctuations and reduce drag forces on the circular cylinder. The underlying reason is that by installing a plate on the rear end of the cylinder, the shear layers previously separated from the cylinder surface reattach separately on top and bottom of the plate, unable to interact with each other. Without the mutual interaction between the wall jets from the top and bottom, the flow field will experience no major fluctuations.

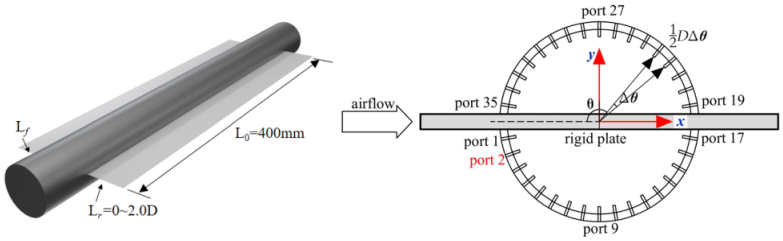

Figure 1.3: Bilateral splitter plate[3]

Although passive flow control devices can be very useful, they generally lack flexibility. In situations where the incoming flow field changes in time, they can be very insufficient because their flow control effects are solely dependent on their geometries, making it very hard to modify the control signals. To overcome these limitations, another type of flow control is studied, the active flow control method.

1.1.2 Active Flow Control

The most commonly used active control methods include the synthetic jet actuator[4], the Lorentz force actuator[5] and the DBD plasma actuator[6]. The synthetic jet actuator controls the flow field by generating high-frequency periodic wall jets which are fast-acting and easy to control. Many devices can be used to generate a wall jet, such as the fast-acting solenoid valve[7], the high-speed rotating siren valve[8] and the rotating orifice[9]. Despite

their usefulness, these devices usually require an external flow source, which can consume extra mass and energy. The synthetic jet actuator[4] developed by the Gerogia Institute of Technology, on the other hand, does not need external flow source.

Figure 1.4 shows a simple sketch of the synthetic jet actuator described above, where a moving plate is installed in a cavity. During its operation, the plate could move up and down rapidly, generating a series of vortices that could be used to manipulate the flow field. The biggest advantage of this jet actuator is its ability to use the air in the main flow stream instead of injecting additional air from an external source. The frequency of the plate oscillation depends on the external signal connected to the device, which gives the user plenty of freedom to manipulate the flow control signal.

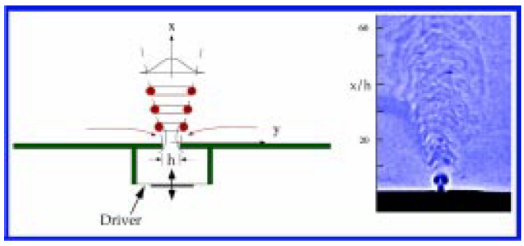

Figure 1.4: Sketch of a synthetic jet actuator[4]

Figure 1.5 shows a picture of the Piezoelectric flap actuator[10], which is usually used for oscillation suppression and noise cancellation. In this actuator, a thin layer of Piezoelectric (PZT) material is sandwiched between two electrodes. This thin layer is able to bend when a voltage is applied to the electrodes. With the help of a high quality feedback control system, the PZT layer is able to flap in accordance with the input signal, generating carefully controlled oscillations that are able to cancel out the incoming disturbances. Although this system is easy to install and fast-acting, there may be a large initial tilt angle due to thin-film stresses which could affect the effectiveness of flow control.

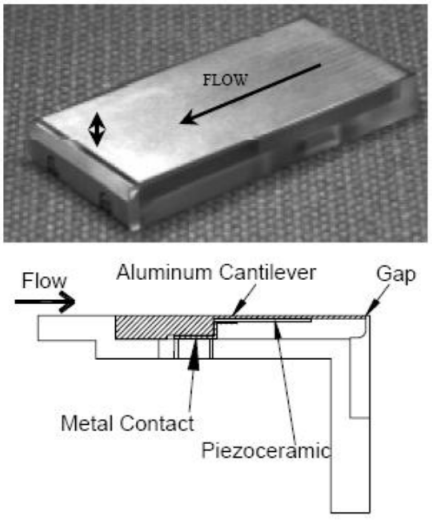

Figure 1.5: Monolithic piezoelectric flap actuator [10]

Both of the active flow control devices described above require moving mechanical parts. Although they are very useful, there is still some room for improvement. First, the movement of the components may not coincide with the input actuation signal due to the friction of air. Second, they can suffer from wear and tear after being used for a long period of time. A better option would be electro-magnetic actuators that do not need moving mechanical parts. The two most commonly used electro-magnetic actuators are the Lorentz force actuator[5] and the Dielectric-Barrier-Discharge (DBD) plasma actuator[11]. Figure 1.6 shows a schematic of the Lorentz force actuator, which uses a pair of sub-surface magnets to induce Lorentz force when conducting fluid moves on the top of the actuator. In this scenario, the moving flow on top of the actuator acts like a current in a magnetic field and the Lorentz force can generate vortices which are essential for flow control. Despite its effectiveness, this device also has some disadvantages. First, they only work for conducting fluids such as salt water. Second, the Lorentz force is a complicated 3D force whose direction is not always easy to determine. The DBD plasma actuator, on the other hand, generates a simple electric force in the stream-wise direction, making flow control much easier. Since it is able to ionize the air and generate weak plasma in its vicinity, it can be used to control non-conducting fluid as

well. Due to these unique advantages, the DBD plasma actuator will be used in our research.

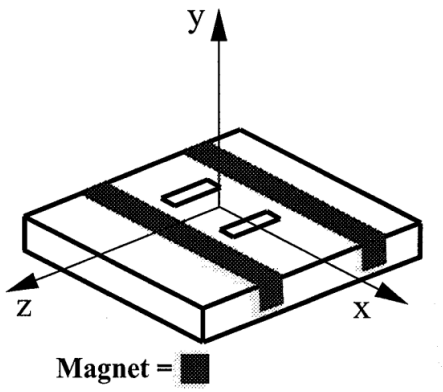

Figure 1.6: Lorentz force actuator[5]

1.2 Flow Control using the DBD Plasma Actuator

The DBD plasma actuator has several advantages, such as being small in weight, fast-acting capabilities, being fully electronic with no moving mechanical parts, not to mention it is very easy to install with no need for holes and cavities. During its operation, a high-voltage power source is applied between two electrodes, ionizing the air in the vicinity of the actuator and creating plasma. The electrodes can be connected to a direct current (DC) or an alternating current(AC) power source. For aerodynamic flow configurations, AC operation is usually preferred over DC operation due to its lower breakdown voltage and the lack of real current which may cause the erosion of electrodes. Figure 1.7 shows a sketch of the DBD plasma actuator under AC operation. The actuator consists of two electrodes, with one electrode exposed in air while the other one completely encapsulated beneath the dielectric surface. In this research, a high-voltage and high-frequency AC power source is connected to the exposed electrode while the buried electrode is always grounded.

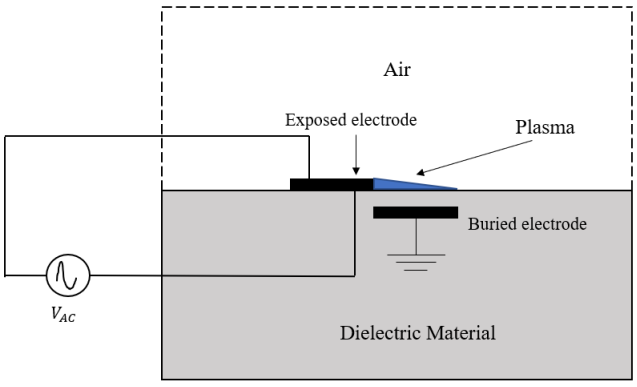

Figure 1.7: Sketch of a DBD plasma actuator [12]

There are two ways to operate the plasma actuator, the continuous actuation and the duty-cycle actuation. Under continuous actuation, the ions move in the direction of the electric field, coupling momentum to the air molecules and creating a wall jet. The induced wall jet

is very essential for flow control, such as delaying the separation point, increasing the lift and drag ratio and creating vortices in the flow field under certain conditions. Under the duty-cycle actuation, the carrier signal is modulated by an on-off switch with a duty-cycle ratio $\tau = \frac{T_{on}}{T}$ and a burst mode frequency f, as shown in Fig 1.8. The duty-cycle ratio is defined as the duration during which the plasma actuator is turned on, divided by the length of a duty-cycle period. Many simulations and experiments have shown that the burst-mode actuation is usually more efficient than steady-state actuation due to its ability to achieve better results using less energy.

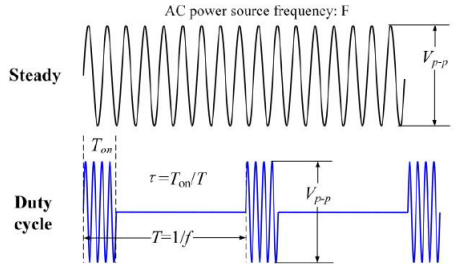

Figure 1.8: Steady-state and duty-cycle actuation[12]

Many studies have revealed the effectiveness of the DBD plasma actuator. Moralev et al.[13] studied the application of the DBD plasma actuator on laminar boundary layer. Huang and Zhang[14] studied the application of stream-wise and span-wise plasma actuators for cavity noise control. Wang et al.[15] did a research on the simulation of flow around a circular cylinder under plasma control. Singhal et al.[16] studied the plasma control of dynamic stall over a NACA0015 airfoil. Mazaheri et al.[17] simulated the plasma control effect on the improvement of wind turbines. For boundary layer separation control, Corke and Post[18] summarized the ability of the DBD plasma actuator to delay boundary layer separation on the surface of an airfoil. Figure 1.9 shows a sketch of the airfoil under plasma control, where the plasma actuator is installed on the leading edge. The plasma actuator is able to induce a jet running downstream on the suction side, adding kinetic energy into the boundary layer and delaying the separation point. Since aircraft stall is caused by the boundary layer

separation, delaying the separation point can increase the stall angle. This paper recorded the stall under different actuation signals. In the first case where the plasma actuator is turned off, the stall angle equals to 14°. In the second case where the plasma actuator operates in continuous actuation, the stall angle increases to 18°. In the third case where the plasma actuator operates in burst-mode actuation, the stall angle increases to 22°. These results not only validate the effectiveness of plasma control, but also validate the superiority of the burst-mode actuation.

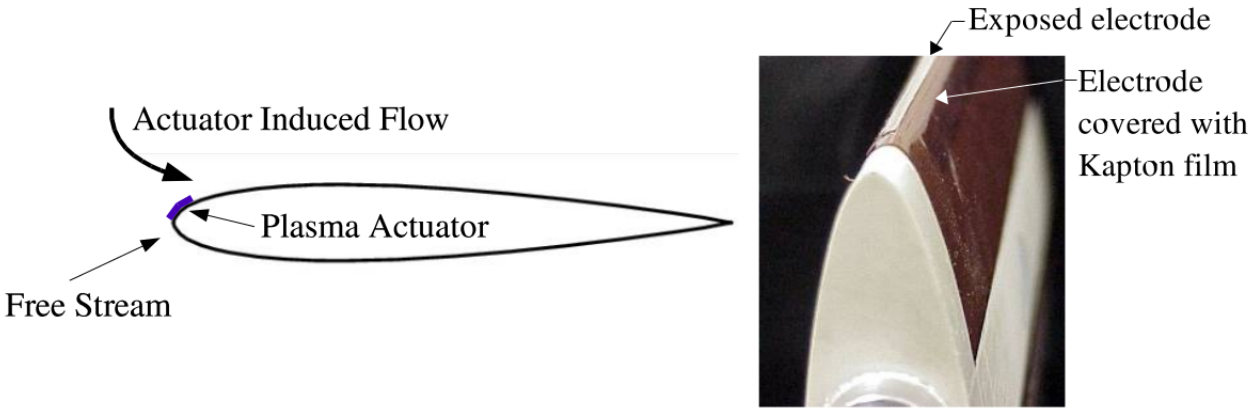

Figure 1.9: Plasma control on an airfoil[18]

The above papers demonstrated the effectiveness of plasma control in an open-loop system. To study the plasma control effect in a closed-loop system, Pasquale et al.[19] studied the flow separation prevention around a NACA0012 profile through multi-variable feedback controlled plasma actuators. He discovered that the closed-loop flow control can enhance the dynamic performance with less control effort and reduce the influence of disturbances due to the feedback loop's ability to react to disturbances in the flow. He also discovered that optimum control can be achieved when using two plasma actuators.

Due to the simplicity of its shape, the circular cylinder is the perfect geometry to study the effect of plasma control on aerodynamic performances. The cylinder wake under plasma control is studied by Jukes and Choi[20]. Figure 1.10 shows a sketch of the DBD plasma ac-

tuator installed at several locations on the surface of a circular cylinder. Several experiments have been conducted to study the effect of actuator location on the cylinder surface. Eventually, they discovered that the flow control effect is optimum when the plasma actuator is installed near the natural separation point. In the same year, Jukes and Choi[21] studied the flow around a circular cylinder controlled by the DBD plasma actuator under pulsed signals, where the plasma actuation signal is modulated by duty-cycle control. They discovered that the maximum suppression of flow oscillation occurred when the non-dimensional frequency $f^+ = 2.0$. They also discovered that the oscillation in the wake actually increased when the duty-cycle frequency equals to the natural vortex shedding frequency. These results show that both the actuator location and the actuation frequency are very important for plasma flow control around a circular cylinder.

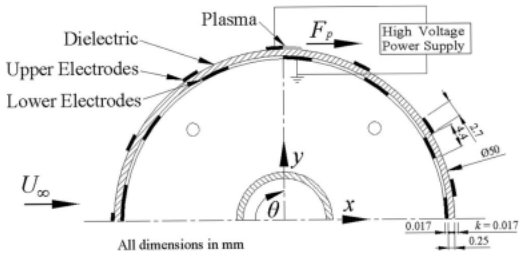

Figure 1.10: Plasma actuators around a circular cylinder[20]

Kopiev et al.[22] conducted an experimental study on noise cancellation in the flow field around a circular cylinder. The results demonstrated that upstream directed plasma actuators were able to reduce the noise around a circular cylinder by $10dB$. Furthermore, noise reduction was accompanied by significant reorganization of the wake behind a cylinder, decreasing both wake width and turbulence level.

All the papers mentioned above are focused on the application of plasma flow control. The papers that study the fundamental physics behind plasma control are relatively rare although they still do exist. Whalley and Choi[23] conducted an experiment to study the vortex propagation under continuous actuation. They discovered that the trajectory of the vortex

core is 31° with respect to the wall, and both the wall normal distance and the wall parallel distance traveled by the vortex core are linearly proportional to $t^{2/3}$. Xue et al.[12] used experimental methods to study the vortex generation and propagation under burst-mode actuation, where the vortices are observed by the PIV method. Figure 1.11 shows a sketch of the plasma induced vortex generation under burst-mode actuation, where one vortex is generated in a duty-cycle period. The vortices travel in the upper right direction, getting bigger and bigger along the way. This paper studied the effect of the duty-cycle frequency and the duty-cycle ratio on the vortex generation and propagation process. The results were presented below.

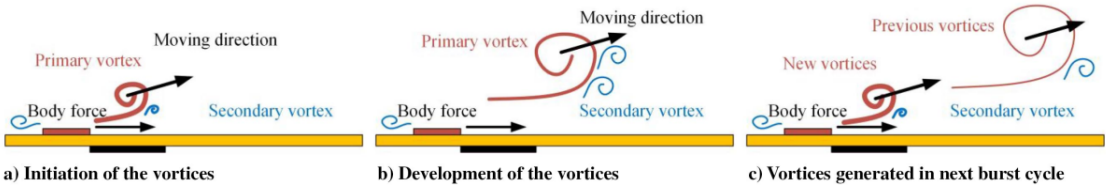

Figure 1.11: Vortex propagation on a flat plate[12]

Figure 1.12 shows the pictures of the vortex propagation process at $\tau = 0.5$. When the duty-cycle frequency $f = 30Hz$, two counter-clockwise vortices coexist in the picture frame, slowly dissipating due to the viscosity of air as they travel downstream. When the duty-cycle frequency $f = 50Hz$, there are three counter-clockwise vortices in the frame and the vortices are slightly smaller than those of lower frequencies. At higher frequencies, the distance between two consecutive vortices are smaller due to the duty-cycle period being shorter.

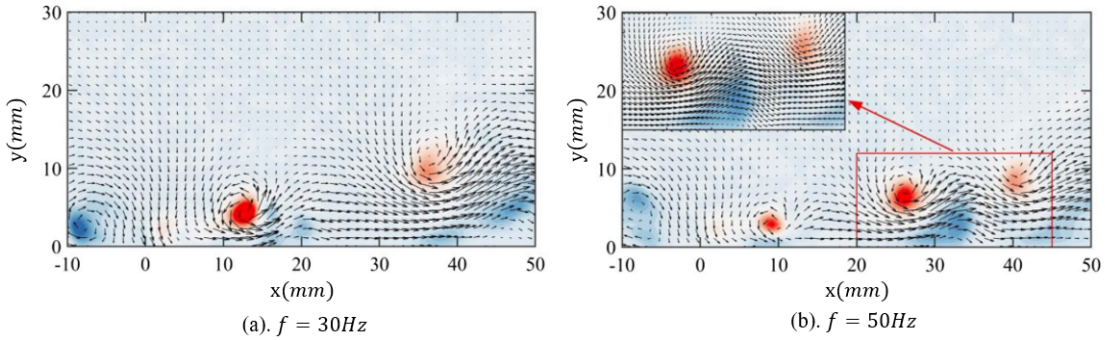

Figure 1.12: Photographs of the vortex train under different duty-cycle periods when $\tau = 0.5$ [12]

Apart from the qualitative results shown above, quantitative results are also studied by tracking the coordinates of vortex cores, which are defined as the point of maximum vorticity in a vortex. Figure 1.13 shows the trajectories of the vortex cores under different duty-cycle frequencies at $\tau = 0.5$. According to the figure, the angles between the vortex trajectories and the x-axis are bigger under lower frequencies. This is because the vortices are able to travel faster in the x-direction under higher frequencies. Since the propagation speed in the y-direction is not affected by the frequency, the angles for higher frequencies are smaller.

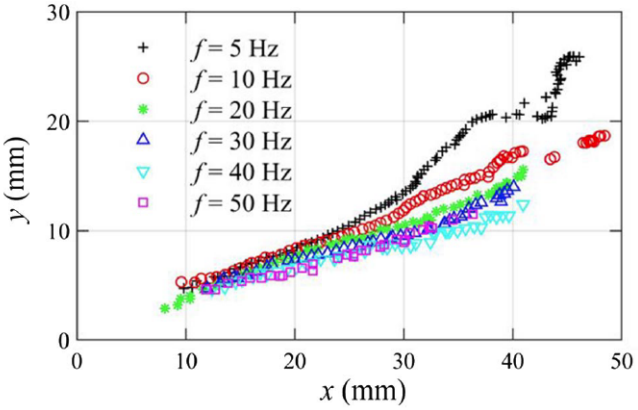

Figure 1.13: Trajectories of the vortex core at $\tau = 0.5$. [12]

Although the above experimental study revealed many cool facts about the fundamental physics behind flow control, there is still room for improvement due to the limitations of

the PIV method used in the experiment. This method struggles to observe the flow field near the wall effectively and faces challenges when dealing with small time scales due to limitations related to the high-frequency camera. In contrast, simulation methods offer a distinct advantage as they are not constrained by experimental limitations, allowing for a deeper investigation. Zhao et al.[24] used the flux reconstruction scheme to simulate the plasma induced flow field over a flat plate. Their simulations not only successfully replicated the experimental findings but also provided a significantly higher resolution, particularly near the wall. The simulated results were able to show much better results for time-accurate flow fields, especially at higher frequencies.

To study the fundamental physics of the plasma control on the flow field around a square cylinder, Anzai et al.[25] used numerical methods to simulate the flow field around a square cylinder controlled by a pair of DBD plasma actuators at $Re = 100$. The plasma effect is treated as a body force and simulated by Shyy's model[26]. This paper aims to study the flow control effects when the plasma actuators are installed in different locations. Figure 1.14 shows the location and direction of plasma induced wall jets on the surface of the square cylinder in three different cases. In Case 1, one actuator is installed on top of the cylinder while another one is installed on the bottom. In Case 2, two actuators are installed on the rear surface of the cylinder and the two induced jets are running into each other. In Case 3, two actuators are installed on the front surface and the two induced jets are running away from each other. In each case, the flow field is simulated and the time-accurate lift and drag coefficients are calculated. After careful analysis, it is discovered that Case 2 is the optimum case, where the oscillations in the wake can be successfully suppressed when the input power is sufficiently high. The time-averaged drag coefficient is also reduced significantly under this case.

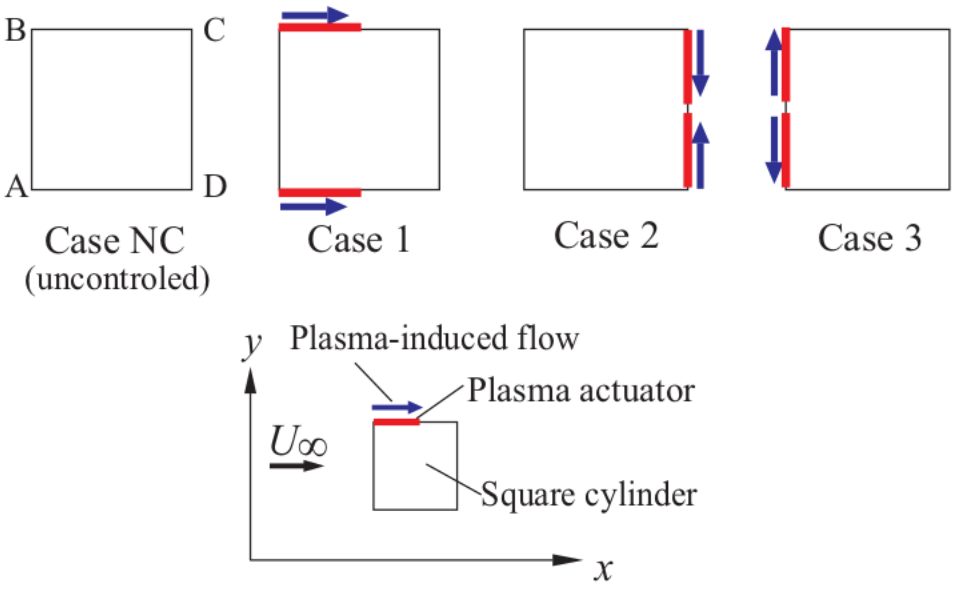

Figure 1.14: The location and arrangement of the plasma actuators

1.3 Goal of the research

We worked on three projects during my PhD study. In the first project, we simulated the plasma induced flow field over a flat plate, where one DBD plasma actuator was installed on the surface of a flat plate. Figure 1.15 shows a sketch of this case, where plasma is generated above the buried electrode due to ionization. This case served two purposes. First, some key parameters in the plasma body force model were obtained by calibrating with experimental results. Second, the vortex propagation process under duty-cycle plasma control were studied in more details comparing to Xue et al.'s experimental paper[12].

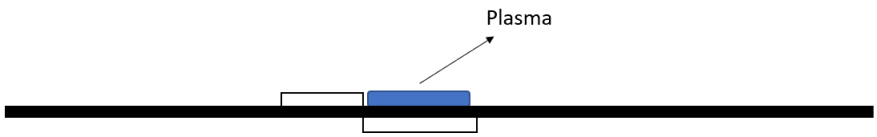

Figure 1.15: A DBD plasma actuator installed on a flat plate

In the second project, we simulated the flow around a square cylinder under plasma control, where a pair of plasma actuators were installed on the surface of a square cylinder. This project was broken into two steps. In the first step, the flow field around the square cylinder under different Reynolds numbers were simulated without any plasma control. The lift and drag coefficients for different Reynolds numbers were calculated and compared with experimental results for validation purposes. In the second step, the flow field around a square cylinder controlled by a pair of plasma actuators were studied in details. Figure 1.16 shows three different cases of plasma installation configurations. In Case 1, a pair of plasma actuators was installed on the front surface of the cylinder, and the wall jets were

running away from each other. In the second case, one actuator was installed on top of the cylinder while another one was installed on the bottom, and the induced jets were running downstream. In the third case, a pair of actuators was installed on the rear surface of the plasma actuator, and the induced jets were running into each other. This project studied the effect of the locations and strengths of the plasma actuator.

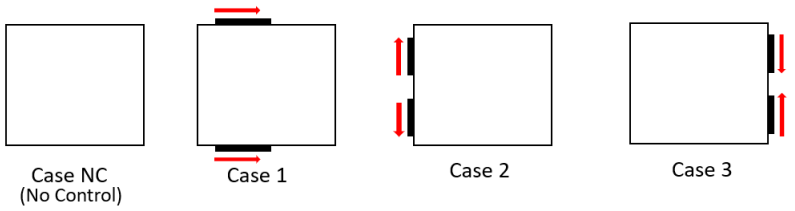

Figure 1.16: Plasma actuator arrangements in three cases

In the third project, we simulated the plasma induced flow field around a circular cylinder, where a pair of plasma actuators were installed on the left and right sides of the cylinder. The plasma actuator on the left was referred to as the port actuator while the plasma actuator on the right was referred to as the starboard actuator. During steady-state actuation, one or both of the plasma actuators were turned on continuously. During duty-cycle actuation, the port actuator was turned off while the starboard actuator was turned on and vice versa. Figure 1.17 shows the sketch of the flow field around a circular cylinder under plasma control, where a pair of actuators was installed on the left and right sides of the circular cylinder. In this project, the air was initially quiescent and the flow field was solely induced by the plasma actuators. The flow field under different actuation signals were studied both qualitatively and quantitatively.

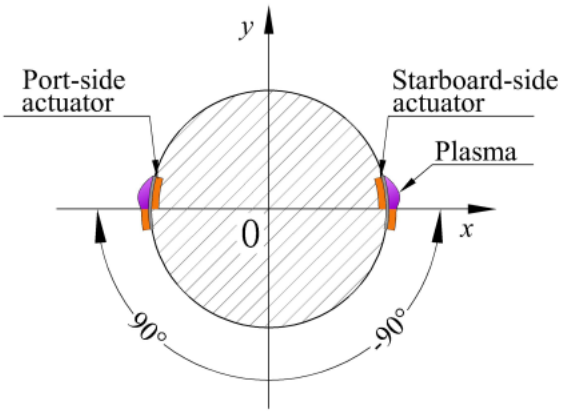

Figure 1.17: Circular cylinder models with plasma actuators [27]

Table 1.1 describes the three cases under steady-state actuation. In Case 1, the starboard actuator was always on while the port actuator was always off, corresponding to a duty-cycle ratio $\tau = 0.0$. In Case 2, the port actuator was always on while the starboard actuator was always off, corresponding to a duty-cycle ratio $\tau = 1.0$. In the third case, both actuators were always on and the plasma body forces were symmetric on both sides.

Case 1: $\tau = 0.0$	starboard-side actuation
Case 2: $\tau = 1.0$	port-side actuation
Case 3: Both-on	symmetric actuation

Table 1.1: Steady-state cases

Under duty-cycle actuation, the plasma body force was modulated using a square wave on-off switch. Table 1.2 provides details about the duty-cycle frequencies and ratios during unsteady actuation. For lower frequencies ($f = 1, 5, 10Hz$), we simulated five different duty-cycle ratios ranging from $\tau = 0.01$ to 0.99 at each frequency. For higher frequencies ($f = 40, 60, 100, 200Hz$), we only simulated three different duty-cycle ratios ranging from $\tau = 0.3$ to 0.7 at each frequency. We employed the dual time-stepping method, using 200 pseudo time steps within each physical time step. For duty-cycle ratios of $\tau = 0.01$ and 0.99,

we utilized 500 physical time steps within each duty-cycle period. For duty-cycle ratios of $\tau = 0.3, 0.5, 0.7$, we employed 130 time steps per period. Detailed results for each case can be found in Section 5.

f	τ
$1Hz$	0.01, 0.3, 0.5, 0.7, 0.99
$5Hz$	0.01, 0.3, 0.5, 0.7, 0.99
$10Hz$	0.01, 0.3, 0.5, 0.7, 0.99
$40Hz$	0.3, 0.5, 0.7
$60Hz$	0.3, 0.5, 0.7
$100Hz$	0.3, 0.5, 0.7
$200Hz$	0.3, 0.5, 0.7

Table 1.2: Duty-cycle frequencies and ratios for different unsteady cases

Chapter 2

Modeling of the DBD Plasma Actuator

2.1 Fundamental Physics behind the DBD Plasma Actuator

Before delving into the application of plasma flow control, a comprehensive summary of the fundamental physics behind the DBD plasma actuator is provided. Enloe et al.[28] conducted a series of experimental studies to investigate the fundamental physics of plasma actuation. Figure 2.1 illustrates the movement of ions and electrons during one AC period, which is comprised of two strokes: the forward stroke and the backward stroke. The voltage applied to the exposed electrode is negative during the forward stroke and positive during the backward stroke.

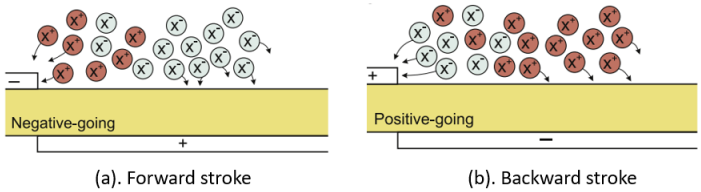

Figure 2.1: A sketch of the forward and backward discharge[29]

During the forward stroke, the exposed electrode experiences increasingly negative voltages, causing electrons to emit from the exposed electrode and land on the surface of the dielectric layer. In contrast, during the backward stroke, the exposed electrode undergoes increasingly positive voltages, and the electrons that accumulated on the dielectric surface return to the exposed electrode. Figure 2.2 provides high-speed photographs of the plasma discharge during the forward stroke (top) and the backward stroke (bottom), clearly illustrating the disparity in plasma distribution between the two strokes. In these images, the intensity of light emission serves as an indicator of plasma density, which is a reasonable assumption given the significant difference in timescales between the recombination time (on the order of 10^{-8} seconds)[30] and the discharge time (on the order of 10^{-3} seconds). The asymmetry between the two discharges can be attributed to the source of electrons. During the forward stroke, electrons originate from the exposed electrode, which essentially serves as an infinite source of readily available electrons, resulting in a continuous discharge. During the backward stroke, electrons come from the dielectric surface and they do not come off as easily. Consequently, electrons come in the form of fewer but larger micro-discharges during this stroke. This asymmetry between the two strokes is also supported by the models presented by Boeuf et al.[31] and Enloe et al.[32, 33].

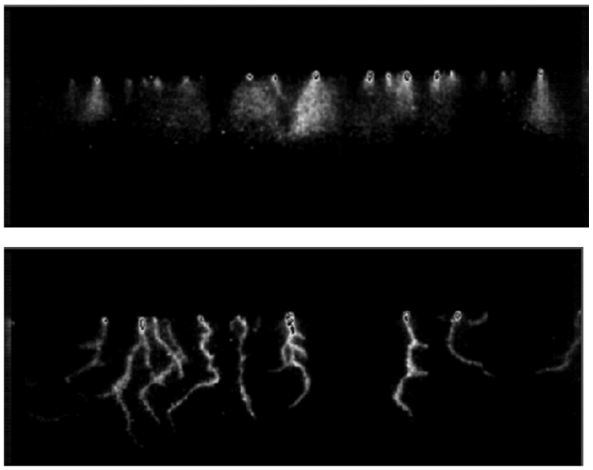

Figure 2.2: High-speed photographs of the DBD discharge[28]

Orlov et al.[34] employs the KINEMA Plasmator software to simulate the plasma behavior in both discharge strokes. The code uses a fluid approximation for the treatment of ions and electrons, solving the continuity and energy equations for the electrons and the continuity and momentum equations for the ions. The neutrals are treated as a background gas and do not enter the simulations except as a source of chemical species and collisional momentum loss. Figure 2.3 shows the 2D rectangular domain for plasma simulation. Although the plasma discharge is inherently a 3D phenomena, this 2D approximation allows the study of some of the discharge characteristics with low computational cost. The domain dimensions are 10 by $7.5mm$ with the plasma actuator located in the lower part of the domain. The exposed electrode is flush-mounted with the dielectric surface while the encapsulated electrode is buried within the dielectric material. The upper part of the domain is represented by pure nitrogen. The simulated results show good agreement with experimental results. They are also able to show the behaviors of ions and electrons that are hard to measure experimentally.

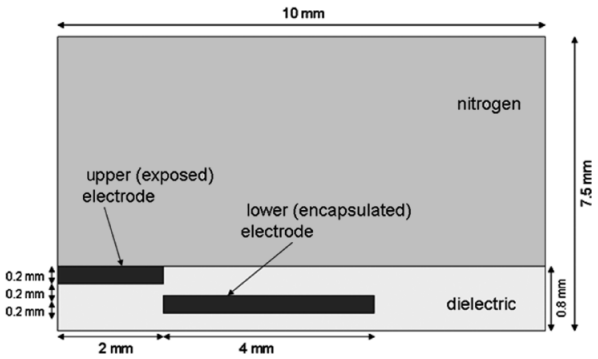

Figure 2.3: Computational domain[34]

Figure 2.4 shows the net-charge density $0.1mm$ above the dielectric surface during the forward and backward discharge in the simulation shown above. During the forward discharge, electrons are emitted from the exposed electrode, colliding with neutral air particles and creating ions in its way before finally resting on the dielectric surface. After a really short period of time, the electrons accumulated on the surface of the dielectric layer are able to shield the effect of the buried electrode. As a result, the electric field strength above the buried electrode is almost zero. Since the electrons are accumulated on the dielectric surface, only positive ions exist in air, resulting in a positive net-charge density in the domain. Due to the shielding effect of the electrons accumulated on the surface of dielectric layer, the electric force is almost non-existent and the position of maximum net-charge density is always located at the right side of the exposed electrode, as shown in Figure 2.4(a). During the backward discharge, the electrons accumulated on the dielectric surface return to the exposed electrode, creating secondary ionization during the process. In this half-cycle, there is nothing to shield the effect of the buried electrode and the electric force is able to push the ions to the right, as can be seen in Figure 2.4(b).

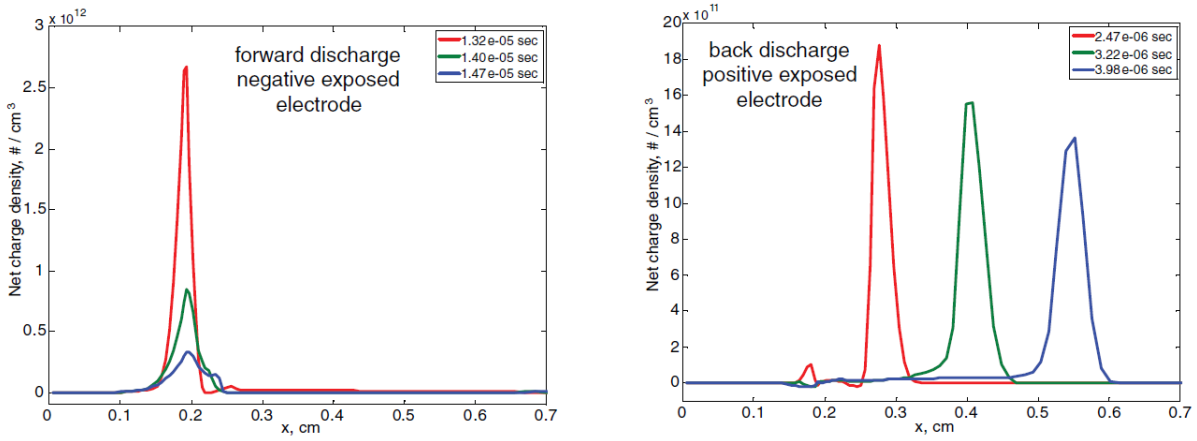

(a) Forward discharge **(b)** Back discharge

Figure 2.4: Plasma net-charge density through one cycle[34]

Many models have been developed to simulate the effect of plasma control by directly solving complex chemical equations. These models typically simulate the interactions among ions, electrons, and neutrals in various gases present in air. An illustrative example is Font and Morgan's model[35], which specifically simulates the ionization process of oxygen and nitrogen in air. These models are constructed on a first-principle basis to describe the creation and movement of ionized species, rendering them valuable tools for comprehending the fundamental physics underlying the DBD plasma actuator. However, it is important to note that such models often require extensive computational time and may involve significant uncertainties in the rates of ionization and recombination. The primary focus of this research is to investigate the flow field behaviors under plasma control. To achieve this objective, it is adequate to employ mathematical models that provide an accurate representation of the body force field without simulating the ionization process. Several examples of simpler models include the Roth model[11], Shyy model[26], Suzen and Huang model[36], and the lumped-element-circuit model[37].

2.2 Roth Model

In 2000, Roth et al.[11] created a computational model to simulate the one-dimensional plasma body force distribution. The equation below could relate the local gradient of the electric field strength and the local net-charge density.

$$\frac{dE}{dx} = \frac{\rho_c}{\varepsilon_0} \tag{2.1}$$

The electric body force was equal to the product of the net-charge density and the electric field strength, as shown in the following equation.

$$F_b = \rho_c E \tag{2.2}$$

Combining the two equations above, they obtained the governing equation for this model,

$$F_b = \frac{d}{dx}(\frac{1}{2}\varepsilon_0 E^2) \tag{2.3}$$

where $\frac{1}{2}\varepsilon_0 E^2$ was the energy density of the electric field. However, it is important to note that the plasma body force simulated by this model is limited to one dimension, whereas real-life plasma body forces typically exhibit at least two dimensions. Therefore, to achieve higher-fidelity results, a more sophisticated model is necessary.

2.3 Shyy's Model

In Shyy et al.[26]'s model, it was assumed that the body force was the strongest at the right edge of the electrode and decayed linearly in both the x and y directions. Since ionization could only occur when the electric field strength exceeded a critical value, plasma was limited

to a region in the vicinity of the actuator. Outside the region, there was no plasma and the body force was always zero. Based on this assumption, the electric field strength in both the x and y directions can be calculated in the following equation,

$$E(x, y) = E_0 - k_1 x - k_2 y \tag{2.4}$$

where E_0 was the maximum electric field strength located on the right side of the exposed electrode, k_1 and k_2 were constants that could determine the rate of decay of the electric field strength in the x and y directions. The plasma existed in a triangular domain shown in Figure 2.5(a). The constants k_1 and k_2 were obtained by calibrating with available experimental data. The maximum electric field strength E_0 could be approximated by the following equation,

$$E_0 = \frac{V}{d}$$

where V was the voltage between the two electrodes and d was the horizontal distance between the two electrodes.

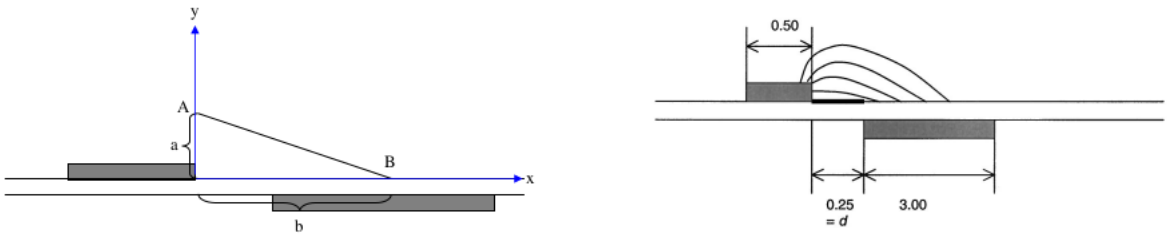

(a) Plasma region **(b)** Electric field lines

Figure 2.5: A sketch of the Shyy's model[26]

Since the direction of the electric field was assumed to be parallel to line AB, the electric field strength in the x and y directions could be calculated by the following equations.

$$E_x(x, y) = \frac{k_2}{\sqrt{k_1^2 + k_2^2}} E(x, y) \tag{2.5}$$

$$E_y(x,y) = \frac{k_1}{\sqrt{k_1^2 + k_2^2}} E(x,y) \tag{2.6}$$

After acquiring the electric field distribution, the body force components in the x and y directions could be calculated by the following equations,

$$f_x(x,y) = E_x(x,y)\rho_c e_c \delta / 2.0 \tag{2.7}$$

$$f_y(x,y) = E_y(x,y)\rho_c e_c \delta / 2.0 \tag{2.8}$$

where $\rho_c = (n_i - n_e)e$ was the net-charge density calculated by the positive charge density minus the negative charge density. In this model, the net-charge density was determined through calibration with experimental results and was assumed to be uniform throughout the entire domain. The Delta function was used to establish the on-and-off state of the plasma body force. In regions where the electric field strength fell below the critical value, δ was set to 0.0, resulting in plasma body force in that region. Conversely, when the electric field strength exceeded the critical value, δ was set to 1.0, and the body force became directly proportional to the electric field strength. Despite its simplicity and usefulness, Shyy's model still had certain drawbacks. For instance, Shyy et al. assumed that the electric field strength decreased linearly from the edge of the electrode, whereas experiments indicated that the electric field strength decreased exponentially and was confined to a much smaller region. As a result, the Shyy's model often overestimated the strength of the body force. Furthermore, Shyy et al. also assumed that the net-charge density remained constant, which was an assumption that did not align with experimental findings.

2.4 Suzen and Huang's Model

Suzen and Huang[36]'s model calculated the plasma body force field using the Poisson equation. This model assumed that the distribution of charged particles in the domain was only

dependent on the potential caused by the electric charge on the wall and was largely unaffected by the external electric field. Under this assumption, the electric potential Φ was decomposed into two parts ϕ and ϕ' using the superposition principle, as shown in the following equation. In this equation, ϕ was the potential field induced by the external power source while ϕ' was the potential field induced by the charge accumulated on the wall.

$$\Phi = \phi + \phi'$$

Under the above assumption, Equation (2.9) solved the potential distribution induced by the external power source ϕ while Equation (2.10) solved the potential distribution induced by the charge accumulated on the wall ϕ'.

$$\nabla \cdot (\varepsilon \nabla \phi) = 0 \tag{2.9}$$

$$\nabla \cdot (\varepsilon \nabla \phi') = -\rho_c \tag{2.10}$$

In the two equations above, ρ_c was the net-charge density and ε was the permittivity of the medium, which was equal to the product between the permittivity of the free space ε_0 and the relative permittivity of the medium ε_r. The net-charge density ρ_c could be related to the potential distribution ϕ' with the following equation, where λ_d was the Deybe length.[35].

$$\rho_c = -\varepsilon_0 \frac{\phi'}{\lambda_d^2} \tag{2.11}$$

By plugging Equation (2.11) into Equation (2.10), the governing equation for the net-charge density was obtained, as shown below.

$$\nabla \cdot (\varepsilon_r \nabla \rho_c) = \rho_c / \lambda_d^2 \tag{2.12}$$

Equations (2.9) and (2.12) served as the governing equations for the distribution of potential and net-charge density. Equation (2.9) were solved in both the air and the dielectric layer. The potential on the exposed electrode was set to the external applied voltage, while the potential on the buried electrode was always set to zero. The potential gradient on the outer boundary was assumed to be zero, provided that the outer boundary was sufficiently far from the plasma actuator. On the other hand, Equation (2.12) was only solved in air because the net-charge density always remained zero inside the dielectric layer. The net-charge density on the outer boundary was set to zero as well. The normal gradient of the net-charge density was presumed to be zero on the dielectric surface, except for the region above the buried electrode. In this specific region, the net-charge density was defined in a manner that synchronized with the external voltage and expressed in the following equation,

$$\rho_{c,w}(x,t) = \rho_c^{max} G(x) f(t) \tag{2.13}$$

where ρ_c^{max} was the maximum net-charge density in the domain and was acquired by calibrating with experimental results. $f(t) = sin(2\pi ft)$ is a sine wave function whose frequency was the same as the carrier frequency of the external AC power source. $G(x)$ was a function chosen to resemble the plasma distribution over the embedded electrode. Both the governing equations and the boundary conditions were sketched in Figure 2.6.

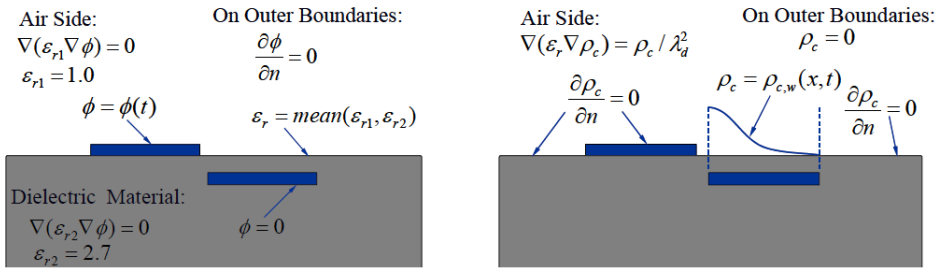

Figure 2.6: Governing equations and boundary conditions for Suzen and Huang's model [36]

After obtaining the potential and net-charge density distribution, the body force field was calculated by the following equation.

$$\overrightarrow{f_b} = \rho_c \overrightarrow{E} = -\rho_c \nabla \phi \tag{2.14}$$

This model had several advantages. The simulated electric and net-charge density fields were concentrated in the vicinity of the plasma actuator and decayed exponentially from the edge of the electrodes, which showed good agreement with the experimental measurements. Despite its advantages, this model still had room for improvement. For example, Suzen and Huang assumed that the ionization process started at the beginning of each cycle while experimental results indicated that ionization could only occur when the voltage exceeded a critical value. The net-charge density distribution on the dielectric surface above the buried electrode was acquired mostly through postulation, rather than being based on physical laws. Therefore, a plasma body force model with even higher fidelity will be introduced.

2.5 Lumped-Element Circuit Model

The lumped-element circuit model was proposed by Mertz and Corke [37]. This model considered both the resistive and capacitive behaviors of air, along with the capacitive properties of the dielectric material. The governing equation was derived from Gauss's law, as presented below.

$$\nabla \cdot (\varepsilon \nabla \phi) = \frac{\phi}{\lambda_d^2} \tag{2.15}$$

The calculation of the potential distribution on the dielectric surface above the buried electrode was performed using a set of equations. When the applied voltage was below the critical value, air was treated as an insulator, and only its capacitive properties were taken into account. However, when the voltage exceeded the critical value, both the capacitive

and resistive properties of air were considered. The dielectric layer was always treated as an insulator, so only its capacitive properties are considered. Figure 2.7 provided an illustration of the lumped-element circuit model. In this model, the computational domain was divided into N parallel sub-circuits and each circuit was comprised of an air capacitor, a dielectric capacitor, and two air resistors. One air resistor R_f was only turned on during the forward discharge and the other resistor R_b was only turned on during backward discharge.

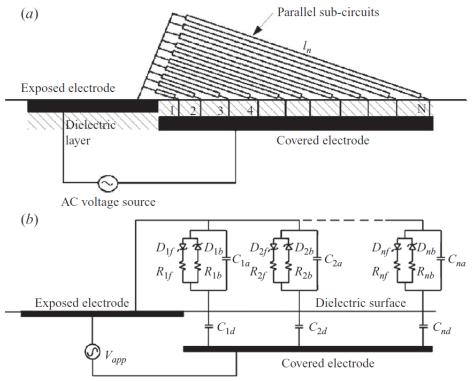

Figure 2.7: Sketch of the lumped element circuit model[37]

Electrons were emitted from the exposed electrode during the forward discharge and from the dielectric surface during the back discharge. Since it was considerably easier for electrons to leave the exposed electrode than to depart from the surface of the dielectric layer, two distinct resistors were employed to accurately simulate both discharge processes. The time-varying voltage at various nodes on the dielectric layer directly above the buried electrode could be calculated using the following equation,

$$\frac{dV_n(t)}{dt} = \left(\frac{C_{n_a}}{C_{n_a} + C_{n_d}}\right)\frac{dV_{app}(t)}{dt} + k_n \frac{I_{n_p}}{C_{n_a} + C_{n_d}} \tag{2.16}$$

where V_{app} is the voltage applied on the exposed electrode, I_{np} is the value of the current passing through air after the critical voltage is reached and $V_n(t)$ is the value of voltage at the nth node on the dielectric surface. C_{na} and C_{nd} were the capacitance values of air and

dielectric layer for element n calculated by the two equations below,

$$C_{na} = \frac{\varepsilon_0 \varepsilon_a A_n}{l_n}$$

$$C_{nd} = \frac{\varepsilon_0 \varepsilon_d A_d}{l_d}$$

where ε_0 was the permittivity of vacuum, ε_a was the relative permittivity of air, and ε_d was the relative permittivity of the dielectric layer. Figure 2.8 showed a sketch of one sub-circuit, where A_n and A_d were the cross-sectional areas of element n in air and dielectric. l_n was the length of the element in air while l_d was the length of the element inside the dielectric layer. k_n was set to one when the applied voltage exceeded the critical voltage and was set to zero otherwise.

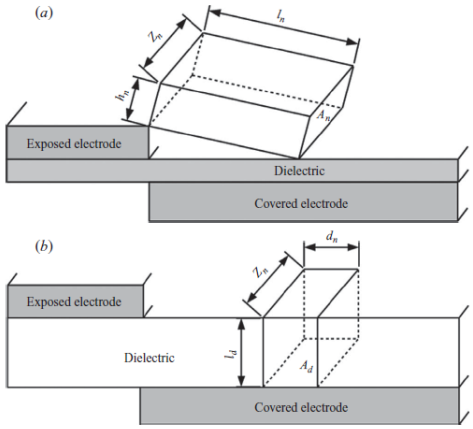

Figure 2.8: Sketch of one single element [37]

For each element n, the electric current passing through this element was calculated by the following equation,

$$I_{np} = \frac{1}{R_n}[V_{app}(t) - V_n(t)] \tag{2.17}$$

where $R_n = \frac{\rho_a l_n}{A_n}$ was the resistance value of element n and ρ_a is the specific resistance value of air. After calculating the potential distribution, the net-charge density distribution was

calculated using the definition of the Deybe length, as shown in the following equation.

$$\rho_c = -\varepsilon_0 \frac{\phi}{\lambda_d^2} \tag{2.18}$$

After successfully simulating the distribution of potential and net-charge density, the distribution of the body force could be calculated as the product of the net-charge density and the electric field strength, as shown in the following equation.

$$\overrightarrow{f_b} = \rho_c \overrightarrow{E} = \varepsilon_0 \frac{\phi}{\lambda_d^2} \nabla\phi \tag{2.19}$$

2.6 D-D Plasma Body Force Model

The D-D plasma body force model was proposed by Nishida1 et al.[38]. In this model, the charged particles including positive ions, negative ions and electrons are considered with basic plasma chemistry including electron impact ionization, attachment and recombination. The time-dependent continuity equations for electrons and ions with a D-D flux are coupled with the Poisson equation. The governing equations are written below,

$$\frac{\partial n_e}{\partial t} + \nabla \cdot (-n_e \mu_e \overrightarrow{E} - D_e \nabla n_e) = (\alpha - \eta) n_e |\nu_e| - r_{ep} n_e n_p \tag{2.20}$$

$$\frac{\partial n_p}{\partial t} + \nabla \cdot (n_p \mu_p \overrightarrow{E} - D_p \nabla n_p) = \alpha n_e |\nu_e| - r_{ep} n_e n_p - r_{pn} n_p n_n \tag{2.21}$$

$$\frac{\partial n_n}{\partial t} + \nabla \cdot (-n_n \mu_n \overrightarrow{E} - D_n \nabla n_n) = \eta n_e |\nu_e| - r_{pn} n_p n_n \tag{2.22}$$

$$\nabla \cdot (\varepsilon_r \overrightarrow{E}) = \frac{e_c}{\varepsilon_0}(n_p - n_e - n_n) + \frac{e_c}{\varepsilon_0}\sigma\delta_s \tag{2.23}$$

where n is the plasma density, μ is the charged particle mobility, and their subscripts e, p, n denotes to electron, positive ion and negative ion. D, α, and η are the coefficients of diffusion, ionization, and attachment, r_{ep} and r_{pn} are the recombination coefficients of

electron-positive-ion and positive-negative-ion, respectively. e_c is the elementary charge and σ is the surface charge density expressed by the Dirac function δ_s. ε_0 and ε_r are the vacuum and relative permittivity of the dielectric layer, respectively. After successfully calculating the time-varying distributions of the charged particles, the plasma body force can be calculated by the equation below.

$$\overrightarrow{f} = e_c(n_p - n_e - n_n)\overrightarrow{E} - [\frac{D_p}{\mu_p}\nabla n_p + \frac{D_e}{\mu_e}\nabla n_e + \frac{D_n}{\mu_n}n_n] \tag{2.24}$$

Comparing to the previous models introduced in this thesis, this model captures the fundamental physics of ionization. It is also able to simulate a time-varying plasma body force field that is especially useful in highly turbulent flows.

Comparing Suzen and Huang's model with the lumped element circuit model and the D-D model, the D-D model has the best representation of the fundamental physics and is able to generate a time-varying plasma body force field with high temporal resolution. This model works especially well in turbulent flows where the flow field changes with time constantly. The only drawback of the D-D model is its complex and time-consuming implementation process. Since our research is mostly focused on laminar flow and turbulent effects are small, we do not need a time-varying plasma body force field. Given that Suzen's model could reasonably match experimental data and was much easier to implement, we decided to use Suzen's model in the current research.

Chapter 3

Numerical Methods for Solving the Plasma Body Force Equations and the Navier-Stokes Equations

3.1 Methods for Solving the Plasma Body Force Equations

In order to save computational time and simplify the algorithm, the plasma generation process and the fluid transportation process are decoupled into two separate parts. In our research, the characteristic velocities of the flow field are on the orders of $1 - 10m/s$. The plasma formation process is characterized by the electron velocity which is in the order of $10^5 m/s$ to $10^6 m/s$ based on the electron temperature ranging from $1000 - 10000K$. The significant difference in characteristic velocities enable the effective decoupling of these two processes. In the general case, the ionization process can be represented by a set of Maxwell's equations shown below, where $\overrightarrow{H}$ is the electric field strength, $\overrightarrow{j}$ is the electric current

density, μ_0 is the electric permeability, $\overrightarrow{E}$ is the electric field strength, ρ_c is the net-charge density and ε is the electric permittivity.

$$\begin{aligned} \nabla \times \overrightarrow{H} &= \overrightarrow{j} + \varepsilon \frac{\partial \overrightarrow{E}}{\partial t} \\ \nabla \times \overrightarrow{E} &= -\mu_0 \frac{\partial \overrightarrow{H}}{\partial t} \\ \nabla \cdot (\varepsilon \overrightarrow{E}) &= \rho_c \\ \nabla \cdot (\mu_0 \overrightarrow{H}) &= 0 \end{aligned} \tag{3.1}$$

Since the time-scale of plasma generation is much smaller than the time-scale of the fluid propagation, the plasma generation process is assumed to be quasi-steady. As a result, the electric current density $\overrightarrow{j}$, the magnetic field strength $\overrightarrow{H}$ are all equal to zero. In addition, the time derivatives $\frac{\partial \overrightarrow{E}}{\partial t}$ and $\frac{\partial \overrightarrow{H}}{\partial t}$ are all equal to zero. Under this assumption, only one of the Maxwell's equations are left, referred to as the Gauss law shown below.

$$\nabla \cdot (\varepsilon \overrightarrow{E}) = \rho_c \tag{3.2}$$

By definition, the electric field strength can be calculated by the potential gradient, while the electric permittivity equals the product of the permittivity of free space and the relative permittivity, as can be seen in the following equations.

$$\overrightarrow{E} = -\nabla \phi \tag{3.3}$$

$$\varepsilon = \varepsilon_0 \varepsilon_r \tag{3.4}$$

Substituting Equation (3.3) into Equation (3.2) gives us the following equation. This is one of the most important equations in the thesis, providing the basis for the governing equations in both the Suzen and Huang's model and the self-developed model. Both models will be

explained in detail in this chapter.

$$\nabla \cdot (\varepsilon_r \nabla \phi) = -\rho_c / \varepsilon_0 \tag{3.5}$$

3.1.1 Suzen and Huang's Model

In our research, we apply Suzen and Huang's model to both the flat plate and square cylinder cases. The governing equations for potential and net-charge density are presented below.

$$\nabla \cdot (\varepsilon_r \nabla \phi) = 0 \tag{3.6}$$

$$\nabla \cdot (\varepsilon_r \nabla \rho_c) = \rho_c / \lambda_d^2 \tag{3.7}$$

Figure 3.1 depicts the domain for the potential ϕ. To obtain the potential distribution, we solve Equation (3.6) in both air and the dielectric layer, where the relative permittivity in air is denoted as $\varepsilon_{r_1} = 1.0$ and the relative permittivity in the dielectric layer is denoted as $\varepsilon_{r_2} = 3.2$. The potential on the outer boundary satisfies the Neumann boundary condition, i.e., $\frac{\partial \phi}{\partial n} = 0$. The boundary condition at the interface between air and the dielectric layer is expressed in the following equation.

$$\varepsilon_{r_1} \frac{\partial \phi}{\partial n}|_1 = \varepsilon_{r_2} \frac{\partial \phi}{\partial n}|_2 \tag{3.8}$$

The potential on the exposed electrode is set to be the input voltage of the external power source, while the potential on the buried electrode is always set to zero.

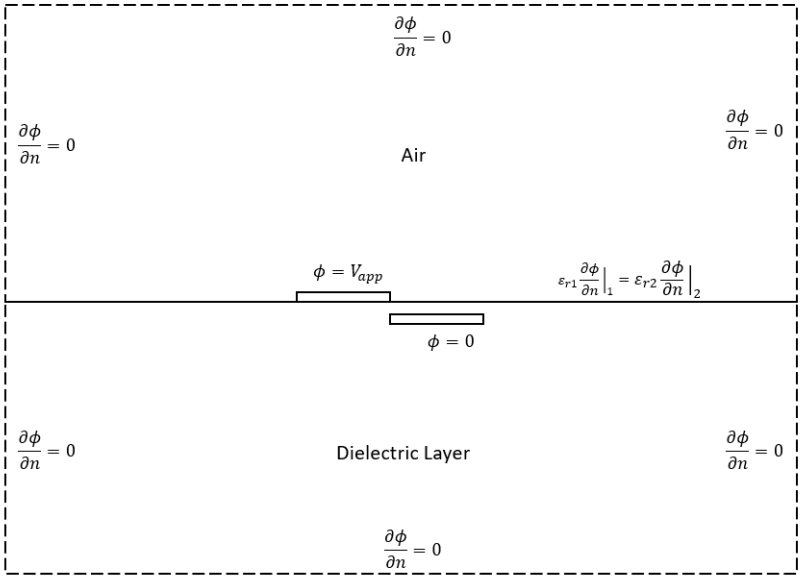

Figure 3.1: The boundary condition for electric potential

Figure 3.2 illustrates the domain for the net-charge density distribution. We only solve Equation (3.7) in air since the net-charge density in the dielectric layer is always zero. At the boundary, the net-charge density is set to zero, denoted as $\rho_c = 0.0$. On the surface of the dielectric layer, the gradient of the net-charge density normal to the surface is also set to zero, denoted as $\frac{\partial \rho_c}{\partial n} = 0.0$, except for the region directly above the buried electrode. In that region, the net-charge density distribution is calculated using the following equation,

$$\rho_{c,w} = \rho_c^{max} G(x) f(t) \tag{3.9}$$

where ρ_c^{max} is the maximum net-charge density, $f(t)$ is the sinusoidal function of the voltage on the exposed electrode. $G(x)$ is the half-Gaussian distribution shown blow, where x_0 is the location of the maximum net-charge density, which is assumed to be the left side of the buried electrode. σ is the scale parameter determining the rate of decay.

$$G(x) = exp[-(x - x_0)^2/(2\sigma^2)] \tag{3.10}$$

In this model, three parameters require calibration: the maximum net-charge density ρ_c^{max}, the scale parameter σ, and the Debye length λ_d. These parameters are calibrated using experimental results conducted by Xue et al.[12], in which a train of vortices is generated by a DBD plasma actuator installed on a flat plate. The calibration process will be explained in detail in the subsequent chapters.

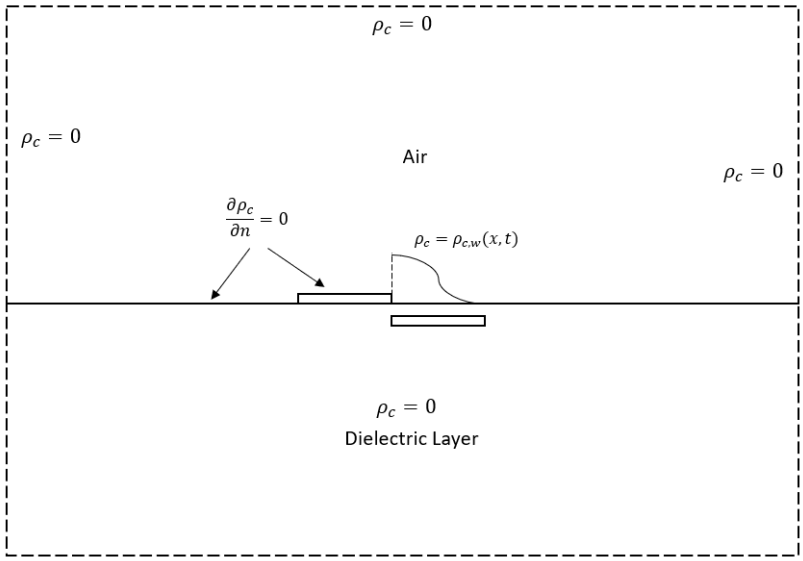

Figure 3.2: The boundary condition for net charged density

The two equations below show the governing equations of the Suzen's model in $2D$,

$$\frac{\partial^2 \phi}{\partial x^2} + \frac{\partial^2 \phi}{\partial y^2} = 0 \tag{3.11}$$

$$\frac{\partial^2 \rho_c}{\partial x^2} + \frac{\partial^2 \rho_c}{\partial y^2} = \frac{\rho_c}{\varepsilon_r \lambda_d^2} \tag{3.12}$$

which need to be discretized before they are solved numerically. The second-order derivatives at the point (i, j) are calculated using the Taylor Series Expansion, as demonstrated in the following equations.

$$\frac{\partial^2 \phi}{\partial x^2}|_{i,j} = \frac{2(\phi_{i+1,j} - \phi_{i,j})}{(x_{i+1,j} - x_{i,j})(x_{i+1,j} - x_{i-1,j})} - \frac{2(\phi_{i,j} - \phi_{i-1,j})}{(x_{i,j} - x_{i-1,j})(x_{i+1,j} - x_{i-1,j})}$$

$$\frac{\partial^2\phi}{\partial y^2}|_{i,j} = \frac{2(\phi_{i,j+1}-\phi_{i,j})}{(y_{i,j+1}-y_{i,j})(y_{i,j+1}-y_{i,j-1})} - \frac{2(\phi_{i,j}-\phi_{i,j-1})}{(y_{i,j}-y_{i,j-1})(y_{i,j+1}-y_{i,j-1})}$$

After discretization, the potential equation becomes the following equation,

$$A(\phi_{i+1,j}-\phi_{i,j}) - B(\phi_{i,j}-\phi_{i-1,j}) + C(\phi_{i,j+1}-\phi_{i,j}) - D(\phi_{i,j}-\phi_{i,j-1}) = 0 \tag{3.13}$$

where the parameters A, B, C, D are expressed below.

$$A = \frac{2}{(x_{i+1,j}-x_{i-1,j})(x_{i+1,j}-x_{i,j})}, B = \frac{2}{(x_{i+1,j}-x_{i-1,j})(x_{i,j}-x_{i-1,j})}$$

$$C = \frac{2}{(y_{i,j+1}-y_{i,j-1})(y_{i,j+1}-y_{i,j})}, D = \frac{2}{(y_{i,j+1}-y_{i,j-1})(y_{i,j}-y_{i,j-1})}$$

The governing equation for net-charge density can be discretized in the same way,

$$A(\rho_{i+1,j}-\rho_{i,j}) - B(\rho_{i,j}-\rho_{i-1,j}) + C(\rho_{i,j+1}-\rho_{i,j}) - D(\rho_{i,j}-\rho_{i,j-1}) - \frac{\rho_{i,j}}{\varepsilon_r\lambda_d^2} = 0 \tag{3.14}$$

where the parameters A, B, C, D are expressed below.

$$A = \frac{2}{(x_{i+1,j}-x_{i-1,j})(x_{i+1,j}-x_{i,j})}, B = \frac{2}{(x_{i+1,j}-x_{i-1,j})(x_{i,j}-x_{i-1,j})}$$

$$C = \frac{2}{(y_{i,j+1}-y_{i,j-1})(y_{i,j+1}-y_{i,j})}, D = \frac{2}{(y_{i,j+1}-y_{i,j-1})(y_{i,j}-y_{i,j-1})}$$

At the interface between air and dielectric, denoted as $j = J$, the following condition is applied.

$$\varepsilon_{r_1}\frac{\phi_{i,J+1}-\phi_{i,J}}{y_{i,J+1}-y_{i,J}} = \varepsilon_{r_2}\frac{\phi_{i,J}-\phi_{i,J-1}}{y_{i,J}-y_{i,J-1}} \tag{3.15}$$

After the potential and net-charge density distribution is successfully simulated, the body force can be calculated with the following equation, where $\overrightarrow{F_b}(x,y,t) = (F_{bx}(x,y,t), F_{by}(x,y,t))$

$$\overrightarrow{F_b}(x,y,t) = \rho_c(x,y,t)\overrightarrow{E}(x,y,t) = -\rho_c(x,y,t)\nabla\phi(x,y,t) \tag{3.16}$$

3.1.2 Self-Developed Model

Although Suzen and Huang's model performed well for the first two cases, it did not show satisfactory agreement with experimental data when the actuators were placed on a curved surface, such as a circular cylinder. To enhance fidelity, we need a model with more parameters available for calibration. Since the Shyy's model features more parameters than the Suzen and Huang model, it offers greater flexibility during the calibration process. However, completely replacing Suzen and Huang's model with the Shyy model may not be advisable, as Suzen and Huang's model excels in calculating the net-charge density distribution. The optimal approach is to use the equations from Shyy's model to calculate the potential distribution and the equations from Suzen and Huang's model to calculate the net-charge density distribution. Figure 3.3 shows the domain of the body force distribution in this new model. At the boundary of the triangle, the electric field strength decreases to the breakdown electric field E_b. Beyond the triangle, the electric field strength is too weak to ionize air so plasma does not exist outside the triangle. Therefore, the plasma body force is only present within the triangle.

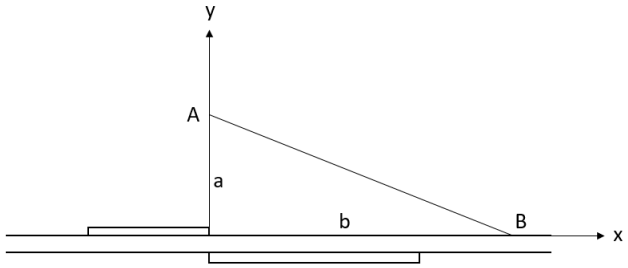

Figure 3.3: Electric field strength

In the newly developed model, the maximum electric field strength is calculated as $E_0 = \frac{\phi^{max}(t)}{d}$, where $\phi^{max}(t)$ represents the electric potential on the exposed electrode, and d is the vertical distance between the exposed and buried electrodes. The electric field strength is assumed to decrease linearly in both the x and y directions and can be calculated using the

following equation,

$$E(x, y, t) = E_0(t) - k_1 x - k_2 y \tag{3.17}$$

where k_1 and k_2 are constants calculated below. In the following equations, a and b are the height and length of the triangle shown in Figure 3.3 while E_b is the breakdown electric field strength. The parameters a, b are determined by calibrating against experimental data.

$$k_1 = \frac{E_0(t) - E_b}{b} \tag{3.18}$$

$$k_2 = \frac{E_0(t) - E_b}{a} \tag{3.19}$$

The net-charge density ρ_c can be calculated by the following equation, where ε_r is the relative permittivity of air and λ_d is the Debye length[39].

$$\nabla \cdot (\varepsilon_r \nabla \rho_c) = \rho_c / \lambda_d^2 \tag{3.20}$$

The governing equation for the net-charge density and its corresponding boundary conditions are illustrated in Figure 3.4. The domain is a sector of 120° with the plasma actuator located in the middle. The upper domain is air while the lower domain is the dielectric material. Since plasma only exists in the vicinity of the plasma actuator, the net-charge density is set to zero at the outer boundary. A zero normal gradient for the net-charge density is imposed on all solid walls except in the region directly above the buried electrode, where the net-charge density along the curved surface can be calculated by Equation (3.21). Inside the dielectric layer, the net-charge density is set to zero everywhere because charged particles do not exist in that region.

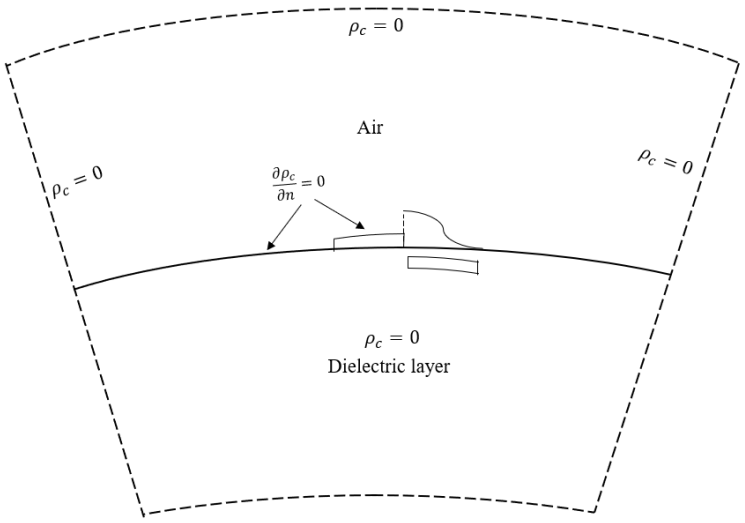

Figure 3.4: Governing equations and boundary conditions

On the surface of the dielectric layer directly above the buried electrode, the net-charge density is assumed to be in sync with the AC voltage applied on the exposed electrode, as shown in the following equation,

$$\rho_{c,w} = \rho_c^{max} G(x) f(t) \tag{3.21}$$

where ρ_c^{max} is the maximum net-charge density and $G(x)$ is the half-Gaussian distribution along the cylinder surface given by the following equation, where x is the distance along the curved surface away from the right side of the exposed electrode, x_0 is the location of the maximum net-charge density, and σ is the scale parameter determining the rate of decay.

$$G(x) = exp[-\frac{(x - x_0)^2}{2\sigma^2}] \tag{3.22}$$

For this model, the parameters a, b, λ_d, ρ_c^{max} and σ are acquired by calibrating against the experimental results. The parameters that show the best agreement with experimental results are $a = 10mm$, $b = 20mm$, $\lambda_d = 4mm$, $\rho_c^{max} = 0.008C/m^3$ and $\sigma = 5mm$. The discretized governing equation for net-charge density in the cylindrical coordinates is shown

below,

$$\frac{\partial^2 \rho_c}{\partial r^2}|_{i,j} + \frac{1}{r_{i,j}}\frac{\partial \rho_c}{\partial r}|_{i,j} + \frac{1}{r_{i,j}^2}\frac{\partial^2 \rho_c}{\partial \theta^2}|_{i,j} = \frac{\rho_{c_{i,j}}}{\varepsilon_r \lambda_d^2} \tag{3.23}$$

where

$$\frac{\partial^2 \rho_c}{\partial r^2}|_{i,j} = \frac{2(\rho_c^{i,j+1} - \rho_c^{i,j})}{(r^{i,j+1} - r^{i,j})(r^{i,j+1} - r^{i,j-1})} - \frac{2(\rho_c^{i,j} - \rho_c^{i,j-1})}{(r^{i,j} - r^{i,j-1})(r^{i,j+1} - r^{i,j-1})}$$

$$\frac{\partial \rho_c}{\partial r}|_{i,j} = \frac{\rho_c^{i,j+1} - \rho_c^{i,j-1}}{r^{i,j+1} - r^{i,j-1}}$$

$$\frac{\partial^2 \rho_c}{\partial \theta^2}|_{i,j} = \frac{2(\rho_c^{i,j+1} - \rho_c^{i,j})}{(\theta^{i,j+1} - \theta^{i,j})(\theta^{i,j+1} - \theta^{i,j-1})} - \frac{2(\rho_c^{i,j} - \rho_c^{i,j-1})}{(\theta^{i,j} - \theta^{i,j-1})(\theta^{i,j+1} - \theta^{i,j-1})}$$

After the potential and net-charge density distribution are successfully simulated, the body force is calculated by the following equation, where $\overrightarrow{F_b}(x, y, t) = (F_{b_x}(x, y, t), F_{b_y}(x, y, t))$.

$$\overrightarrow{F_b}(x, y, t) = \frac{\rho_c(x, y, t)}{\rho_{air}} \overrightarrow{E}(x, y, t) \tag{3.24}$$

Figure 3.5 displays the body force contours generated by both the Suzen and Huang's model and the newly developed model. The body force generated by the newly developed method exhibits a significantly larger region of influence when compared to the body force generated by the Suzen and Huang's model. The less concentrated body force field imparts a gentle, prolonged push along the cylinder surface, as opposed to the short, intense push provided by Suzen and Huang's model. The simulated results obtained using the newly developed model demonstrate much closer agreement with experimental data when compared to the results from Suzen and Huang's model.

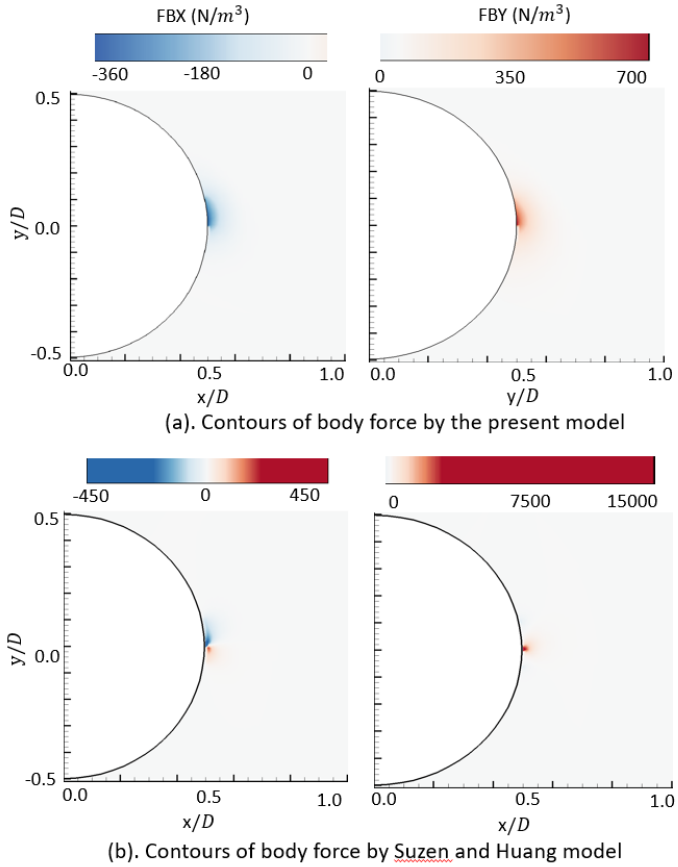

Figure 3.5: Comparison between body force contours generated by different methods

Due to the high frequency of the AC power source, the flow field does not have sufficient time to respond to the rapid changes in the AC signal. For both methods described above, the plasma body force can be treated as a constant calculated by the following two equations, where $f_{bx}(x, y)$ and $f_{by}(x, y)$ denote the body forces in the x and y directions.

$$f_{bx}(x, y) = \frac{1}{T_{AC}} \int_T F_{bx}(x, y, t)dt \tag{3.25}$$

$$f_{by}(x, y) = \frac{1}{T_{AC}} \int_T F_{by}(x, y, t)dt \tag{3.26}$$

3.2 Method for solving the Navier-Stokes Equations

3.2.1 The SIMPLE algorithm implemented on staggered grids

Since this research is focused on low speed 2 dimensional flow, the governing equations are the $2D$ incompressible Navier-Stokes equations shown below, where the body forces f_{bx} and f_{by} in the Navier-Stokes equations are calculated using Equations (3.25) and (3.26).

$$\frac{\partial u}{\partial x} + \frac{\partial v}{\partial y} = 0 \tag{3.27}$$

$$\frac{\partial(\rho u)}{\partial t} + \frac{\partial(\rho u^2)}{\partial x} + \frac{\partial(\rho uv)}{\partial y} = -\frac{\partial p}{\partial x} + \mu(\frac{\partial^2 u}{\partial x^2} + \frac{\partial^2 u}{\partial y^2}) + \rho f_{bx} \tag{3.28}$$

$$\frac{\partial(\rho v)}{\partial t} + \frac{\partial(\rho uv)}{\partial x} + \frac{\partial(\rho v^2)}{\partial y} = -\frac{\partial p}{\partial y} + \mu(\frac{\partial^2 v}{\partial x^2} + \frac{\partial^2 v}{\partial y^2}) + \rho f_{by} \tag{3.29}$$

The continuity and Navier-Stokes equations are solved using the Semi-Implicit Method for Pressure-Linked Equations (SIMPLE) algorithm on staggered grids. In most grid types, the flow field values are stored at each vertex, and gradient values can be calculated based on the values of neighboring points. Under the second order central scheme, the discretized form of the continuity equation on a standard mesh is expressed in the following equation.

$$\frac{u_{i+1,j} - u_{i-1,j}}{2\Delta x} + \frac{v_{i,j+1} - v_{i,j-1}}{2\Delta y} = 0 \tag{3.30}$$

The solutions of Equation (3.30) have the possibility to produce a checkerboard velocity distribution, as illustrated in Figure 3.6. While the velocity distribution in this figure does not conform to the actual continuity equation, it does satisfy the discretized continuity equation. In other words, the simulated velocity field may not represent a physically realistic flow. To avoid this phenomenon, a staggered grid is employed.

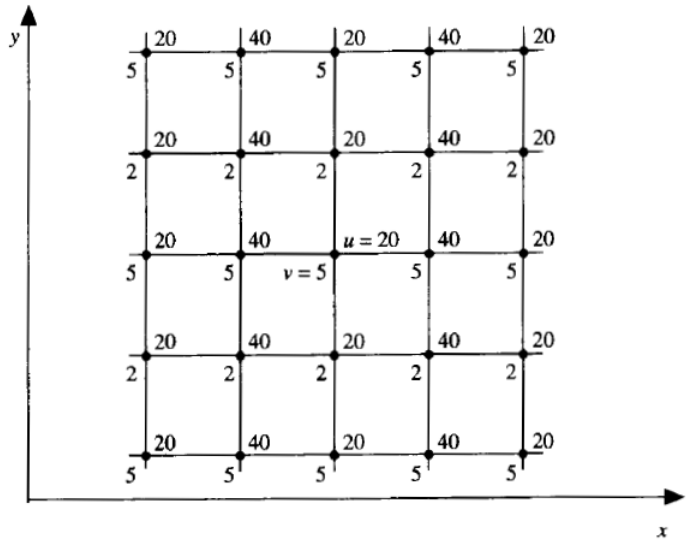

Figure 3.6: The checkerboard velocity distribution [40]

Figure 3.7 shows an example of the staggered grid. In this grid system, scalar terms such as pressure and density are stored at the vertices, while vector terms such as velocity and momentum are stored at the midpoints between two vertices.

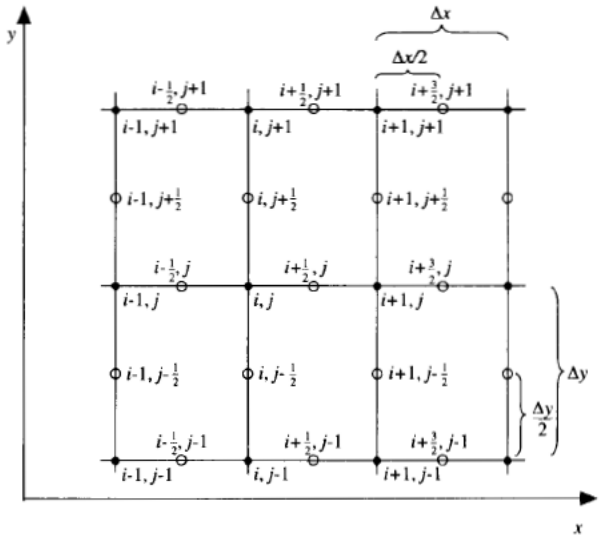

Figure 3.7: Simple sketch of the staggered grid [40]

Taking point (i,j) as an example, the pressure value is stored at point (i,j), while the momentum and velocity values in the x-direction are stored at points (i+$\frac{1}{2}$,j) and (i-$\frac{1}{2}$,j). Similarly,

the momentum and velocity in the y-direction are stored at points (i,j+$\frac{1}{2}$) and (i,j-$\frac{1}{2}$). The discretized continuity equation on the staggered grid is expressed as follows.

$$\frac{(\rho u)_{i+1/2,j} - (\rho u)_{i-1/2,j}}{x_{i+1/2,j} - x_{i-1/2,j}} + \frac{(\rho v)_{i,j+1/2} - (\rho v)_{i,j-1/2}}{y_{i,j+1/2} - y_{i,j-1/2}} = 0 \tag{3.31}$$

After successfully simulating the velocity values on the staggered grid, the velocities on the vertices can be calculated by simple averaging, as shown in the equations below.

$$u_{i,j} = \frac{(u_{i-1/2,j} + u_{i+1/2,j})}{2}$$

$$v_{i,j} = \frac{(v_{i,j-1/2} + v_{i,j+1/2})}{2}$$

In this research, an improved version of the SIMPLE algorithm is implemented using the finite-volume method. Figure 3.8 shows several adjacent grid cells within the staggered grid, where pressure and density values are stored at the vertices and velocity values are stored at the midpoint between two vertices.

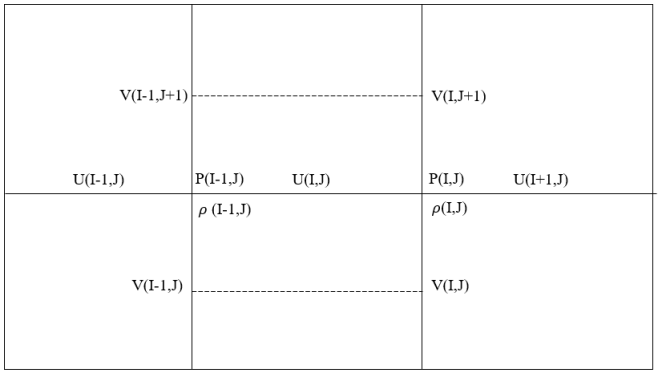

Figure 3.8: Sketch of one single staggered grid

In the finite-volume method, the integration of the Navier-Stokes equation in the x-direction is performed within a control volume shown in Figure 3.9, where the velocity u is located at the center of the control volume. The momentum values $(\rho u)_e$, $(\rho u)_w$, $(\rho v)_n$, and $(\rho v)_s$ are

located to the east, west, north, and south of the control volume.

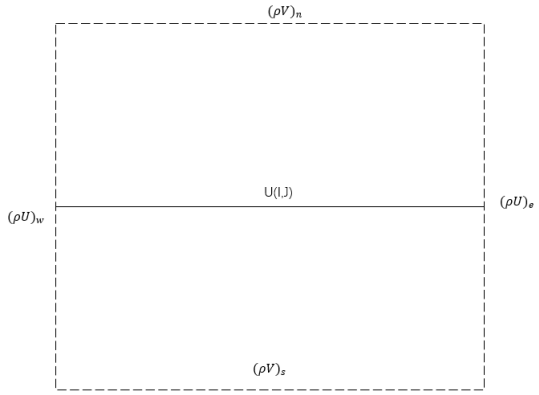

Figure 3.9: The control volume for velocity in the x-direction

The equation below shows the integrated momentum equation in the x-direction, where Δx and Δy are the length of the rectangular sides in the x and y directions.

$$\begin{aligned}\int_{\Delta x}\int_{\Delta y}\frac{\partial \rho u}{\partial t}dxdy + \int_{\Delta x}\int_{\Delta y}\frac{\partial(\rho u^2)}{\partial x}dxdy + \int_{\Delta x}\int_{\Delta y}\frac{\partial(\rho uv)}{\partial y}dxdy = \\ -\int_{\Delta x}\int_{\Delta y}\frac{\partial p}{\partial x}dxdy + \int_{\Delta x}\int_{\Delta y}\mu(\frac{\partial^2 u}{\partial x^2}+\frac{\partial^2 u}{\partial y^2})dxdy + \int_{\Delta x}\int_{\Delta y}\rho g_x dxdy\end{aligned} \tag{3.32}$$

For time-marching purposes, the residual RSU is defined as follow.

$$\begin{aligned}RSU = &-\int_{\Delta x}\int_{\Delta y}\frac{\partial(\rho u^2)}{\partial x}dxdy - \int_{\Delta x}\int_{\Delta y}\frac{\partial(\rho uv)}{\partial y}dxdy - \int_{\Delta x}\int_{\Delta y}\frac{\partial p}{\partial x}dxdy \\ &+\int_{\Delta x}\int_{\Delta y}\mu(\frac{\partial^2 u}{\partial x^2}+\frac{\partial^2 u}{\partial y^2})dxdy + \int_{\Delta x}\int_{\Delta y}\rho g_x dxdy\end{aligned}$$

In order to use the residuals from the current time step and the next time step, Equation (3.32) is transformed into the following equation,

$$\int_{\Delta x}\int_{\Delta y}\frac{\partial \rho u}{\partial t}dxdy = \alpha RSU^{n+1} + (1-\alpha)RSU^n \tag{3.33}$$

where RSU^n and RSU^{n+1} are the residuals in the current and next time steps and the parameter α is used to control the time-marching method. When $\alpha = 0.0$, this method

becomes the Euler implicit method. When $\alpha = 1.0$, this method becomes the Euler explicit method. When $\alpha = 0.5$, this method becomes the Crank–Nicolson scheme where both the information from the current and future residuals are used. In this research, we set $\alpha = 0.5$ and the discretized residuals in the current and next time steps are shown below.

$$\begin{aligned} RSU^n = &- [(\rho u^2)_e^n - (\rho u^2)_w^n]\Delta y - [(\rho uv)_n^n - (\rho uv)_s^n]\Delta x \\ &+ \mu[\frac{\partial u}{\partial x}|_e^n \Delta y - \frac{\partial u}{\partial x}|_w^n \Delta y + \frac{\partial u}{\partial y}|_n^n \Delta x - \frac{\partial u}{\partial y}|_s^n \Delta x] - (p_{i,j}^n - p_{i-1,j}^n)\Delta y + \rho g_x \Delta x \Delta y \end{aligned} \tag{3.34}$$

$$\begin{aligned} RSU^{n+1} = &- [(\rho u^2)_e^{n+1} - (\rho u^2)_w^{n+1}]\Delta y - [(\rho uv)_n^{n+1} - (\rho uv)_s^{n+1}]\Delta x \\ &+ \mu[\frac{\partial u}{\partial x}|_e^{n+1} \Delta y - \frac{\partial u}{\partial x}|_w^{n+1} \Delta y + \frac{\partial u}{\partial y}|_n^{n+1} \Delta x - \frac{\partial u}{\partial y}|_s^{n+1} \Delta x] - (p_{i,j}^{n+1} - p_{i-1,j}^{n+1})\Delta y + \rho g_x \Delta x \Delta y \end{aligned} \tag{3.35}$$

To simplify Equations (3.34) and (3.35), we define the fluxes in the east, west, north and south sides of the grid cell by the following equations.

$F_e = \rho u_e \Delta y$, $F_w = \rho u_w \Delta y$,

$F_n = \rho v_n \Delta x$, $F_s = \rho v_s \Delta x$

Using the equations above, the convection terms $(\rho u^2)_e$, $(\rho u^2)_w$, $(\rho uv)_n$, $(\rho uv)_s$ can be simplified into the following equations,

$(\rho u^2)_e \Delta y = F_e u_e$, $(\rho u^2)_w \Delta y = F_w u_w$,

$(\rho uv)_n \Delta x = F_n u_n$ and $(\rho uv)_s \Delta x = F_s u_s$

while the diffusion terms $\frac{\partial u}{\partial x}|_e$, $\frac{\partial u}{\partial x}|_w$, $\frac{\partial u}{\partial y}|_n$, $\frac{\partial u}{\partial y}|_s$ can be calculated by Taylor series expansion shown below.

$\frac{\partial u}{\partial x}|_e = \frac{u_{i+1,j} - u_{i,j}}{\Delta x}$, $\frac{\partial u}{\partial x}|_w = \frac{u_{i,j} - u_{i-1,j}}{\Delta x}$,

$\frac{\partial u}{\partial y}|_n = \frac{u_{i,j+1} - u_{i,j}}{\Delta y}$, $\frac{\partial u}{\partial y}|_s = \frac{u_{i,j} - u_{i,j-1}}{\Delta y}$,

According to the flux splitting scheme, the convection terms can be calculated by the following equations.

$$F_e u_e = max(F_e, 0)u_{i,j} - max(-F_e, 0)u_{i+1,j}$$

$$F_w u_w = max(F_w, 0)u_{i-1,j} - max(-F_w, 0)u_{i,j}$$

$$F_n u_n = max(F_n, 0)u_{i,j} - max(-F_n, 0)u_{i,j+1}$$

$$F_s u_s = max(F_s, 0)u_{i,j-1} - max(-F_s, 0)u_{i,j}$$

After plugging the convection and diffusion terms into equations (3.34) and (3.35), the residuals for the current time step and the next time step are transformed into the following equations,

$$RSU^n = a_e u^n_{i+1,j} + a_w u^n_{i-1,j} + a_n u^n_{i,j+1} + a_s u^n_{i,j-1} - a_p u^n_{i,j} + (p^n_{i-1,j} - p^n_{i,j})\Delta y + S \quad (3.36)$$

$$RSU^{n+1} = a_e u^{n+1}_{i+1,j} + a_w u^{n+1}_{i-1,j} + a_n u^{n+1}_{i,j+1} + a_s u^{n+1}_{i,j-1} - a_p u^{n+1}_{i,j} + (p^{n+1}_{i-1,j} - p^{n+1}_{i,j})\Delta y + S \quad (3.37)$$

where the parameters a_e, a_w, a_n, a_s, a_p, and S are calculated by the equations below.

$$a_e = \mu\frac{\Delta y}{\Delta x} + max(-F_e, 0)$$

$$a_w = \mu\frac{\Delta y}{\Delta x} + max(F_w, 0)$$

$$a_n = \mu\frac{\Delta x}{\Delta y} + max(-F_n, 0)$$

$$a_s = \mu\frac{\Delta x}{\Delta y} + max(F_s, 0)$$

$$a_p = a_e + a_w + a_n + a_s$$

$$S = \rho g_x \Delta x \Delta y$$

The newly updated version of the governing equation is expressed as follow, where the residual of the current time step is treated as a known variable while the residual of the next time step is implemented into the following equation.

$$(\frac{RDT}{\alpha} + a_p)u^{n+1}_{i,j} = a_e u^{n+1}_{i+1,j} + a_w u^{n+1}_{i-1,j} + a_n u^{n+1}_{i,j+1} + a_s u^{n+1}_{i,j-1} + (p^{n+1}_{i-1,j} - p^{n+1}_{i,j})\Delta y + SU \quad (3.38)$$

In this equation, the parameters RDT and SU are defined by the following expressions.

$$RDT = \frac{\rho \Delta x \Delta y}{\Delta t}$$

$$SU = S + \frac{(1-\alpha)RSU^n + RDTu^n_{i,j}}{\alpha}$$

For simplification purposes, we define a new term $\sum_k a_k u_k^{n+1}$ and update the parameter a_p according to the following equations.

$$\sum_k a_k u_k^{n+1} = a_e u_{i+1,j}^{n+1} + a_w u_{i-1,j}^{n+1} + a_n u_{i,j+1}^{n+1} + a_s u_{i,j-1}^{n+1}$$

$$a_p = \frac{RDT}{\alpha} + a_p$$

After plugging the above two terms into Equation (3.38), we get the following governing equation.

$$a_p u_{i,j}^{n+1} = \sum_k a_k u_k^{n+1} + SU + (p_{i-1,j}^{n+1} - p_{i,j}^{n+1})\Delta y \tag{3.39}$$

The governing equation for the velocity in the y-direction, denoted as $v_{i,j}^{n+1}$, can be deduced in a similar manner, as shown in the following equation.

$$a_p v_{i,j}^{n+1} = \sum_k a_k v_k^{n+1} + SU + (p_{i,j-1}^{n+1} - p_{i,j}^{n+1})\Delta x \tag{3.40}$$

The first step of the SIMPLE algorithm is to guess a pressure field, p^*. Then the initial velocities u^* and v^* can be calculated from the guessed pressure field, using the following equations

$$a_p u_{i,j}^{*^{n+1}} = \sum_k a_k u_k^{*^{n+1}} + SU + (p^{*n+1}{}_{i-1,j} - p^{*n+1}{}_{i,j})\Delta y \tag{3.41}$$

$$a_p v_{i,j}^{*^{n+1}} = \sum_k a_k v_k^{*^{n+1}} + SU + (p^{*n+1}{}_{i,j-1} - p_{i,j}^{*^{n+1}})\Delta x \tag{3.42}$$

In our code, Equations (3.41) and (3.42) are calculated using the ADI method combined

with the TDMA flow solver. The exact values are calculated by adding the guessed values and the correction values together, as shown in the following equations.

$$p = p^* + p' \tag{3.43}$$

$$u = u^* + u' \tag{3.44}$$

$$v = v^* + v' \tag{3.45}$$

Using Equation (3.39) to subtract Equation (3.41), and equation (3.40) to subtract equation (3.42), we get the governing equations for the correction velocities and the correction pressures.

$$a_p u'(i,j) = \sum_k a_k u'_k + (p'_{i-1,j} - p'_{i,j})\Delta y \tag{3.46}$$

$$a_p v'(i,j) = \sum_k a_k v'_k + (p'_{i,j-1} - p'_{i,j})\Delta x \tag{3.47}$$

Since the SIMPLE algorithm assumes that the velocity corrections $\sum_k a_k u'_k$ and $\sum_k a_k v'_k$ equal to zero when the flow field reaches steady-state, the governing equations for the correction terms are simplified into the following equations.

$$a_p u'_{i,j} = (p'_{i-1,j} - p'_{i,j})\Delta y \tag{3.48}$$

$$a_p v'_{i,j} = (p'_{i,j-1} - p'_{i,j})\Delta x \tag{3.49}$$

The governing equation for pressure is derived in the pressure control volume shown in Figure 3.10, where pressure is located in the middle and the 4 velocities $u_{i,j}$, $u_{i+1,j}$, $v_{i,j}$, $v_{i,j+1}$ are located on the 4 sides of the control volume.

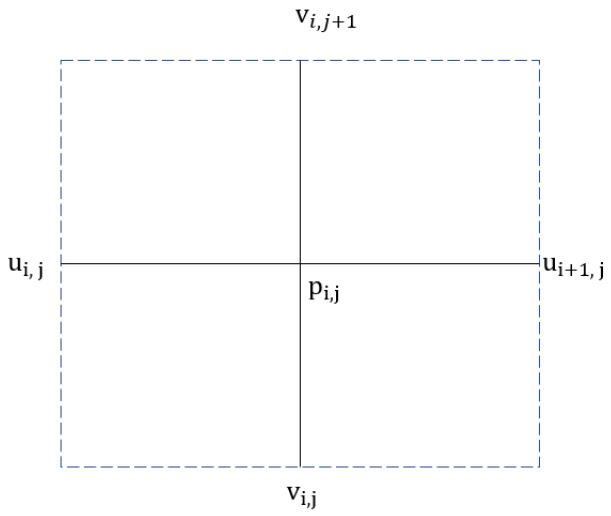

Figure 3.10: The control volume for pressure

Equations (3.48) and (3.49) can be used for the velocity values in the adjacent vertices, denoted as $u_{i,j}$, $u_{i+1,j}$, $v_{i,j}$, $v_{i,j+1}$. For simplicity, we rename the velocities according to their locations in the control volume, where $u_w = u_{i,j}$, $u_e = u_{i+1,j}$, $v_s = v_{i,j}$, and $v_n = v_{i,j+1}$. Using these new variables, the velocity correction terms in the east, west, north and south sides of the control volume are calculated in the following equations.

$$a_e u'_e = (p'_{i,j} - p'_{i+1,j})\Delta y$$

$$a_w u'_w = (p'_{i-1,j} - p'_{i,j})\Delta y$$

$$a_n v'_n = (p'_{i,j} - p'_{i,j+1})\Delta x$$

$$a_s v'_s = (p'_{i,j-1} - p'_{i,j})\Delta x$$

In the equations above, a_e, a_w, a_n, a_s are different from the parameters defined in the governing equations for velocity. They are basically coefficient a_p applied for u_e, u_w, v_s, and v_n. To make things simpler, we define $d_e = \Delta y/a_e$, $d_w = \Delta y/a_w$, $d_n = \Delta x/a_n$, $d_s = \Delta x/a_s$

and the above four equations can be rewritten as the following equations.

$$u'_w = d_w(p'_{i-1,j} - p'_{i,j}) \tag{3.50}$$

$$u'_e = d_e(p'_{i,j} - p'_{i+1,j}) \tag{3.51}$$

$$v'_n = d_n(p'_{i,j} - p'_{i,j+1}) \tag{3.52}$$

$$v'_s = d_s(p'_{i,j-1} - p'_{i,j}) \tag{3.53}$$

The integrated continuity equation over the control volume is shown below.

$$[(\rho u)_e^{n+1} - (\rho u)_w^{n+1}]\Delta y + [(\rho v)_n^{n+1} - (\rho v)_s^{n+1}]\Delta x = 0 \tag{3.54}$$

After substituting Equations (3.50) to (3.53) into Equation (3.54), we can derive the governing equation for pressure, as shown below.

$$a_p p'_{i,j} = a_e p'_{i+1,j} + a_w p'_{i-1,j} + a_n p'_{i,j+1} + a_s p'_{i,j-1} + b \tag{3.55}$$

In the pressure equation, the parameters a_e, a_w, a_n, a_s, a_p and b are calculated in the following equations.

$$a_e = \rho d_e \Delta y$$

$$a_w = \rho d_w \Delta y$$

$$a_n = \rho d_n \Delta x$$

$$a_s = \rho d_s \Delta x$$

$$a_p = a_w + a_e + a_n + a_s$$

$$b = [(\rho u)_w^{*^{n+1}} - (\rho u)_e^{*^{n+1}}]\Delta y + [(\rho v)_s^{*^{n+1}} - (\rho v)_n^{*^{n+1}}]\Delta x$$

The steps of the SIMPLE algorithm are summarized as follow:

1. Guess the pressure field distribution.
2. Calculate the guessed values of u^* and v^* using Equations (3.41) and (3.42).
3. Solve Equation (3.55) to get pressure correction p'.
4. Use Equations (3.48) and (3.49) to get velocity corrections u' and v'.
5. Use Equations (3.43), (3.44), and (3.45) to get pressure and velocity field after correction.
6. Use the newly calculated pressure field p^{n+1} as the guessed value for the next iteration.
7. Keep iterating until convergence is reached.

3.2.2 Solving the URANS Equation with SA turbulence model

The flow solver used for this case is a compressible flow solver. The governing equations consist of the continuity equation and the 2D compressible Navier-Stokes (NS) equations, as depicted below in vector form. In this equation, f_{bx} and f_{by} represent the plasma body force per unit mass calculated by Equations (3.25) and (3.26).

$$\frac{\partial W}{\partial t} + \frac{\partial F}{\partial x} + \frac{\partial G}{\partial y} + H = 0 \tag{3.56}$$

In the governing equation, the parameters W, F, G and H are expressed as follow.

$$W = \begin{pmatrix} \rho \\ \rho u \\ \rho v \\ \rho E \end{pmatrix}, F = \begin{pmatrix} \rho u \\ \rho u^2 + p - \tau_{xx} \\ \rho uv - \tau_{xy} \\ \rho uH \end{pmatrix}, G = \begin{pmatrix} \rho v \\ \rho uv - \tau_{yx} \\ \rho v^2 + p - \tau_{yy} \\ \rho vH \end{pmatrix}, H = \begin{pmatrix} 0 \\ -\rho f_{bx} \\ -\rho f_{by} \\ 0 \end{pmatrix} \tag{3.57}$$

The shear stresses can be calculated using the following equations, where τ_{xx}, τ_{xy}, τ_{yx}, and τ_{yy} represent the normal stress in the x-direction, the shear stress in the y-direction, the shear stress in the x-direction, and the normal stress in the y-direction, respectively. μ refers to the dynamic viscosity while μ_t refers to the eddy viscosity calculated by the SA one-equation model. This model will be explained in details at the end of this section.

$$\tau_{xx} = (\mu + \mu_t)[2\frac{\partial u}{\partial x} - \frac{2}{3}\nabla \cdot \overrightarrow{V}] \tag{3.58}$$

$$\tau_{xy} = (\mu + \mu_t)[\frac{\partial u}{\partial y} + \frac{\partial v}{\partial x}] \tag{3.59}$$

$$\tau_{yx} = (\mu + \mu_t)[\frac{\partial v}{\partial x} + \frac{\partial u}{\partial y}] \tag{3.60}$$

$$\tau_{yy} = (\mu + \mu_t)[2\frac{\partial v}{\partial y} - \frac{2}{3}\nabla \cdot \overrightarrow{V}] \tag{3.61}$$

In this simulation, air is treated as an ideal gas with the gas constant $R = 287J/(kg.K)$, the specific ratio $\gamma = 1.4$, and dynamic viscosity $\mu = 1.7894 \times 10^{-5} kg/(m \cdot s)$. The far-field conditions are set to atmospheric conditions, where the pressure $p = 101325Pa$ and the temperature $T = 300K$. The Reynolds-Averaged Navier-Stokes (RANS) Equations are solved to simulate the flow field, where the mean flow is solved by the JST central scheme[41], and turbulence is modeled using the SA one-equation model. In the JST central scheme, Equation (3.56) is integrated over one grid cell, as shown in the following equation.

$$\int\int_A \frac{\partial W}{\partial t} dxdy + \int_\Omega (Fdy - Gdx) + \int\int_A Hdxdy = 0 \tag{3.62}$$

The governing equation is solved by the cell-centered finite volume method where all the information are stored in cell centers. Figure 3.11 shows a sketch of the cell-centered scheme, where (i, j) is the coordinate of the cell center and k is the notation of the sides.

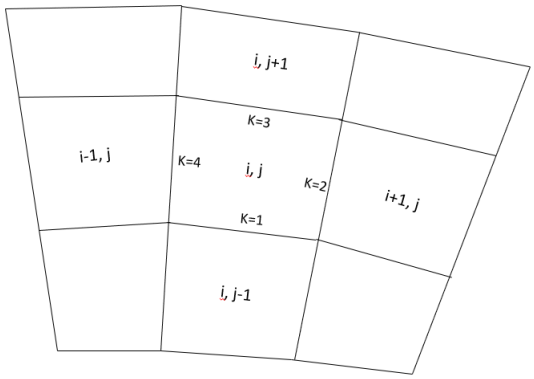

Figure 3.11: Sketch of the mesh for JST method

Equation (3.63) shows the discretized version of the governing equation, where $A_{i,j}$ is the area of the cell (i, j), $Q^c_{i,j}$ is the summation of the convective terms on the four sides of the cell, $Q^v_{i,j}$ is the summation of the viscous terms on the four sides of the cell and $H_{i,j}$ is the source term located at the cell center.

$$\frac{dW_{i,j}}{dt} A_{i,j} + Q^c_{i,j} + Q^v_{i,j} + H_{i,j} A_{i,j} = 0 \tag{3.63}$$

For the momentum in the x-direction, its convective term is calculated by the following equation, where Δx_k is the increment in the x-direction and Δy_k is the increment in the y-direction.

$$Q^c_{i,j} = \sum_{k=1}^{4} (\rho u)_k (u_k \Delta y_k - v_k \Delta x_k) \tag{3.64}$$

In this equation, the momentum terms in the x-direction on four sides can be calculated by averaging the two vertices adjacent to the sides, as shown below.

$$(\rho u)_1 = ((\rho u)_{i,j} + (\rho u)_{i,j-1})/2$$

$$(\rho u)_2 = ((\rho u)_{i,j} + (\rho u)_{i+1,j})/2$$

$$(\rho u)_3 = ((\rho u)_{i,j} + (\rho u)_{i,j+1})/2$$

$$(\rho u)_4 = ((\rho u)_{i-1,j} + (\rho u)_{i,j})/2$$

The velocity terms in the x and y directions u_k and v_k can be calculated by the simple averaging as well. The viscous term $Q^k_{i,j}$ can be calculated in the equation below, where p_k, τ^k_{xx}, τ^k_{yy} are the pressure and shear stress acting on side k.

$$Q^v_{i,j} = \sum_{k=1}^{4} [p_k \Delta y_k - \tau^k_{xx} \Delta y_k + \tau^k_{yx} \Delta x_k] \tag{3.65}$$

The convective terms for the density ρ, the momentum in the y-direction ρv and the energy ρE are calculated in the same way. Solving Equation (3.63) may lead to odd and even decoupling, which can be solved by adding an artificial dissipation term $D_{i,j}$ to the Navier-Stokes equation. The governing equation with the artificial dissipation is shown below.

$$\frac{dW_{i,j}}{dt} A_{i,j} + Q^c_{i,j} + Q^v_{i.j} - D_{i,j} + H_{i,j} A_{i,j} = 0 \tag{3.66}$$

The construction processes of the dissipative terms for each of the four dependent variables

are similar. For the density equation, the artificial dissipation term for cell (i, j) can be calculated by the following equation,

$$(D\rho)_{i,j} = d_{i+\frac{1}{2},j} - d_{i-\frac{1}{2},j} + d_{i,j+\frac{1}{2}} - d_{i,j-\frac{1}{2}} \tag{3.67}$$

where the term $d_{i+\frac{1}{2},j}$ can be calculated by the equation below.

$$d_{i+\frac{1}{2},j} = \frac{A_{i+\frac{1}{2},j}}{\Delta t}[\varepsilon^{(2)}_{i+\frac{1}{2},j}(\rho_{i+1,j} - \rho_{i,j}) - \varepsilon^{(4)}_{i+\frac{1}{2}}(\rho_{i+2,j} - 3\rho_{i+1,j} + 3\rho_{i,j} - \rho_{i-1,j})] \tag{3.68}$$

The coefficients $\varepsilon^{(2)}_{i+\frac{1}{2},j}$ and $\varepsilon^{(4)}_{i+\frac{1}{2},j}$ are expressed in the following equations,

$$\varepsilon^{(2)}_{i+\frac{1}{2},j} = k^{(2)} max(\nu_{i+1,j}, \nu_{i,j})$$

$$\varepsilon^{(4)}_{i+\frac{1}{2},j} = max(0, (k^{(4)} - \varepsilon^{(2)}_{i+\frac{1}{2},j}))$$

where the artificial viscosity ν is predicted by pressure using the following equation, and the parameters $k^{(2)}$ and $k^{(4)}$ are the second order and fourth order dissipation.

$$\nu_{i,j} = \frac{|p_{i+1,j} - 2p_{i,j} + p_{i-1.j}|}{|p_{i+1,j}| + 2|p_{i,j}| + |p_{i-1,j}|}$$

The artificial dissipation terms for the other conservation equations can be calculated by substituting either ρu, ρv, ρE for ρ in the above formulas. The time-stepping scheme used in this simulation is the fourth-order Runge-Kutta scheme. In this research, the simulation results show best agreement with experimental results when $k^{(2)} = 0$, $k^{(4)} = 1.0$. Equation (3.69) shows the simplified version of the governing equation,

$$\frac{dW_{i,j}}{dt} A_{i,j} + R_{i,j} = 0 \tag{3.69}$$

where the residual $R_{i,j}$ is calculated below.

$$R_{i,j} = Q^c_{i,j} + Q^v_{i,j} - D_{i,j} + H_{i,j}A_{i,j}$$

At time step n, the classical fourth order Runge-Kutta scheme is defined as follow.

$$\begin{aligned}
W^{(0)} &= W^n \\
W^{(1)} &= W^{(0)} - \frac{\Delta t}{2} R^{(0)}_{i,j} \\
W^{(2)} &= W^{(0)} - \frac{\Delta t}{2} R^{(1)}_{i,j} \\
W^{(3)} &= W^{(0)} - \Delta t R^{(2)}_{i,j} \\
W^{(4)} &= W^{(0)} - \frac{\Delta t}{6}(R^{(0)}_{i,j} + 2R^{(1)}_{i,j} + 2R^{(2)}_{i,j} + R^{(3)}_{i,j}) \\
W^{n+1} &= W^{(4)}
\end{aligned} \tag{3.70}$$

In the SA one-equation model, a working variable $\tilde{\nu}$ is introduced to evaluate the eddy viscosity and is governed by the transport equation shown below.

$$\frac{D\tilde{\nu}}{Dt} = c_{b1}\tilde{S}\tilde{\nu} + \frac{1}{\sigma}[\nabla \cdot ((\nu + \tilde{\nu})\Delta\tilde{\nu}) + c_{b2}(\Delta\tilde{\nu})^2] - c_{w1}f_w[\frac{\tilde{\nu}}{d}]^2 \tag{3.71}$$

In this equation, the essential parameters are calculated as follow.

$$f_{v1} = \frac{X^3}{X^3 + c^3_{v1}}$$

$$X = \frac{\tilde{\nu}}{\nu}$$

$$\tilde{S} = S + \frac{\tilde{\nu}}{k^2 d^2} f_{v2}$$

$$S = \sqrt{2\Omega_{ij}\Omega_{ij}}$$

$$f_{v2} = 1 - \frac{X}{1 + X f_{v1}}$$

$$\Omega = \frac{1}{2}(\partial u_i)/\partial x_j - \partial u_j/\partial x_i$$

$$f_w = g[\frac{1 + c_{w3}^6}{g^6 + c_{w3}^6}]$$

$$g = r + c_{w2}(r^6 - r)$$

$$r = \frac{\tilde{\nu}}{\tilde{S}k^2d^2}$$

In our research, the essential parameters are set to $cb1 = 0.1355$, $cb2 = 0.622$, $cv1 = 7.1$, $\sigma = 2/3$, $c_w1 = c_{b1}/k^2 + (1 + cb2)/\sigma$, $cw2 = 0.3$, $cw3 = 2$, $k = 0.41$. After calculating the working variable $\tilde{\nu}$ with Equation (3.71), the eddy viscosity μ_t in Equations (3.58) to (3.61) can be obtained by the following equation.

$$\mu_t = \rho f_{v1} \tilde{\mu} \tag{3.72}$$

Chapter 4

Control of the Flow Past a Square Cylinder in a Channel

In this chapter, the flow field is simulated by the SIMPLE algorithm while the plasma control effect is simulated by the Suzen and Huang's model. Before studying plasma control effects, the behavior of the flow field past a square cylinder is studied without using plasma control for the purpose of (1) validating the computational method by comparing with limited available experimental and computational data in open literature; (2) documenting in detail the flow behavior, including lift and drag coefficients, Strouhal number, the flow field pattern for a range of Reynolds numbers; and (3) establishing base flow behaviors for comparison with results under DBD plasma flow control. Figure 4.1 shows a sketch of a square cylinder in the center of a channel. Breuer et al.[42] used numerical methods to study the channel flow around a square cylinder. In his simulation, the length of the channel $L = 1.0m$, the diameter of the square cylinder $D = 0.02m$ and the height of the channel $H = 0.16m$, giving a blockage ratio $D/H = 0.125$. The cylinder is located on the center line of the channel $0.25m$ away from the inlet, and $0.75m$ away from the exit. In the first part of this section, we use the same configurations and boundary conditions as their simulation. At the inlet, the

flow velocity is parallel to the channel axis and satisfies the laminar fully-developed parabolic profile with the maximum velocity U_0 at the center line. At the outlet, the velocities in both x and y directions satisfy the Neumann boundary condition. The no-slip condition is applied on the channel walls as well as the surface of the cylinder.

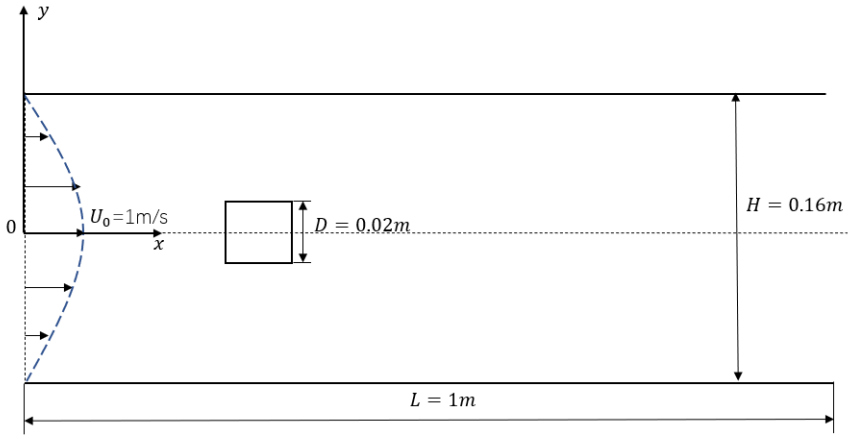

Figure 4.1: Square cylinder in $2D$ channel

Figure 4.2 shows a sketch of the boundary conditions for the square cylinder case. The no-slip and no-penetration boundary conditions are implemented on the walls of the channel and the square cylinder. The Dirichlet boundary condition is implemented on the inlet and the Neumann boundary condition is implemented on the outlet. The initial condition is zero velocity everywhere in the flow field.

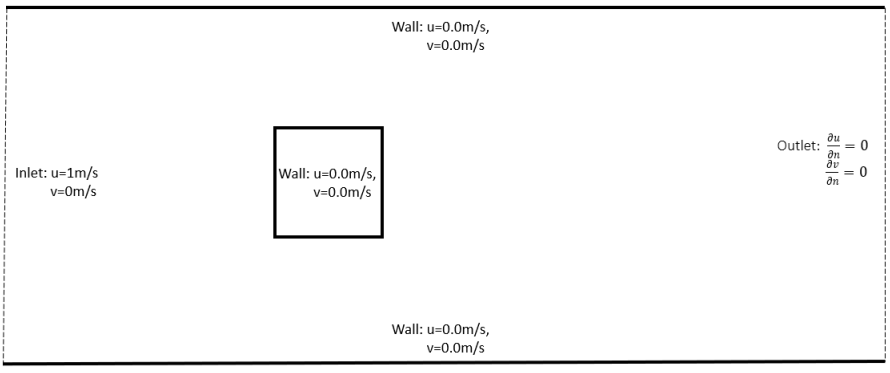

Figure 4.2: The boundary condition for the square cylinder case

Computations are performed using non-dimensionalized variables based on the cylinder diameter D and maximum free-stream velocity U_0. The lift coefficient C_L, drag coefficient C_D, the Strouhal number St and the Reynolds number Re are calculated by the following equations, where F_L, F_D, f and ν are the lift force, drag force, frequency and kinematic viscocity.

$$C_L = \frac{F_L}{\frac{1}{2}\rho U_0^2 D}$$

$$C_D = \frac{F_D}{\frac{1}{2}\rho U_0^2 D}$$

$$St = \frac{fD}{U_0}$$

.

$$Re = \frac{U_0 D}{\nu}$$

4.1 Flow Past a Square Cylinder in a Channel Without Control

In this section, simulations are conducted for Reynolds numbers ranging from 1 to 300 and the behavior of the flow field under different Reynolds numbers are analyzed in detail. When the Reynolds number is really small, the flow field is steady, symmetric with no separation in the wake. Figure 4.3 shows the streamlines when the Reynolds number $Re = 1$, which represents the typical flow field for very small Reynolds numbers.

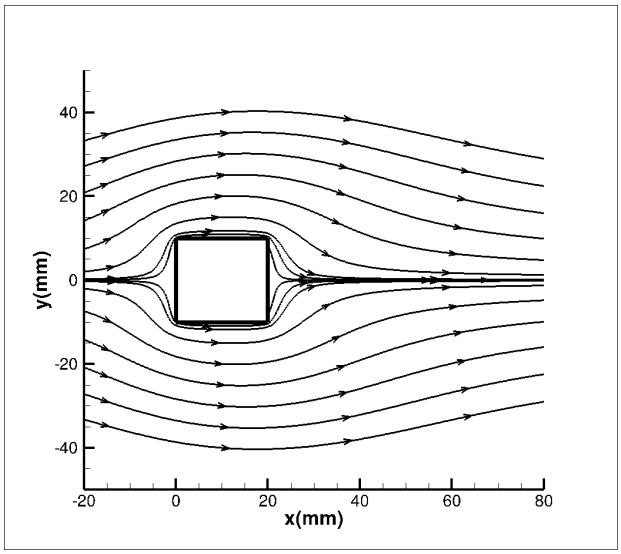

Figure 4.3: Streamlines for $Re = 1$.

When the Reynolds number increases beyond 5, two steady symmetric vortices are generated in the wake. Figure 4.4 shows the streamlines for $Re = 10$ and $Re = 50$, where the flow remains attached on both the top and bottom surfaces but there is separation located at the two rear corners of the square cylinder. As a consequence, two symmetric vortices are generated in the wake after separation although the flow field is still steady. The size of the vortices for $Re = 50$ is larger than that for $Re = 10$. Although not shown here, our computations at other Reynolds numbers show that for $1 < Re < 50$, the flow field is always steady and symmetric. The length of the vortex is measured by the distance between the square cylinder and the first point where the axial flow velocity changes sign from negative (in the recirculation zone) to positive (after reattachment) along the centerline. The recirculation length increases with increasing Reynolds number, as can be seen in Figure 4.5, where L_r/D represents the length of the vortex normalized by the diameter of the square clylinder. These results show very good agreement with Breuer et al.[42]'s simulation results.

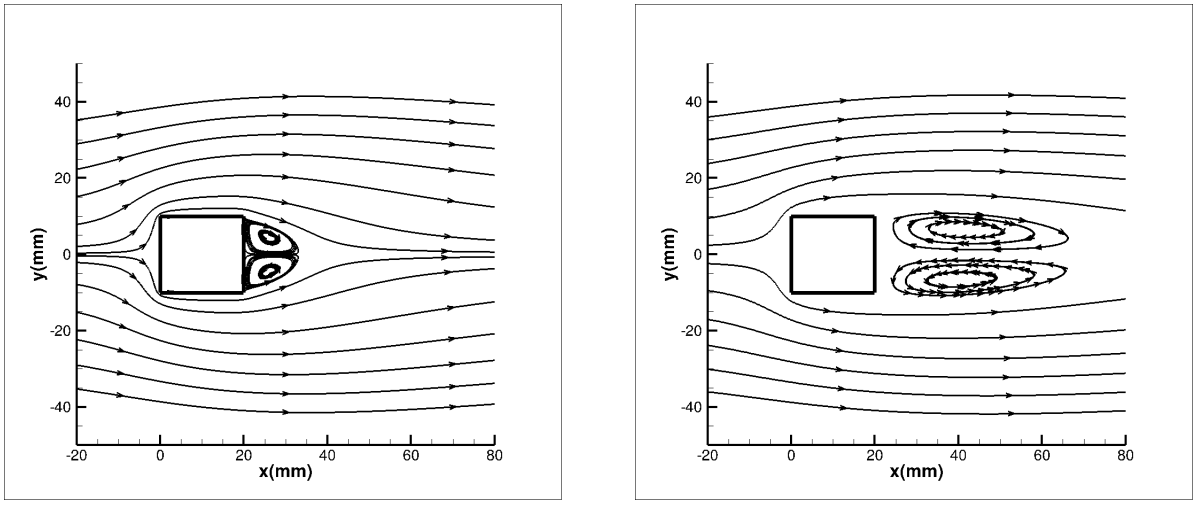

(a) $Re = 10$ **(b)** $Re = 50$

Figure 4.4: Streamlines for low Reynolds number flows

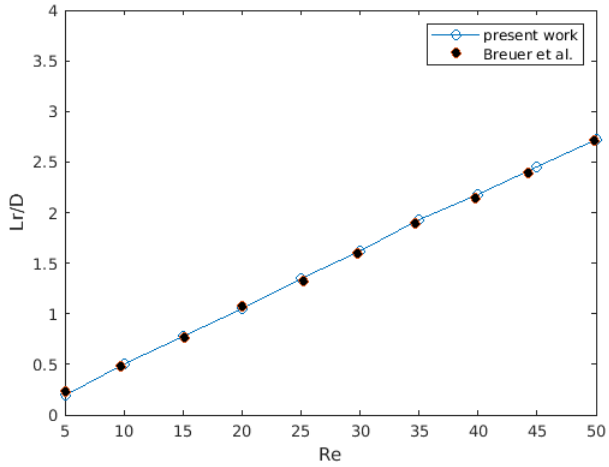

Figure 4.5: Vortex length in the wake

Figure 4.6 plots the drag coefficient vs Reynolds number ranging from $Re = 1$ to $Re = 50$, where the flow is steady, and the results agree with those from Breuer et al.[42]. The drag force is comprised of pressure drag and friction drag. The pressure drag is caused by the pressure difference between the front and rear sides while the friction drag is caused by the velocity gradient at the top and bottom of the cylinder. The flow onto the front side of the cylinder reaches approximately the stagnation pressure, but part of the kinetic energy is lost

due to viscosity and flow separation as the flow travels to the trailing edge. As a result, the stagnation pressure at the trailing edge is considerably lower than that at the leading edge. The drag force is mainly caused by this pressure difference between the front and rear surfaces.

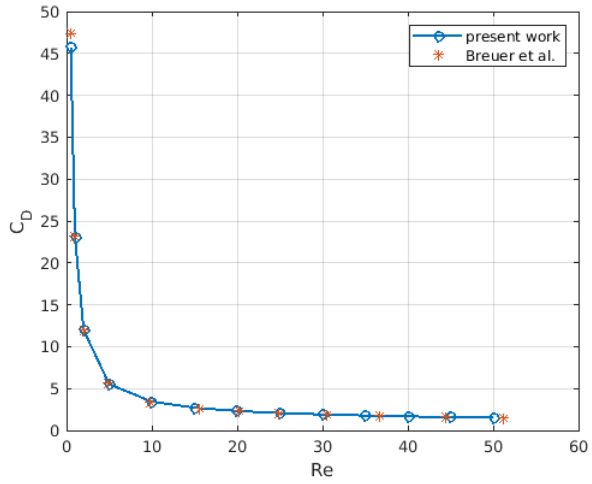

Figure 4.6: Drag coefficient for steady-state flow field.

Although the flow field starts to become unsteady when $Re = 60$, the oscillation only starts to become obvious when $Re = 80$, so this case is chosen to demonstrate the regularly oscillating flow field. Figure 4.7 shows the time evolution of the flow field for $Re = 80$. Our computed results initially converge to a nearly symmetric flow as shown in Figure 4.7(a). Two elongated vortices appear symmetrically behind the cylinder at the non-dimensional time $\frac{tU_0}{D} = 6.25$. As the computation continues, the symmetry of the vortices breaks down. The bottom vortex gets elongated further and is eventually shed downstream. The top vortex then grows in size and is eventually shed downstream, too. Ultimately, the computation yields to a periodic flow pattern with vortices alternately shedding from the two trailing edge corners of the cylinder. The flow on the top and bottom surfaces of the cylinder remains attached, albeit unsteady.

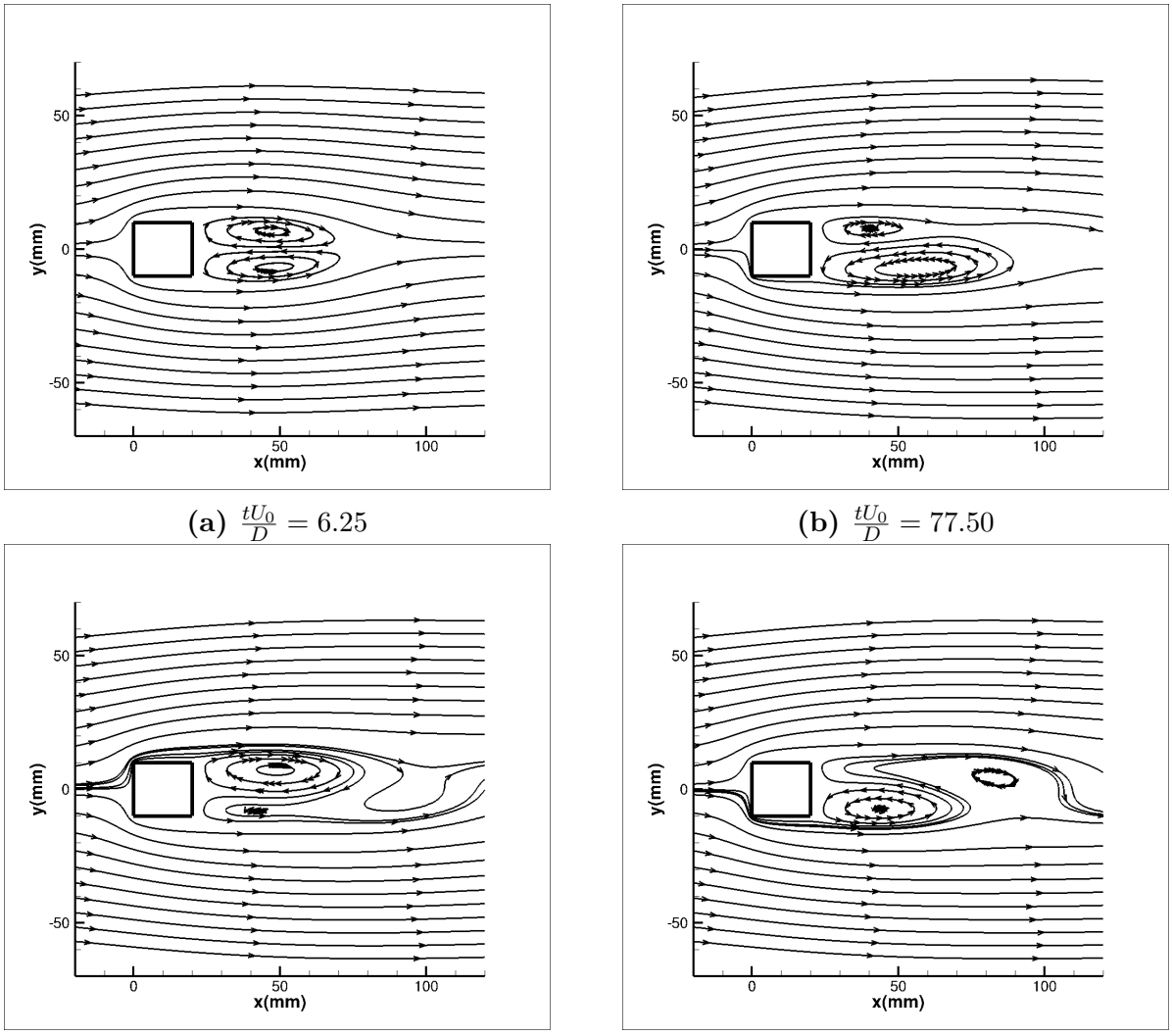

(a) $\frac{tU_0}{D} = 6.25$ **(b)** $\frac{tU_0}{D} = 77.50$

(c) $\frac{tU_0}{D} = 90.00$ **(d)** $\frac{tU_0}{D} = 93.75$

Figure 4.7: Streamlines at different non-dimensional time for $Re = 80$

Figure 4.8 shows the lift and drag coefficients vs time for $Re = 80$ after the flow becomes fully periodic. The lift fluctuation is produced mainly by the pressure oscillation on top and bottom, and this oscillation is induced by the oscillation in the wake.

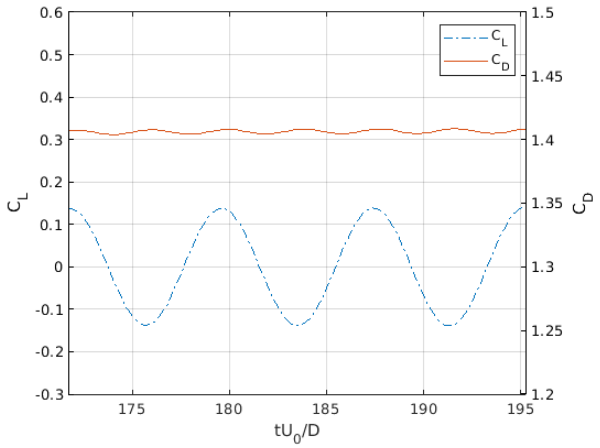

Figure 4.8: Lift and drag coefficients for $Re = 80$.

Figure 4.9 shows the Fourier spectrum for both the lift and drag coefficients. There is only one dominant frequency for either the lift or drag. The lift coefficient oscillates at the frequency of $f = 6.154Hz$, corresponding to a Strouhal number of $St = \frac{fD}{U_0} = 0.123$. Since the oscillation in the lift coefficient is caused by the vortex shedding in the wake, the frequency of the lift coefficient equals to the vortex shedding frequency. Consider the time instant shown in Figure 4.7(c) when a strong vortex trails the top corner of the cylinder, the velocity on the top surface is higher than that on the bottom surface, resulting in a positive lift coefficient. By the time when the top vortex is shed downstream and the flow is dominated by the bottom vortex behind the lower corner of the cylinder as shown in Figure 4.7(d), the velocity on the lower surface becomes greater than that on the top surface. Therefore, the lift becomes negative. The drag coefficient, however, does not distinguish the top or bottom surfaces in terms of either skin friction or pressure drag. Each cycle of oscillating velocity on either top and bottom of the two surfaces gives rise to an oscillating cycle of the drag coefficient. Therefore, the drag coefficient oscillates at exactly twice the frequency of the lift coefficient.

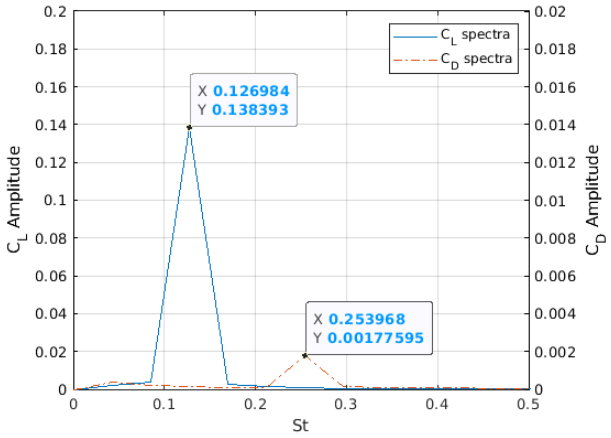

Figure 4.9: Fourier spectrum of C_L and C_D for $Re = 80$.

For $60 < Re < 200$, the lift and drag coefficients behave similarly as in the case $Re = 80$. When $Re > 200$, the vortex shedding becomes more irregular and the flow starts to show signs of becoming turbulent. Figure 4.10 shows the lift and drag coefficients for $Re = 300$. For this Reynolds number, the sinusoidal oscillation no longer exists.

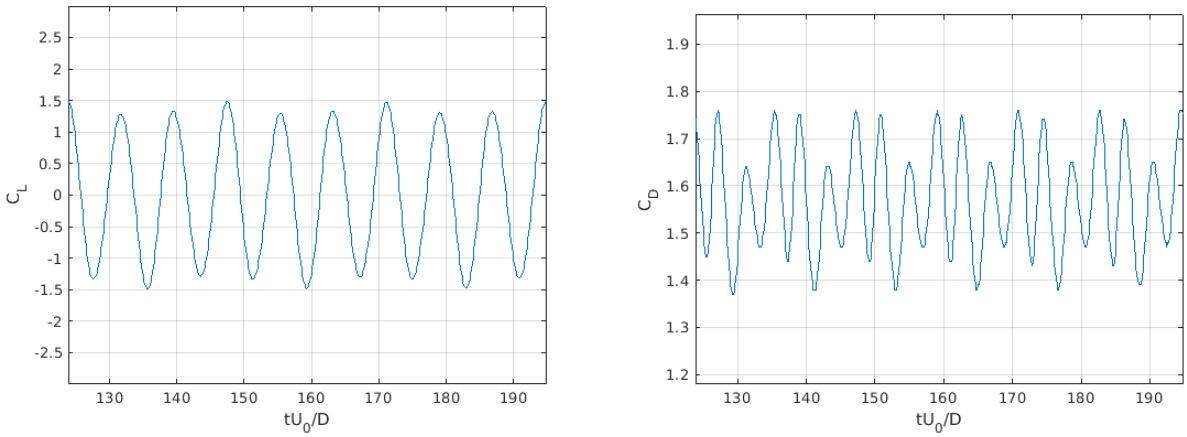

(a) Lift coefficient **(b)** Drag coefficient

Figure 4.10: Lift and drag coefficients for $Re = 300$.

Figure 4.11 shows the streamlines for $Re = 300$ at different time instants. Apart from the von Kármán vortex street in the wake, two vortices appear alternately on top and bottom of the cylinder. When the vortex on the top breaks, another vortex appears on the bottom, and

vice versa. Due to the interaction of these vortices, three different frequencies appeared for the lift fluctuation, as can be seen in Figure 4.12. The dominant non-dimensional frequency $St = 0.127$ corresponds to the vortex shedding frequency in the wake. The lower and higher non-dimensional frequencies $St = 0.042$ and $St = 0.211$ are related to the formation and destruction of the vortex on each side surface and their interaction with the main vortex shedding.

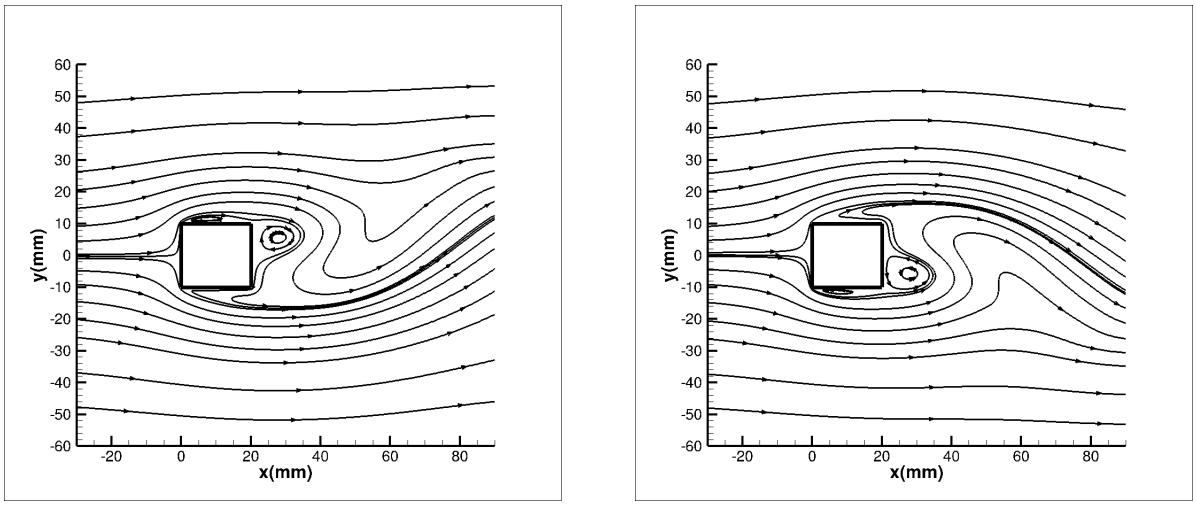

(a) $\frac{tU_0}{D} = 208.5$ **(b)** $\frac{tU_0}{D} = 220.125$

Figure 4.11: Streamlines at different non-dimensional times for $Re = 300$.

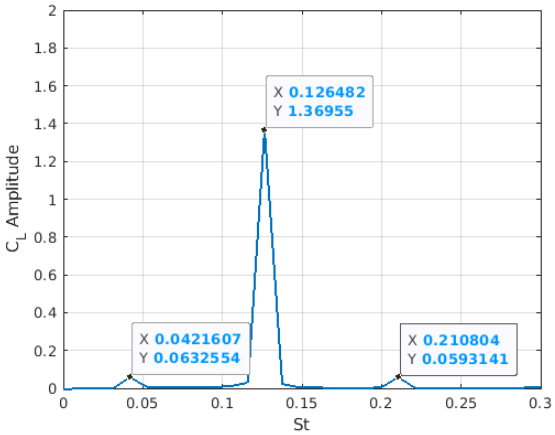

Figure 4.12: Fourier spectrum of C_L for $Re = 300$.

Figure 4.13 shows the peak to peak oscillation magnitudes of the lift and drag coefficients vs

Reynolds number. The peak to peak magnitudes of both the lift and drag increase with the Reynolds number. Figure 4.14 shows the average drag coefficient and the Strouhal number vs Reynolds number, and these results agree very well with those by Breuer et al.[42].

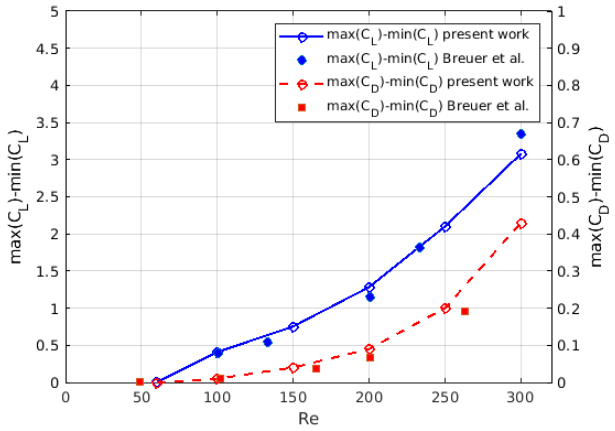

Figure 4.13: Lift and drag peak to peak vs Reynolds number.

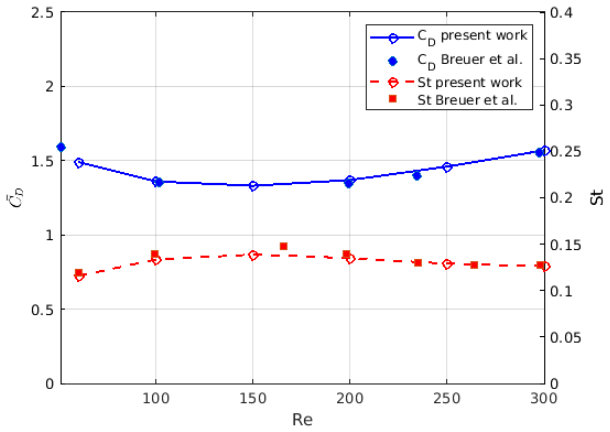

Figure 4.14: Average drag coefficient and Strouhal number vs Reynolds number.

Experimental results for the vortex shedding behind the square cylinder under different Reynolds numbers are scarce. The only source can be found was the experimental results by Okijima et al.[43], which were carried out at blockage ratio $D/H \leq 0.036$. Sohankar et al.[44] did a numerical simulation using the blockage ratio $D/H = 0.056$. Figure 4.15 compares the average drag coefficient between the present simulation, the experimental data

by Okijima et al.[43] and the numerical results by Sohankar et al[44]. On consideration of the blockage effects and the experimental uncertainties, these results may be regarded as in good agreement.

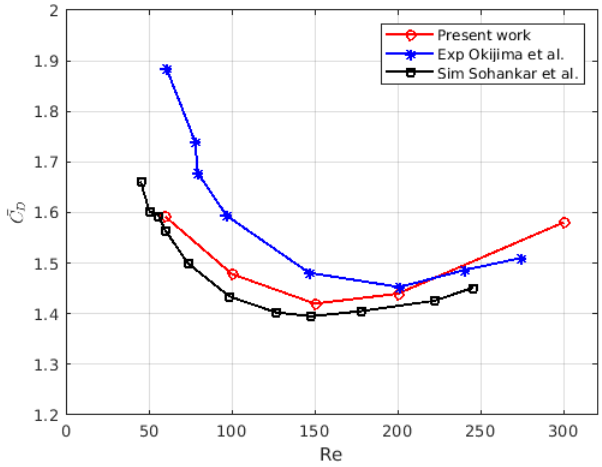

Figure 4.15: Average drag coefficient vs Reynolds number.

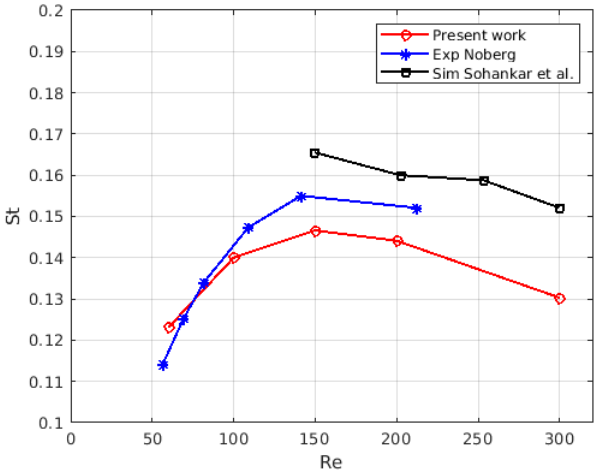

Figure 4.16: Strouhal number vs Reynolds number.

Noberg[45] presented measurement data of Strouhal number in a range of Reynolds numbers for a slightly different channel configuration. In his experiment, the height and length of the channel are set to $H = 1.25m$ and $L = 2.90m$, respectively. The cylinder of the same size is placed $0.7m$ away from the inlet. As can be seen in Figure 4.16, computational results in the

present work agree well with Noberg's experimental data at low Reynolds numbers. They show the correct behavior between the Strouhal number and the Reynolds number although the computational value falls under the experimental value for Reynolds number 150 and greater. Sohankar et al.[44]'s simulation results show similar trend for Reynolds numbers higher than 150. However, they over predicted the Strouhal number. For the remainder of this chapter, we will use the same geometrical dimensions as Noberg's paper.

A grid refinement study is performed on three successively refined grids. Grids 1, 2, and 3 have 150, 200, and 250 grid points, respectively, on each side of the square cylinder. All four sides of the cylinder have the same number of grid points and the grid in the directions normal to the walls are refined accordingly to keep the same grid interval size in both the normal and tangential direction on the wall. Table 4.1 lists the computed Strouhal number and amplitude of the lift coefficient on the three different grids for Reynolds numbers ranging from 100 to 300. These results demonstrate sufficient grid convergence on the three grid systems. Table 4.2 shows results of refining the time step on Grid 2. Excellent convergence is achieved with respect to time step refinement as well. The computational results presented above and in the following sections are computed on Grid 2 (total number of 244989 grid points) with a time step size of $0.0025s$ (more than 50 time intervals within one oscillation period of flow).

	St			$C_{L,rms}$		
Re	grid 1	grid 2	grid 3	grid 1	grid 2	grid 3
100	0.134	0.134	0.133	0.145	0.146	0.151
150	0.140	0.140	0.138	0.265	0.267	0.278
200	0.135	0.135	0.134	0.453	0.453	0.460
250	0.129	0.129	0.129	0.719	0.719	0.713
300	0.126	0.127	0.125	0.961	0.972	0.959

Table 4.1: Computed Strouhal number and amplitude of lift coefficient on three successively refined grids.

	St		$C_{L,rms}$	
Re	$dt = 0.0015s$	$dt = 0.0025s$	$dt = 0.0015s$	$dt = 0.0025s$
100	0.134	0.134	0.145	0.146
150	0.140	0.140	0.267	0.267
200	0.135	0.135	0.453	0.453
250	0.129	0.129	0.718	0.719
300	0.127	0.127	0.970	0.972

Table 4.2: Computed Strouhal number and amplitude of lift coefficient with two successively refined time steps on Grid 2.

4.2 Flow with Plasma Actuator Control

This section studies the flow around a square cylinder under plasma control, where the plasma body force is simulated by the Suzen and Huang model while the flow field is simulated by the SIMPLE algorithm. The first step is the calibration process, where many parameters in the Suzen and Huang model are acquired by calibrating with experimental results. Since

experimental data on the plasma control around a square cylinder is very limited, we used Xue et al.[12]'s case for the calibration process, where a single DBD plasma actuator is installed on top of a flat plate. Figure 4.17 shows a sketch of the DBD plasma actuator, including the dimensions of each component. This device consists of two electrodes separated by a dielectric layer. The length of the exposed electrode is $2mm$ while the length of the buried electrode is $4mm$, both having a thickness of $0.066mm$. The vertical distance between two electrodes is $0.3mm$. The relative dielectric constant for air $\varepsilon_{r1} = 1.0$ and the relative dielectric constant for the dielectric material $\varepsilon_{r2} = 3.2$. The input signal is a sinusoidal electric signal whose peak-to-peak voltage equals to $14kV$ and the carrier frequency equals to $8kHz$.

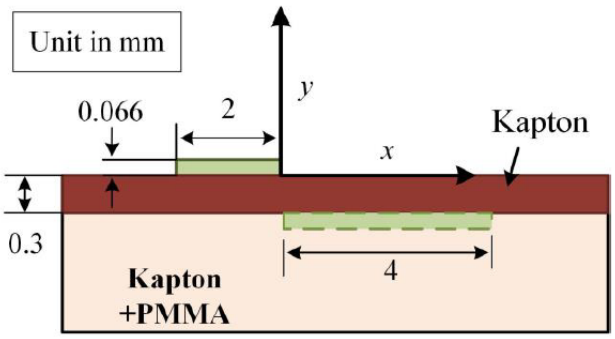

Figure 4.17: Sketch of the DBD plasma actuator [12]

As explained in the previous chapter, the parameters σ, ρ^c_{max} and λ_d are obtained by calibrating with experimental results. It is discovered that when $\sigma = 10mm$, $\rho_c^{max} = 0.004C/m^3$ and $\lambda_d = 0.3mm$, the simulation results show the best agreement with experimental results for the flat plate case, which will be discussed in details in the next few pages. Figure 4.18 shows the simulated potential and net-charge density distribution in the domain under this set of parameters.

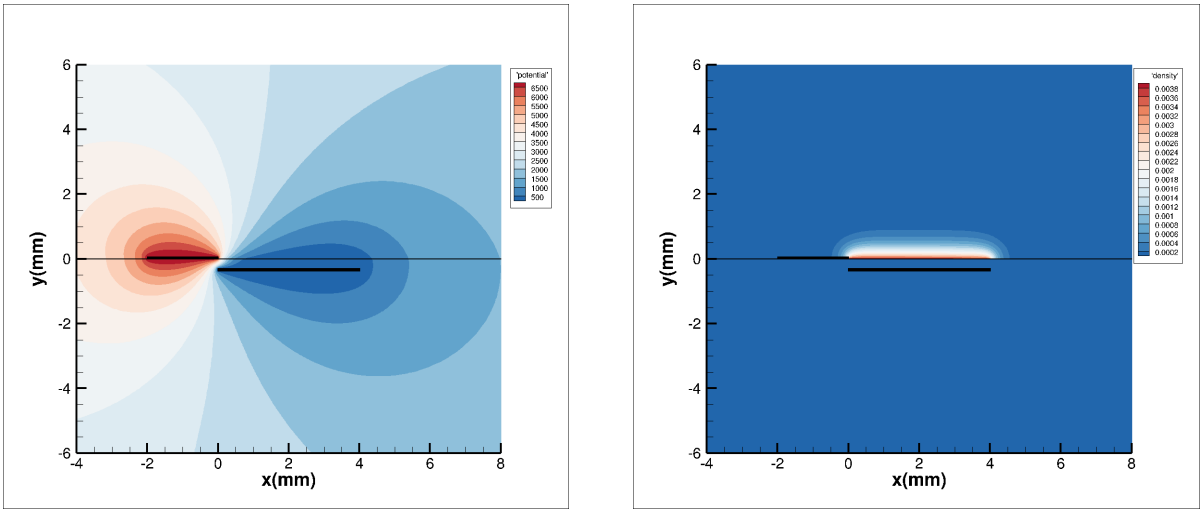

(a) Potential **(b)** Net-charge density

Figure 4.18: Potential and net-charge density distribution

Figure 4.19 shows the plasma body force in the x and y directions, which is concentrated in a small area between the exposed and buried electrodes. Although the region of influence for the body force is small, its magnitude is quite large and thus able to cause significant influence on the flow field.

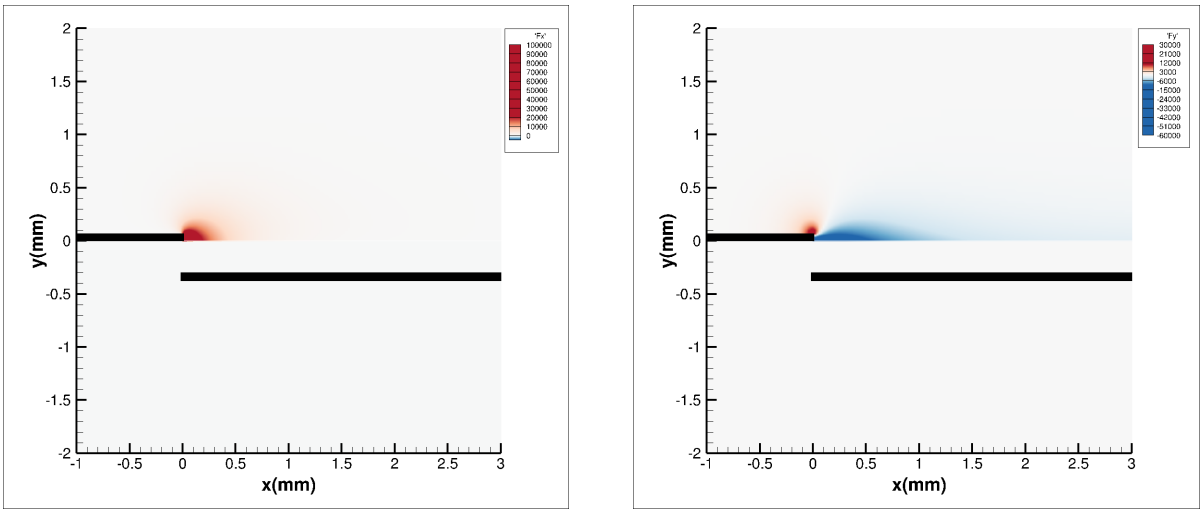

(a) x-direction **(b)** y-direction

Figure 4.19: The plasma body force in the x and y directions

Air is quiescent initially and the flow is only induced by the plasma body force. A few seconds

after the plasma actuator is turned on, the flow field becomes stable and the vortex motion within each cycle repeats itself. As explained in Chapter 3, the plasma effect is simulated as a body force and treated as a source term in the Navier-Stokes equations. Figure 4.20 shows the boundary condition, where the no-slip condition is implemented on the surface of the flat plate and the Neumann boundary condition is implemented on the other three sides.

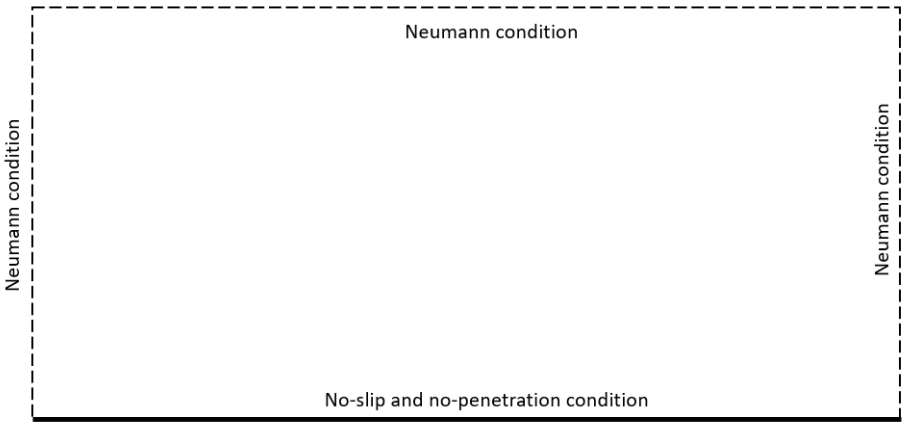

Figure 4.20: The boundary conditions for the flat plate case

The experimental case used for calibration has the duty-cycle frequency $f = 10Hz$ and duty-cycle ratio $\tau = 0.5$. Figure 4.21 shows the simulation and experimental contours for this case. The picture is taken at one-tenth of a duty-cycle period, $t = \frac{1}{10}T$. For both simulation and experiment, there are two vortices in the flow field. The main vortex (pictured in red) is rotating in the counter-clockwise direction and the secondary vortex (pictured in blue) is rotating in the clockwise direction. The simulated results compare relatively well with the experimental results despite some slight differences. According to the picture, the biggest difference between the simulation and experiment is the "red tail", indicating that the wall jet starts from the plasma actuator in the simulation but a distance away in the experiment. The difference in wall jet is likely to be induced by the difference of plasma body force between the simulation and experiment. In the simulation, the body force is concentrated at the intersection between the exposed and buried electrode. In the experiment, the body force is likely to start some distance away from the DBD plasma actuator.

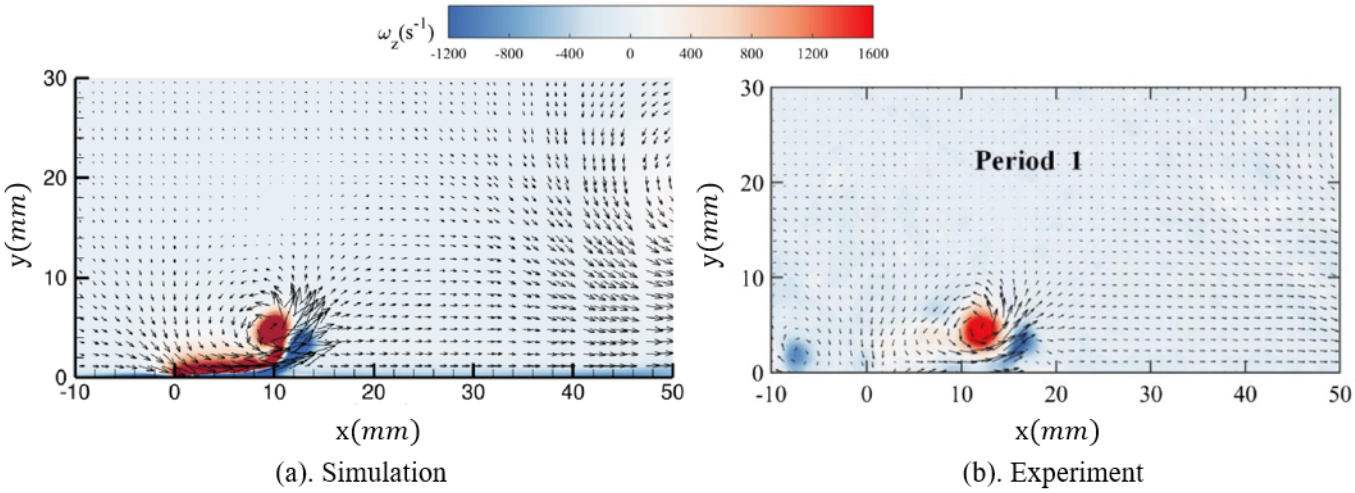

Figure 4.21: Vortex propagation when $f = 10Hz$ at $t = \frac{1}{10}T$.

To study the plasma control effects on the flow around a square cylinder, three different configurations are shown in Figure 4.22. In Case 1, a pair of plasma actuators are placed symmetrically on top and bottom of the square cylinder, where the wall jets induced by the DBD actuators point downstream in the stream-wise direction. In Case 2, a pair of actuators are installed on the front surface, where the top actuator generates a jet running upwards and the bottom actuator generates a jet running downwards. In Case 3, a pair of opposing actuators are installed on the rear surface and two wall jets are running into each other, colliding in the middle. For the present work, only steady-state actuation is considered for this project.

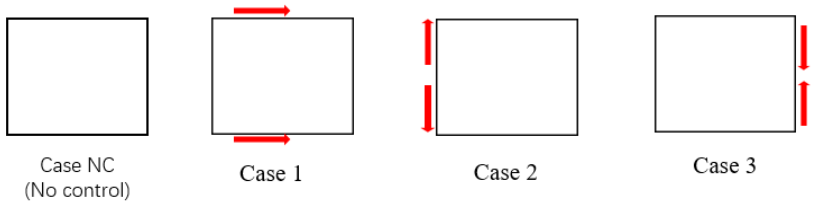

Figure 4.22: Arrangements of plasma actuators on a square cylinder.

The flow control effect is studied under two different Reynolds numbers, $Re = 100$ and

$Re = 200$. For each Reynolds number, all three different arrangements shown in Figure 4.22 will be tested to determine the optimal case. Under each case, both the position and the plasma body force strength will be varied. The plasma body force strength is measured by $C_{pow} = \frac{Power}{\frac{1}{2}\rho U_0^3 D}$, where $Power$ is the power input of the plasma actuator and $\frac{1}{2}\rho U_0^3 D$ represents the kinetic energy in the free-stream.

4.2.1 Case 1: Plasma Actuators Mounted on Top and Bottom

At $Re = 100$, the flow separates at the trailing edge and a Von Kármán vortex street is formed in the wake. Although the flow on top and bottom remains attached to the surface, the oscillations in the wake lead to oscillations of pressure and flow velocity on top and bottom of the cylinder, causing fluctuations in lift and skin friction drag. The pressure drag is directly affected by vortex shedding in the wake. Under this Reynolds number, the average drag coefficient $\bar{C}_D = 1.449$, and the root mean square lift fluctuation is $C_{L,rms} = 0.203$. At Reynolds number $Re = 200$, the flow separates at the leading edge and apart from the vortices in the wake, two vortices also appeared on top and bottom of the cylinder similar to the situation shown in Figure 4.11. Due to the two additional vortices on top and bottom, the flow field fluctuates more intensely compared to the case at $Re = 100$, resulting in a significantly higher root mean square lift coefficient $C_{L,rms} = 0.452$. The average drag coefficient does not change much, i.e. $\bar{C}_D = 1.440$.

The plasma actuators on the top and bottom surfaces of the cylinder each generate a jet in the positive x-direction. Their combined effect results in a reduction of the wake size and the fluctuation. The location of the plasma actuator is measured by the non-dimensional distance x/D from the leading edge to the right side of the exposed electrode, where D is the diameter of the cylinder. To find out the optimum location, the plasma actuators are installed at $x/D = 0.1$, $x/D = 0.5$, and $x/D = 0.75$. Different power coefficients are applied

for each actuator location to study the effect of body force strength.

We consider first the case when $x/D = 0.75$ and $C_{pow} = 0.4752$ for $Re = 100$. The flow field under this condition is shown in Figure 4.23. The width of the wake is slightly reduced compared to the case without plasma control. Figure 4.24 shows the lift and drag coefficients with and without plasma control. The label NC in the figure indicates No Control.

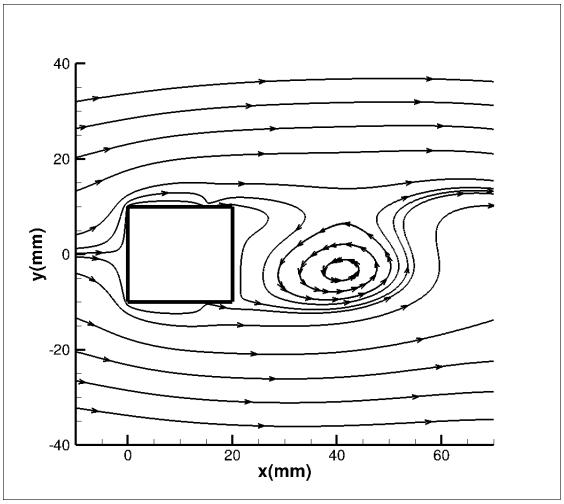

Figure 4.23: Flow field for Case 1 at one instant

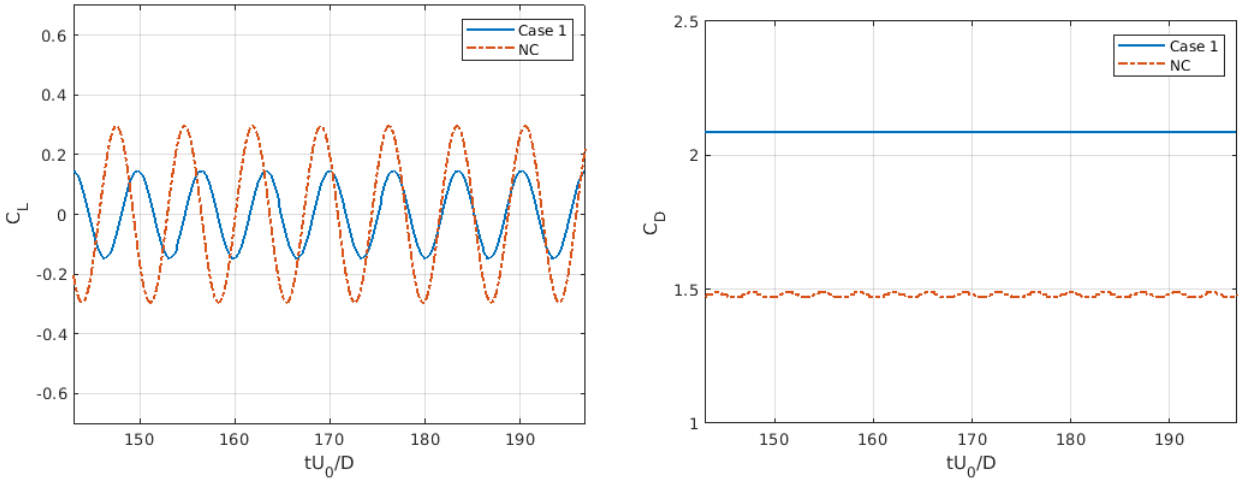

(a) Lift coefficient **(b)** Drag coefficient

Figure 4.24: Lift and drag coefficients for $Re = 100$, $x/D = 0.75$,$C_{pow} = 0.4752$, Case 1

The plasma actuators in this configuration significantly reduces the amplitudes of both the

lift and drag fluctuations. However, the average drag coefficient is increased by approximately 41% due to the increase of shear stress on the two side surfaces of the cylinder. Table 4.3 shows the pressure and friction drag coefficients under different power inputs for this case. While the pressure drag shows a slight overall decreasing trend, the friction drag is increased significantly. The two jets on the side surfaces increase the velocity in the vicinity of the wall significantly. Due to the no-slip condition, the shear stress increases with the increase of velocity gradient in the boundary layer. The pressure drag is caused mainly by the pressure difference between the front and rear surface, and the plasma actuators have little effect over it. Fourier analysis of the lift coefficient shows slightly increased frequency of the vortex shedding compared to the case without plasma control. The Strouhal number increases from 0.139 to 0.148 and 0.180 to 0.182 for the Reynolds number 100 and 200 cases, respectively.

C_{pow}	$\bar{C}_D$	$\bar{C}_{D_P}$	$\bar{C}_{D_F}$
0.0	1.4490	1.4082	0.0409
0.0028	1.5183	1.4275	0.0908
0.0579	1.6795	1.3855	0.2940
0.2196	1.8832	1.3400	0.5432
0.4752	2.0900	1.3000	0.7900

Table 4.3: Pressure and friction drag under different power inputs for $x/D = 0.75$

Figure 4.25 shows the lift fluctuation and the average drag vs power input for different locations of plasma actuators when $Re = 100$. The suppression of lift fluctuation gets better when the plasma actuators are installed further away from the leading edge. Regardless where the actuators are installed, the suppression of lift fluctuation always gets better with the increase of power input. When two actuators are installed $x/D = 0.75$ away from the leading edge and the power coefficient reaches about 0.4752, the standard deviation of the lift coefficient is reduced by almost 50%. The average drag always increases with the power input, but the position of the actuators has little influence over the average drag coefficient.

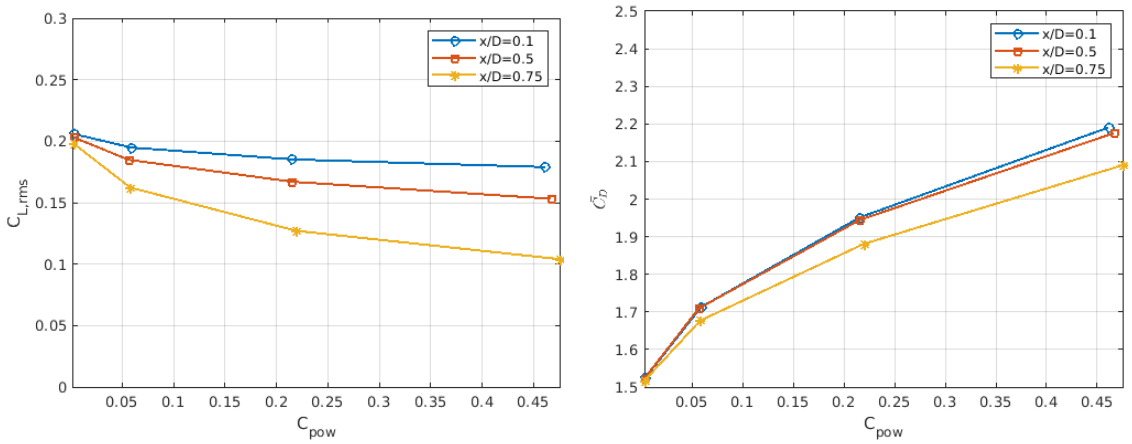

(a) Lift fluctuation **(b)** Average drag coefficient

Figure 4.25: Lift fluctuation and average drag vs actuator power input for $Re = 100$ under different actuator arrangements, Case 1

Figure 4.26(a) shows the lift fluctuation vs power input for $Re = 200$. The control effect still gets better as the actuators are installed further away from the leading edge. Figure 4.26(b) shows the average drag coefficient vs power input. The general behavior of the flow is similar to that for $Re = 100$.

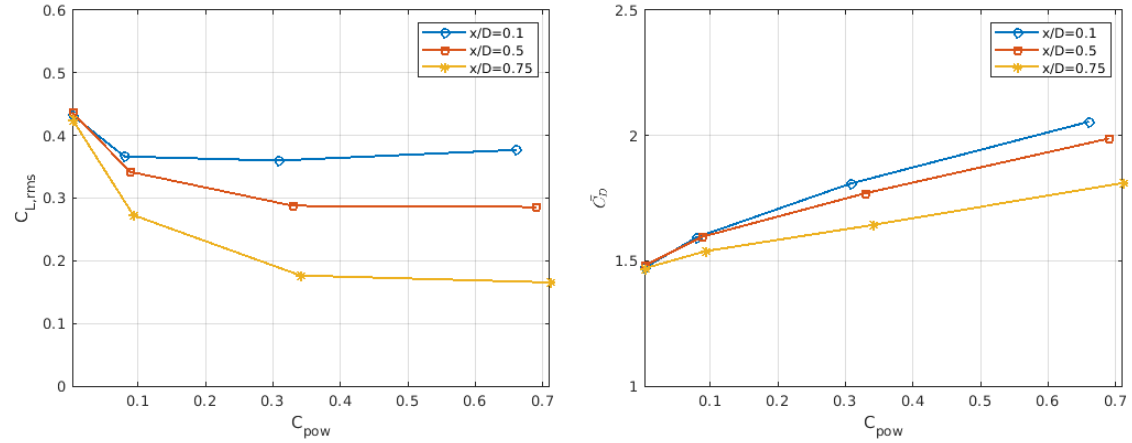

(a) Lift fluctuation **(b)** Average drag coefficient

Figure 4.26: Lift fluctuation and average drag vs actuator power input for $Re = 200$ under different actuator arrangements, Case 1.

4.2.2 Case 2: Plasma Actuators Mounted on the Front Surface

In this case, two plasma actuators are installed on the front surface. The plasma actuator above the center line is referred to as the top actuator while the plasma body force below the center line is referred to as the bottom actuator. The bottom actuator generates a body force pointing downwards while the top actuator generates a body force pointing upwards, inducing two cross stream jets on the front surface of the cylinder. These two jets tend to induce more disturbance and increase the degree of flow separation from the two leading edge corners of the cylinder. Due to these wall jets, the oscillation becomes even stronger, causing the pressure fluctuation on the surface of the cylinder to increase. At $Re = 100$, both the lift fluctuation and the average drag coefficient are increased by the plasma body force as shown in Figure 4.27. Similar results are obtained for $Re = 200$. These computational results demonstrate that mounting the plasma actuators on the front surface of the cylinder is not a viable choice for reducing either lift or drag or their oscillations.

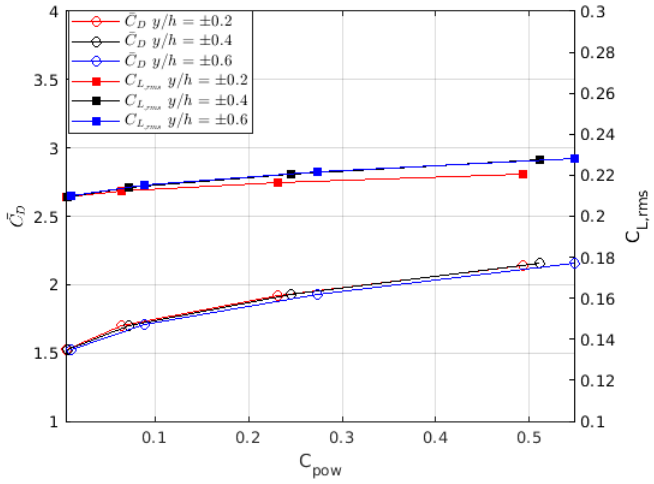

Figure 4.27: Lift fluctuation and average drag vs actuators' power input at $Re = 100$, Case 2.

4.2.3 Case 3: Plasma Actuators Mounted on the Rear Surface

Computations show that this configuration is the most effective for reducing vortex shedding and drag. In this case, the two jets on the rear surface of the cylinder bring the flow from the two rear corners of the cylinder into the center line, reducing the size of the separation vortices in the wake. Consequently, the flow suffers a smaller base pressure loss and recovers to a higher stagnation pressure on the back surface of the cylinder. The plasma also directly adds to the kinetic energy of the base flow and thus the stagnation pressure. In this case, the plasma body force has little influence on the top and bottom surface so the friction drag is not much affected. Since the pressure drag is reduced and the friction drag is not affected, the total drag coefficient is decreased by the plasma body force. This is verified by Table 4.4, where the pressure drag decreases rapidly with plasma power input while the friction drag decreases at a slower rate. The suppression of lift fluctuation is achieved by the suppression of vortex shedding in the wake.

C_{pow}	$\bar{C}_D$	$\bar{C}_{D_P}$	$\bar{C}_{D_F}$
0.0	1.4490	1.4082	0.0409
0.0019	1.4222	1.3828	0.0394
0.0565	1.2052	1.1667	0.0385
0.2259	0.9356	0.8992	0.0364
0.6966	0.4361	0.4041	0.0321

Table 4.4: Friction and pressure drag under different power inputs at $y/h = \pm 0.8$

Figure 4.28 shows the lift fluctuation and the average drag vs the plasma power coefficient for $Re = 100$. Three installation locations are considered, measured by the distance of the actuators from the center point of the rear side. The $y/h = \pm 0.8$ distance location corresponds to having the pair of DBD actuators mounted flush with the back side of the

cylinder and the leading edge of the exposed electrode aligned exactly at the rear corners of the cylinder. Both the lift fluctuation and the average drag decrease with increasing power input and the distance between the two actuators. The $y/h = \pm 0.8$ case appears to have the most effective mounting location for the plasma actuators. With this mounting configuration, the lift fluctuation is reduced to 0 when the actuator power input increases to $C_{pow} = 0.7$.

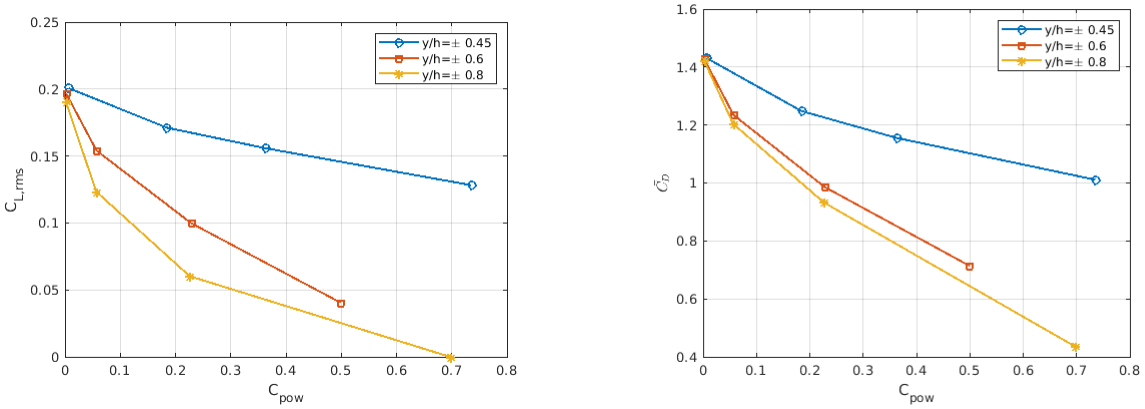

(a) Lift fluctuation **(b)** Average drag coefficient

Figure 4.28: Lift fluctuation and average drag vs C_{pow} for $Re = 100$ under different actuator arrangements, Case 3

Figure 4.29 shows the flow field under different plasma power input when the two actuators are installed at $y/h = \pm 0.8$. When the power input is set to $C_{pow} = 0.001$, the effect of the plasma body force on the flow field is very small. The Von Karman vortex street still exists in the wake, as shown in Figure 4.29(a). When the power input is increased to $C_{pow} = 0.226$, two new vortices are generated by the DBD actuators over the rear surface of the cylinder, as shown in Figure 4.29(b). The original separation vortex from the top corner is reduced in strength and pushed downstream by the newly generated vortex. A similar situation appears at the instant when the flow is dominated by the vortex shed from the lower corner of the cylinder. When C_{pow} increased to 0.697, the pair of new vortices generated by the plasma actuators become strong enough to stabilize the original separation vortices, and

the flow becomes steady and symmetric, as shown in Figure 4.29(c). Consequently, the lift fluctuation is completely suppressed.

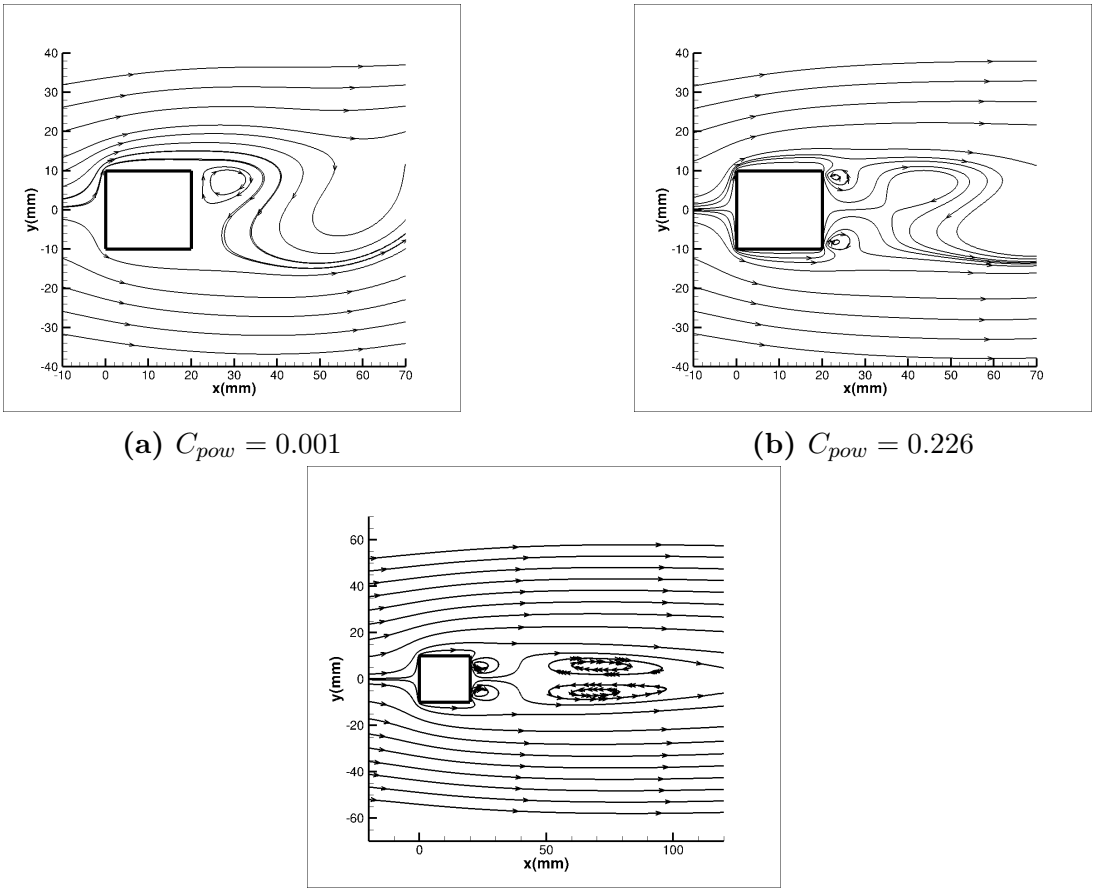

(a) $C_{pow} = 0.001$ **(b)** $C_{pow} = 0.226$

(c) $C_{pow} = 0.697$

Figure 4.29: Flow field for $Re = 100$ under different plasma power input, Case 3

However, computations at $Re = 200$ show that the oscillations in the flow field cannot be suppressed completely for higher Reynolds numbers. Figure 4.30 shows the lift fluctuation and the average drag vs power input at $Re = 200$. Initially, when the power input is small, the lift fluctuation is reduced by the plasma body force. However, when the power input reaches a certain level, the lift fluctuation starts to increase when more power is added. The average drag, on the other hand, always decreases with increasing of power input. The configuration with the two actuators farthest apart, i.e., the $y/h = \pm 0.8$ case, is still the most effective installation configuration.

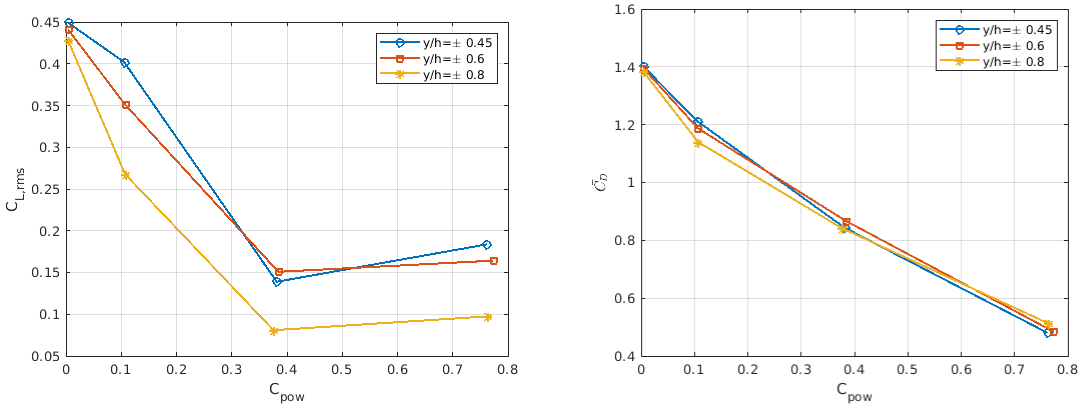

(a) Lift fluctuation **(b)** Average drag coefficient

Figure 4.30: Lift fluctuation and average drag vs C_{pow} for $Re = 200$ under different actuator arrangements, Case 3

Figure 4.31 shows the flow field for the $y/h = \pm 0.8$ case when the power input $C_{pow} = 0.77$. Even with this extreme amount of power input in the optimum actuator location, the flow field is still asymmetric and unsteady. The pair of new vortices generated by the plasma actuators pushes the main shedding vortices downstream and thus attenuates their influence on the lift fluctuations as shown in Figure 4.30(a). Nevertheless, they are unable to stabilize the main shedding vortices or the separation vortices on the top and bottom surfaces from the leading edges of the cylinder at this high Reynolds number.

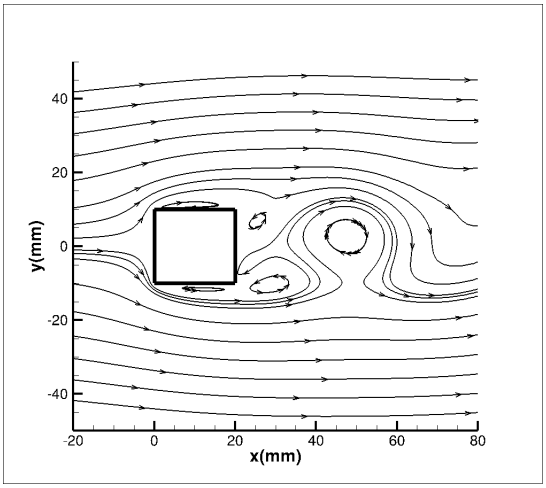

Figure 4.31: The flow field under plasma control at one instant when $C_{pow} = 0.77$, Case 3.

To measure the efficacy of the plasma actuator for drag reduction, a drag reduction efficacy coefficient is defined as $\eta = \frac{\bar{C}_{D,NC}}{\bar{C}_D + \bar{C}_{pow}}$, which is the ratio of drag coefficient without control divided by the combination of drag and power coefficients. Figure 4.32 shows η vs C_{pow} for the configuration with $y/h = \pm 0.8$. For both Reynolds numbers, the drag efficacy is always higher than 1.0, indicating that the plasma actuator is able to achieve a net power saving. We can also see that the efficacy for $Re = 100$ is higher than the efficacy for $Re = 200$, indicating that the plasma actuator is more energy efficient for lower Reynolds numbers. When $Re = 100$, the efficacy always increases with respect to plasma power input. When $Re = 200$, however, the maximum efficacy is achieved when the plasma power coefficient $C_{pow} = 0.4$. When the power input increases beyond this value, the efficacy is actually decreasing when more power is added.

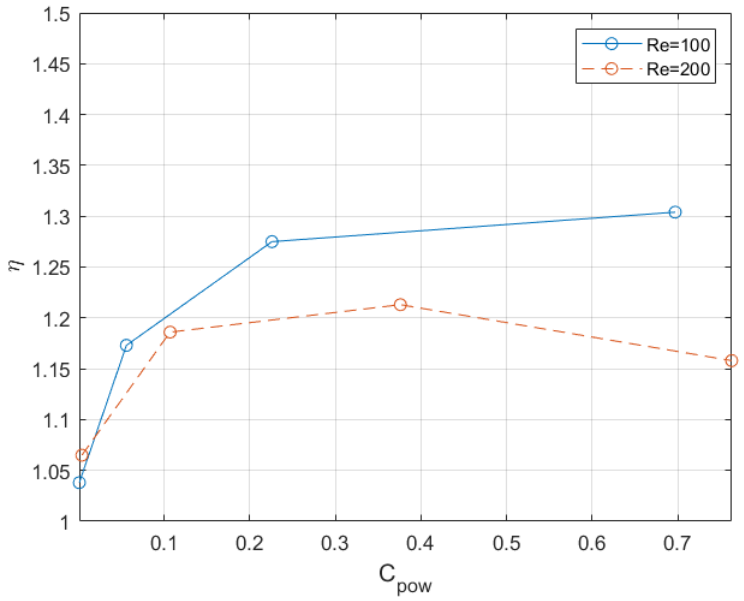

Figure 4.32: Drag reduction efficacy vs power input for Case 3.

Chapter 5

Plasma Induced Flow Field around a Circular Cylinder

Figure 5.1 shows a sketch of a pair of DBD plasma actuators installed on a circular cylinder in Hui et al.[27]'s experiment. In this experiment, two plasma actuators are installed symmetrically on both sides of the circular cylinder and the initial fluid is quiescent. In other words, there is no free stream in this project and the flow field is entirely induced by the plasma actuators. The plasma actuator on the left is referred to as the left actuator while the plasma actuator on the right is referred to as the right actuator. At the negative y-axis, the azimuth angle equals to $0°$. The clockwise direction is considered to be positive and the counter-clockwise direction is considered to be negative. To avoid potential asymmetry caused by gravity, the left actuator is located at an azimuth angle of $90°$ while the right actuator is located at an azimuth angle of $-90°$. The plasma actuators have the same geometry as those used in Chapter 4 and the simulation is created to resemble the settings in Hui et al.[27]'s experiment.

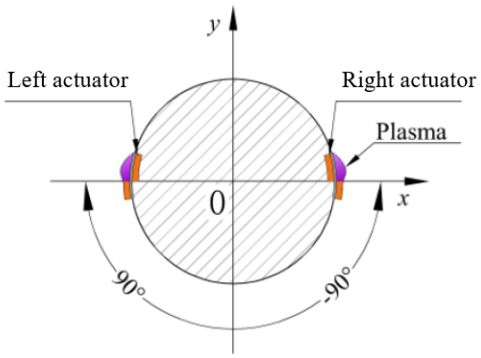

Figure 5.1: A sketch of plasma actuators installed on a circular cylinder.

Figure 5.2 shows the mesh around the circular cylinder, where the left side shows the entire mesh and the right side shows the blow-up region around the circular cylinder. The axis x/D and y/D are the coordinates in the x and y directions normalized by the cylinder diameter D. Finer grids are implemented in the near-wall area to capture the details of the boundary layer. There are 392 grids in the circumferential direction and 194 grids in the radial direction. Although no mesh sensitivity analysis has been done in this research, this mesh has been tested on several other cases and was proven to be fine enough. The flow field is simulated by solving the Unsteady Reynolds Averaged Navier-Stokes (URANS) Equations with the SA turbulence model. The boundary condition on the surface of the circular cylinder is the no-slip boundary condition while the boundary condition in the far field is the 1D non-reflecting boundary condition, which is implemented to break down the vortices accumulated near the outer boundary so that they do not interfere with the flow field inside the domain.

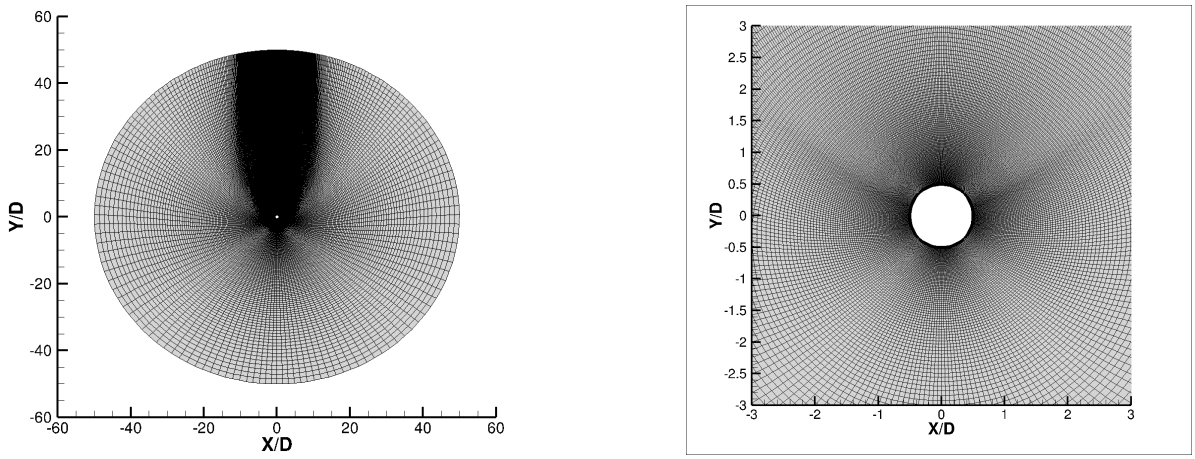

(a) The entire mesh **(b)** Zoom-in

Figure 5.2: The mesh around the circular cylinder

Both steady-state and duty-cycle actuation signals are studied in this project. Table 5.1 describes the three cases under steady-state actuation. In Case 1, the right actuator is always on while the left actuator is always off, corresponding to a duty-cycle ratio $\tau = 0.0$. In Case 2, the left actuator is always on while the right actuator is always off, corresponding to a duty-cycle ratio $\tau = 1.0$. In the third case, both actuators are always on and the plasma body forces are symmetric on both sides.

Case 1: $\tau = 0.0$	right-side actuation
Case 2: $\tau = 1.0$	left-side actuation
Case 3: Both-on	symmetric actuation

Table 5.1: Steady-state cases

Under duty-cycle actuation, the plasma body force is modulated by a square wave on-off switch. Table 5.2 describes the duty-cycle frequencies and the duty-cycle ratios under different plasma actuation signals. For lower frequencies $f = 1, 5, 10Hz$, five different duty-cycle ratios, $\tau = 0.01, 0.3, 0.5, 0.7, 0.99$, are simulated under each duty-cycle frequency. For higher frequencies $f = 40, 60, 100, 200Hz$, three different duty-cycle ratios, $\tau = 0.3, 0.5, 0.7,$

are simulated for each duty-cycle frequency. The highest duty-cycle frequency studied is $f = 200Hz$ because beyond this value, the flow field no longer changes.

f	τ
$1Hz$	0.01, 0.3, 0.5, 0.7, 0.99
$5Hz$	0.01, 0.3, 0.5, 0.7, 0.99
$10Hz$	0.01, 0.3, 0.5, 0.7, 0.99
$40Hz$	0.3, 0.5, 0.7
$60Hz$	0.3, 0.5, 0.7
$100Hz$	0.3, 0.5, 0.7
$200Hz$	0.3, 0.5, 0.7

Table 5.2: Duty-cycle frequencies and duty-cycle ratios for different cases

For steady-state cases, around $30,000$ iterations are required to get a fully converged solution. For unsteady actuation, the dual-time stepping method is used where each physical time step has 200 pseudo time steps. For duty-cycle ratios $\tau = 0.01, 0.99$, 500 physical time steps are used in one duty-cycle period. For duty-cycle ratios $\tau = 0.3, 0.5, 0.7$, 130 physical time steps are used in each duty-cycle period. This chapter will be broken into two parts. The first part studies the steady-state actuation while the second part studies the duty-cycle actuation. The contours shown in this chapter is taken in a rectangular measurement window sketched in Figure 5.3, where the length of the rectangle equals to 4 cylinder diameters and the height of the rectangle equals to 2 cylinder diameters. This measurement window is chosen to be the same as the experimental measurement window in Hui et al.[27]'s paper for validation purposes.

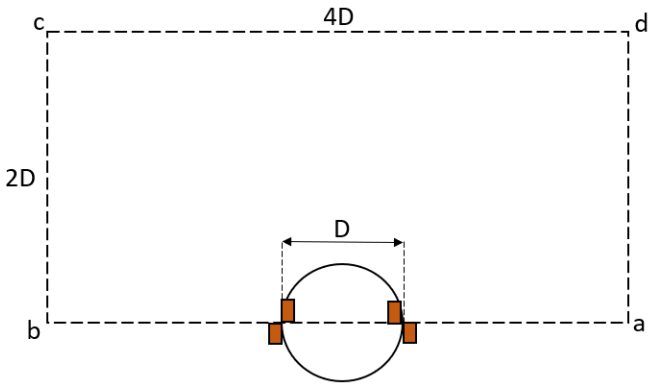

Figure 5.3: The measurement window

The total plasma body force in the x and y directions $f_{bx,tot}$, $f_{by,tot}$ are calculated by the following set of equations, where $f_{bx}(x,y)$ and $f_{by}(x,y)$ are the plasma body forces per unit mass in the x and y directions while ρ_{air} is the density of air.

$$f_{bx,tot} = \int\int\int_v \rho_{air} f_{bx}(x,y)dv \tag{5.1}$$

$$f_{by,tot} = \int\int\int_v \rho_{air} f_{by}(x,y)dv \tag{5.2}$$

Then the magnitude of the plasma body force in the measurement window $f_{b,tot}$ can be calculated as below.

$$f_{b,tot} = \sqrt{f_{bx,tot}^2 + f_{by,tot}^2} \tag{5.3}$$

In order to study the plasma control effects quantitatively, a series of reference variables are defined for the normalization process. The reference acceleration g_{ref} is calculated by Equation (5.4), where $f_{b,tot}$ refers to the total plasma body force induced by one plasma actuator and M_{tot} is the total mass of the fluid in the domain shown in Figure 5.3.

$$g_{ref} = \frac{f_{b,tot}}{M_{tot}} \tag{5.4}$$

Equation (5.5) calculates the reference velocity, which refers to the velocity induced by the

reference acceleration after traveling through the reference length L_{ref}, which equals to the diameter of the circular cylinder D.

$$V_{ref} = \sqrt{2g_{ref}L_{ref}} \tag{5.5}$$

Equation (5.6) calculates the reference time, which refers to the time required for a fluid element to travel across the reference length at the reference velocity.

$$\tau_{ref} = \frac{L_{ref}}{V_{ref}} \tag{5.6}$$

The momentum is calculated by the integration of the velocity field in the measurement window multiplied by the constant air density, as shown in Equation (5.7). The reference momentum T_{ref} is calculated by Equation (5.8), where M_{tot} is the total mass of the fluid inside the measurement window and V_{ref} is the reference velocity. Although the momentum is a vector, the reference momentum is a scalar.

$$T = \int\int\int_v \rho\vec{V}dv \tag{5.7}$$

$$T_{ref} = M_{tot}V_{ref} \tag{5.8}$$

5.1 Flow under steady-state actuation

In this section, the plasma control effect is studied under different steady-state actuation signals. Figure 5.4 shows the body force contours in the x and y directions in Case 1, where only the right actuator is turned on and the left actuator is always turned off. The body force only exists on the right side, where the force in the x-direction points to the left and the force in the y-direction points upwards.

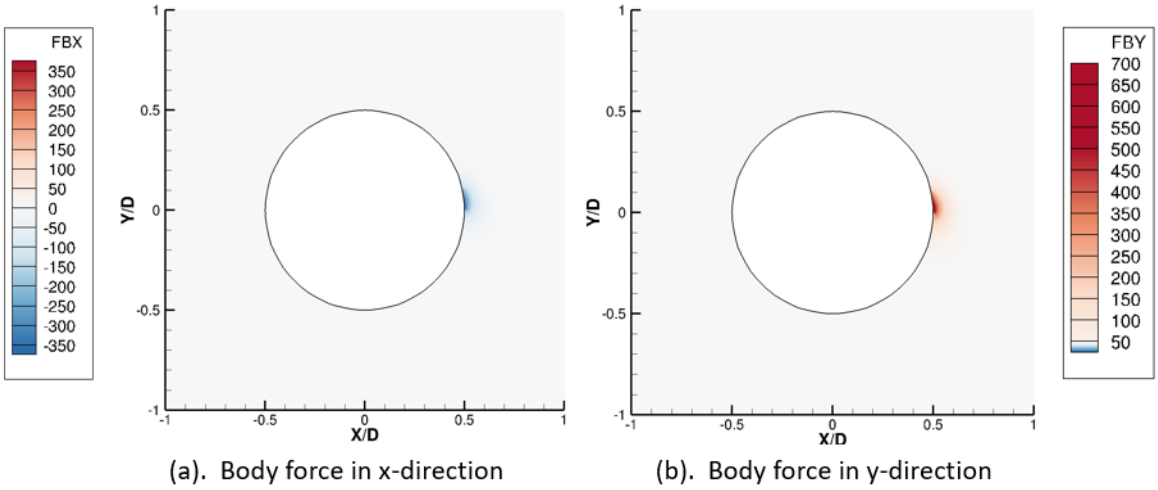

Figure 5.4: The plasma body force contour in Case 1: right-on

Figure 5.5(a) shows the simulated flow field, which is represented by the velocity vectors on top of the vorticity contour. $\frac{\omega D}{U_{max}}$ is the normalized vorticity, where ω is the vorticity, D is the diameter of the cylinder and U_{max} is the maximum velocity in the flow field. Coordinates x/D and y/D are the non-dimensional coordinates where both the x and y axis are divided by the cylinder diameter D. A wall jet is evidenced by the long velocity vectors sandwiched between a positive and a negative vortex sheet originating from the right actuator. This jet is induced by the body force in the y-direction and is able to cling to the cylinder surface due to the Conda effect, resulting in a left-running jet after flow separation on top of the

circular cylinder. Figure 5.5(b) shows the experimental flow field under the same actuation signal. The simulation results show good agreement with the experimental results despite some small differences. The most obvious difference is that the simulated results show more focused vortex sheets surrounding the jet immediately downstream of the actuator rather than some distance away from the actuator as shown in the experiment. There are two reasons for this difference. First, although Figure 5.5(a) and Figure 5.5(b) plot the velocity vectors on the same window, the simulation results are plotted on a fine curvilinear grid confirming to the surface of the cylinder while the PIV measurement for experimental results are much coarser. The second reason is the inaccuracy of the body force model. The current body force model generates a body force right at the center of the actuator while the actual plasma actuator may experience some lag in distance. Despite these differences, the simulated results can be considered as reasonably good.

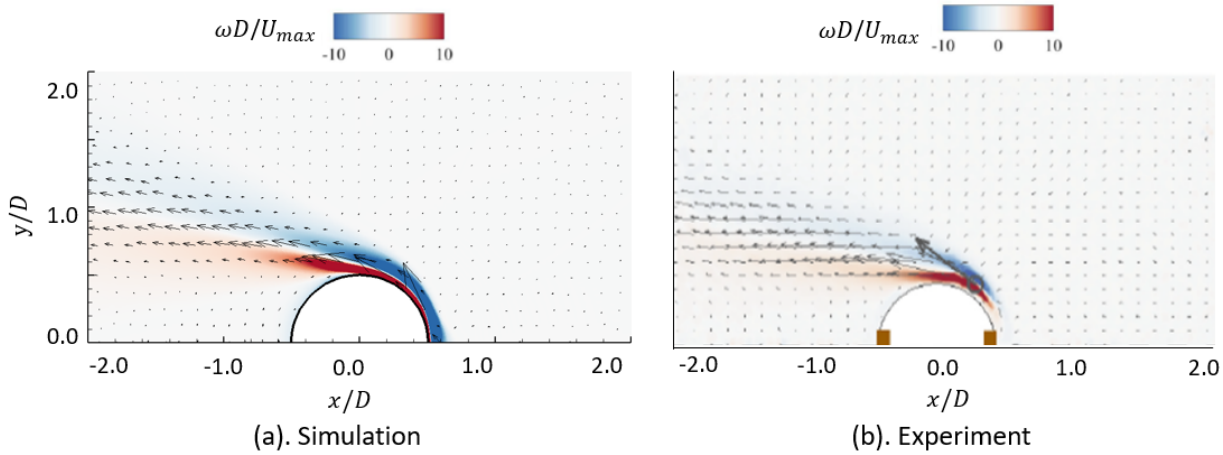

Figure 5.5: Velocity vectors over vorticity contour for right- on case

Figure 5.6 shows the streamlines, plasma body force, pressure and friction force around the circular cylinder. The plasma body force only exists on the right side of the circular cylinder and is approximately zero everywhere else. The pressure and friction coefficients are calculated by Equations (5.9) and (5.10). For both forces, a peak appears on the right side of the cylinder due to the plasma body force injecting mechanical energy into the flow

field. Further downstream, the effect of the plasma body force starts to fade away, and both the pressure and velocity start to decrease. One interesting fact is that the pressure decreases much faster than the velocity because the pressure energy transforms into kinetic energy as the jet travels downstream.

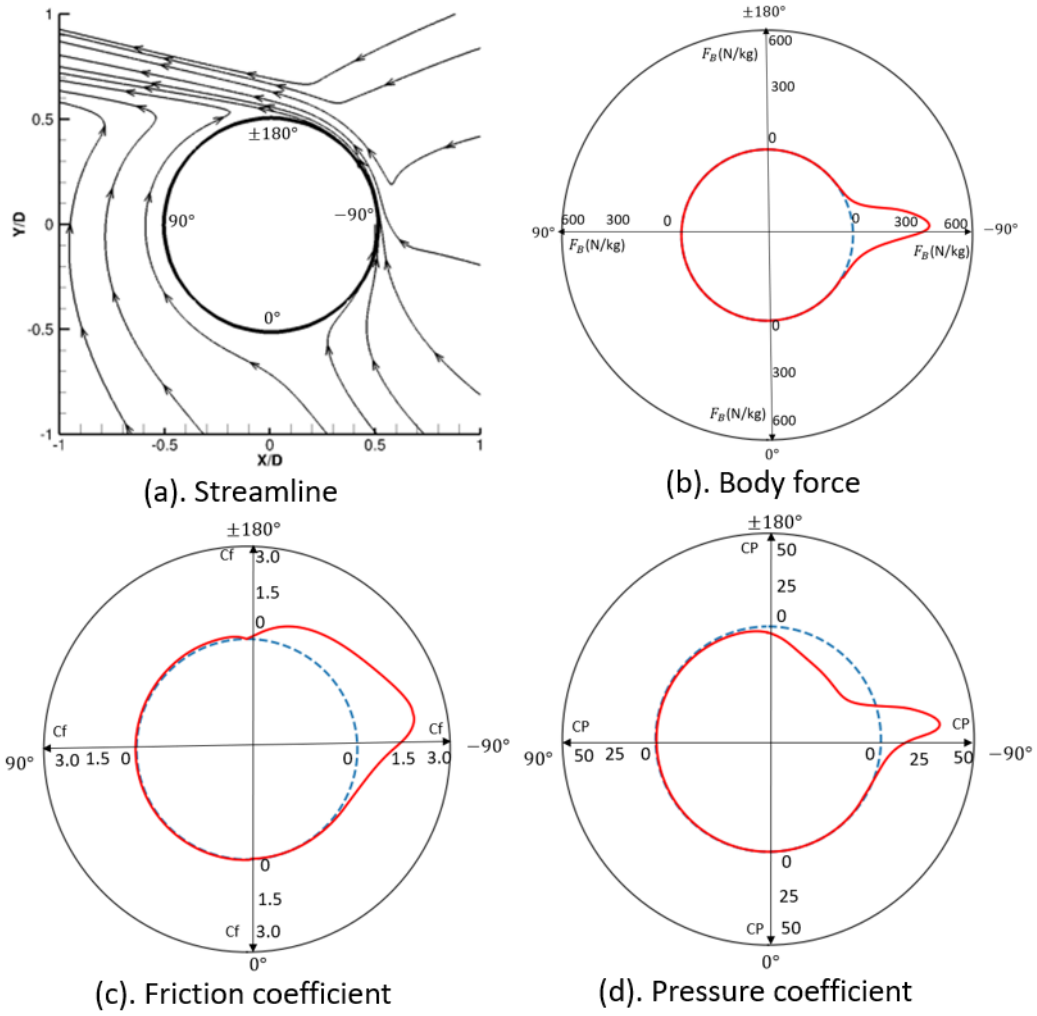

Figure 5.6: Streamlines and surface parameters for the right-on case

$$C_P = \frac{P - P_\infty}{\frac{1}{2}\rho V_{ref}^2} \tag{5.9}$$

$$C_f = \frac{\tau_w}{\frac{1}{2}\rho V_{ref}^2} \tag{5.10}$$

In Equation (5.10), τ_w refers to the shear stress on the cylinder surface defined by the following equation.

$$\tau_w = \mu \frac{\partial u_\theta}{\partial r}|_s \tag{5.11}$$

Table 5.3 shows the force and momentum coefficients in the x and y directions. The pressure and friction force coefficients equal to the force divided by the plasma body force induced by the left actuator, as can be seen in the following two equations. In Equation (5.13), the wall shear stress τ_w is calculated by Equation (5.11).

$$CF_p = \frac{\int\int_A p dA}{f_{b,tot}} \tag{5.12}$$

$$CF_f = \frac{\int\int_A \tau_w dA}{f_{b,tot}} \tag{5.13}$$

The momentum coefficient C_M equals to the momentum in the measurement window divided by the reference momentum, as can be seen in the equation below.

$$CM = \frac{T}{T_{ref}} \tag{5.14}$$

CF_p and CF_f equal to the pressure and friction forces divided by the plasma body force generated by the left actuator. One interesting fact is that the pressure force in the x-direction is almost negligible comparing to the pressure force in the y-direction. The reason for this can be found in Figure 5.6(d), where the high pressure region on the right side of the cylinder is able to induce a pressure force pointing to the left and the low pressure region on the upper right side of the cylinder is able to induce a pressure force pointing to the upper right direction. As a result, the pressure force in the x-direction is cancelled out due to the effect of the high and low pressure region. The pressure force in the y-direction points upwards due to the effect of the low pressure region on the top half cylinder. The negative friction force in the x-direction is caused by the left-running jet on top of the circular cylinder

while the positive friction force in the y-direction is caused by the upwards wall jet on the right side. The magnitude of the total pressure force is much bigger than the magnitude of the total friction force, indicating that the pressure force has the dominant effect. The momentum coefficient in the x-direction is negative due to the left-running wall jet after the separation point. The momentum coefficient in the y-direction is positive due to the upwards wall jet on the right. We notice that the magnitude of the momentum in the x-direction is much bigger than that of the y-direction. The reason can be found in Figure 5.5, where the left-running jet in the x-direction is much wider than the upward-running jet in the y-direction. The wider jet in the x-direction is able to induce a higher momentum.

	x-direction	y-direction	Magnitude
CF_p	-0.0018	0.4668	0.4668
CF_f	-0.0340	0.0812	0.088
C_M	-0.611	0.084	0.612

Table 5.3: The force and momentum in the x and y directions for right-on case

Figure 5.7 shows the body force contours for the left-on case. In this case, the plasma body force only exists on the left side with the plasma in the x-direction pointing to the right and the plasma in the y-direction pointing upwards.

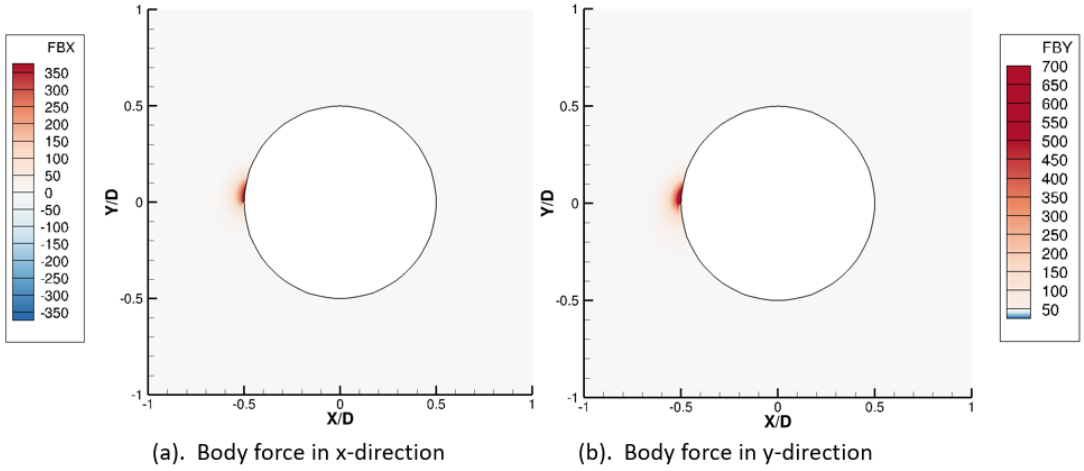

Figure 5.7: The plasma body force contour in Case 2: left-on

Figure 5.8(a) shows the simulated flow field for the left-on case, which is the mirror image of the right-on case. Although the simulated result still agrees well with the experimental result overall, the discrepancy seems to be slightly larger because there is slight asymmetry between the left-on and right-on case in the experiment, which is caused by slight asymmetry in the installation of the plasma actuators during the experiment. The computational simulation does not suffer from such a problem and thus able to produce exact symmetric results.

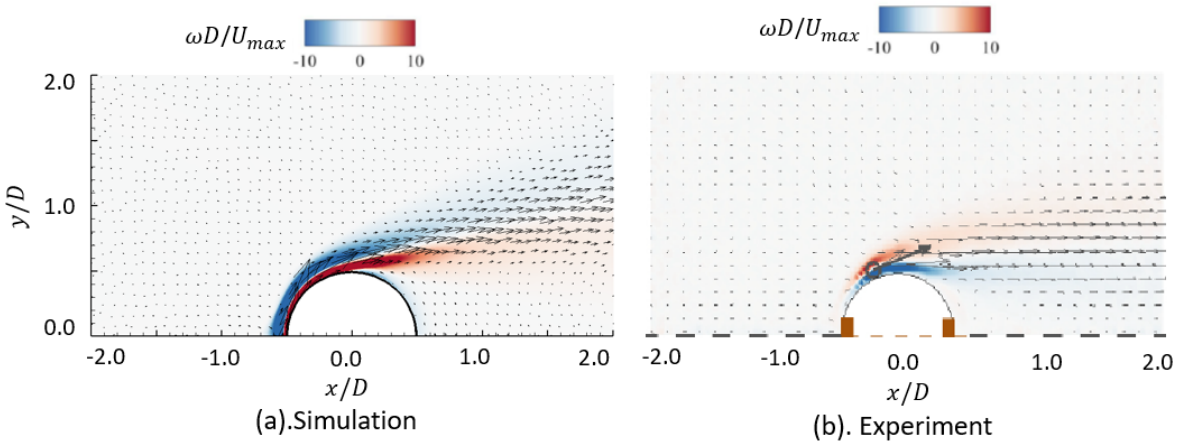

Figure 5.8: Velocity vectors over the vorticity contour for left-on case

Figure 5.9(a) shows the streamline, plasma body force, friction and pressure distribution

around the circular cylinder, all of which are the mirror image of the right-on case. The complete symmetry of both cases are shown in the simulation.

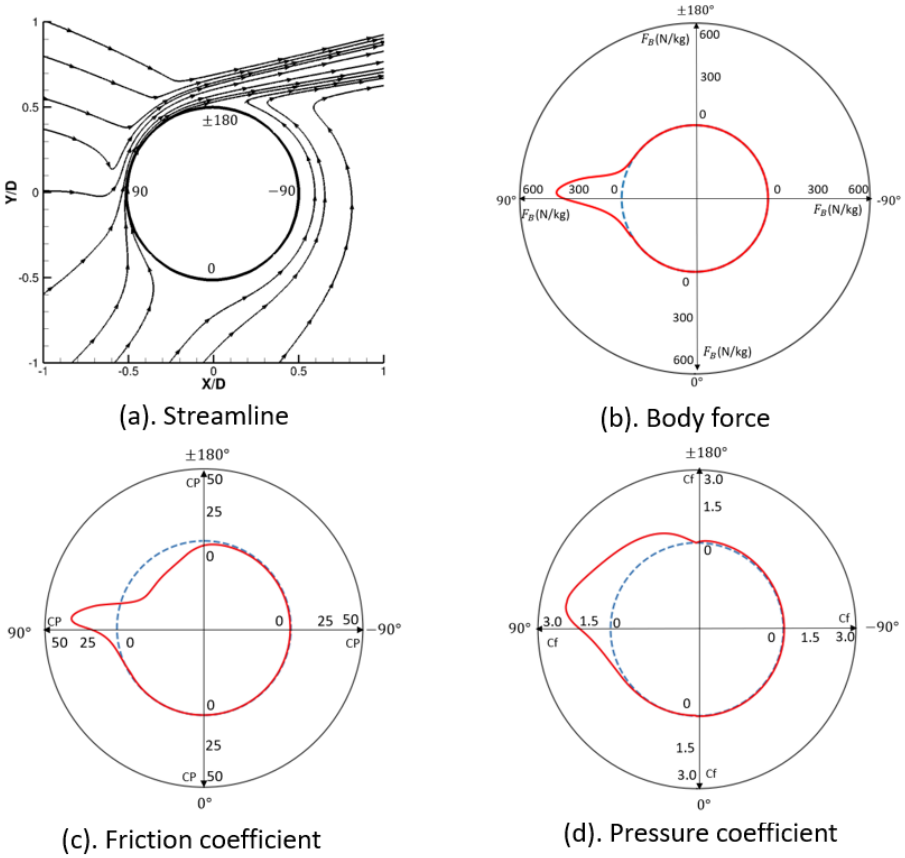

Figure 5.9: Streamline and surface parameters for the left-on case

	x-direction	y-direction	total
CF_p	0.0018	0.4668	0.4668
CF_f	0.0340	0.0812	0.088
C_M	0.611	0.084	0.612

Table 5.4: The force and momentum in the x and y directions for the left-on case

Figure 5.10 shows the body force contours for the Both-on case, where the plasma actuators on both sides are activated. In this case, symmetric plasma body force exists on both sides with the body force on the left pointing to the positive x-direction and the body force on the right pointing to the negative x-direction. The body force in the y-direction are positive on both sides.

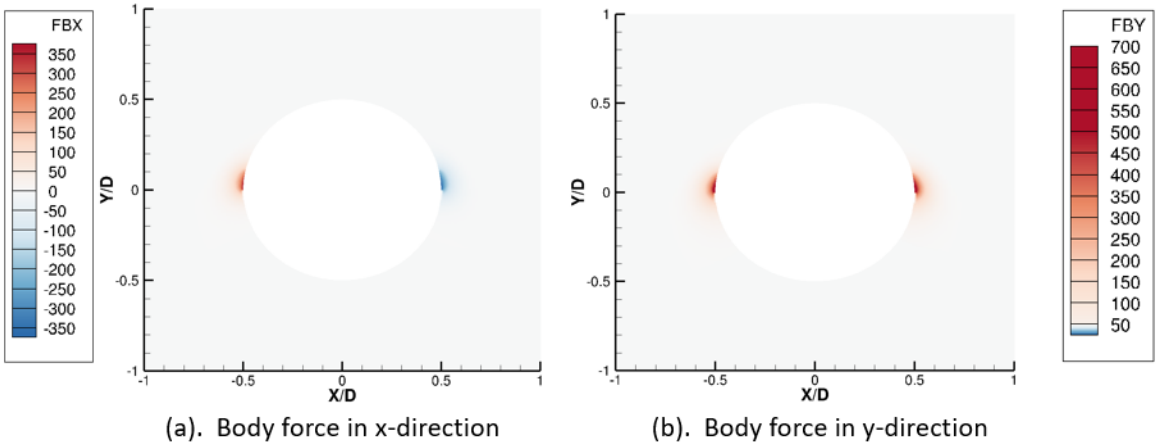

Figure 5.10: The plasma body force contour in Case 3: Symmetry

Figure 5.11(a) shows the plasma induced flow field in the Both-on case, where one steady jet is generated on each side of the cylinder. Initially, both jets cling to the cylinder surface due to the Conda effect. After some distance, the two jets start to separate from the wall until colliding at a point above the cylinder. The merged jet is much wider than the two jets on either sides of the cylinder and becomes weaker as it travels upwards. In this case, the simulated flow field once again shows relatively good agreement with the experimental flow field.

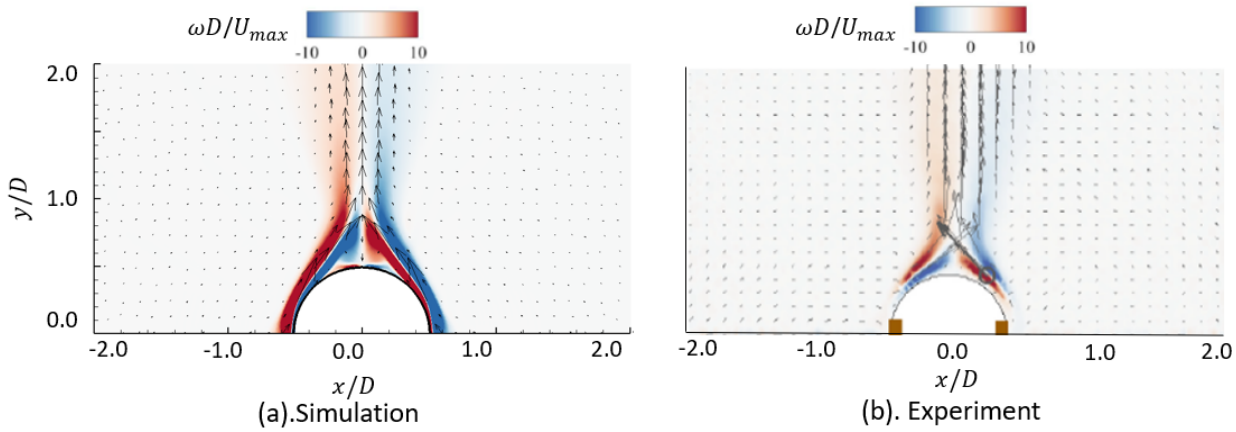

Figure 5.11: Velocity vectors over vorticity contour for the Both-on case

According to Figure 5.12, the plasma body force shows two symmetric peaks on both sides of the cylinder, inducing one jet on each side of the cylinder. Both jets travel upwards along the cylinder surface until separating near the cylinder top, where two vortices are generated due to flow separation. The friction coefficient is mostly positive except for a small region on top, where the two vortices are able to induce a negative jet resulting in a negative friction coefficient. The pressure distribution is symmetric with a peak and a valley on each side of the circular cylinder. On each side of the cylinder, the pressure distribution behaves similarly to the previous two cases except for a small peak appearing on top of the cylinder, which is caused by the collision of two wall jets.

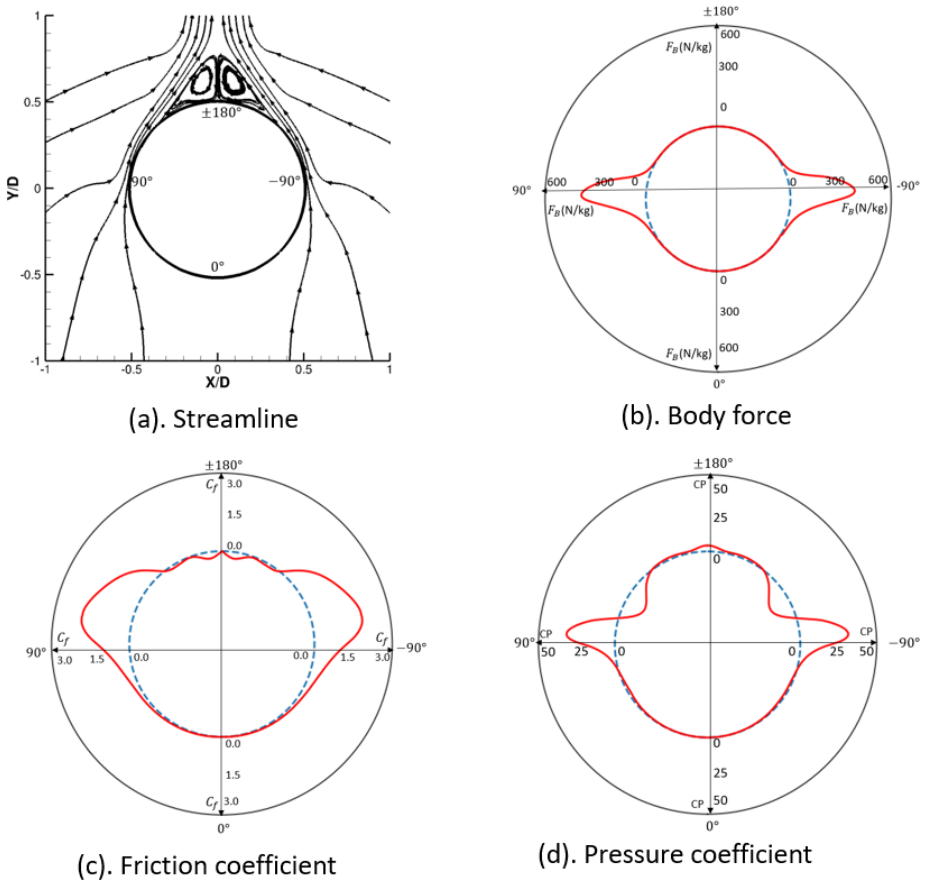

Figure 5.12: Streamline and surface parameters for the Both-on case

Table 5.5 shows the force and momentum coefficients in the x and y directions. The forces and momentum in the x-direction are negligible comparing to those of the y-direction, which is the result of the symmetric wall jet. The pressure and friction forces in the x-direction cancel each other out on the left and right sides of the circular cylinder. Surprisingly, the friction force becomes the dominant force in this case although the magnitude of the pressure coefficient is much larger. This is because the pressure force induced by the pressure peak and pressure valley cancel each other out along the cylinder surface. Since the friction coefficient is always positive, the friction force does not experience the same effect.

	x-direction	y-direction
CF_p	-0.0011	0.0634
CF_f	-0.0004	0.1297
CM	0.002	0.630

Table 5.5: The force coefficients in the x and y directions

The three cases above demonstrated the fidelity of the simulation as well as the relationship between the plasma body force and the flow field.

5.2 Flow under duty-cycle actuation

This section is divided into two parts, the first part shows the time-averaged flow fields and the second part shows the instantaneous flow fields throughout one duty-cycle period. Some of the velocity contours are compared with the experimental results for validation.

5.2.1 Time-averaged flow field under duty-cycle actuation

Figure 5.13 shows the variation of the plasma body force within one duty-cycle period, where T is the length of the duty-cycle period and τ is the duty-cycle ratio. When $0 < t < \tau T$, the left actuator is turned on and the right actuator is turned off, creating a body force on the left side. When $\tau T < t < T$, the left actuator switched to the right actuator, creating a body force on the right side.

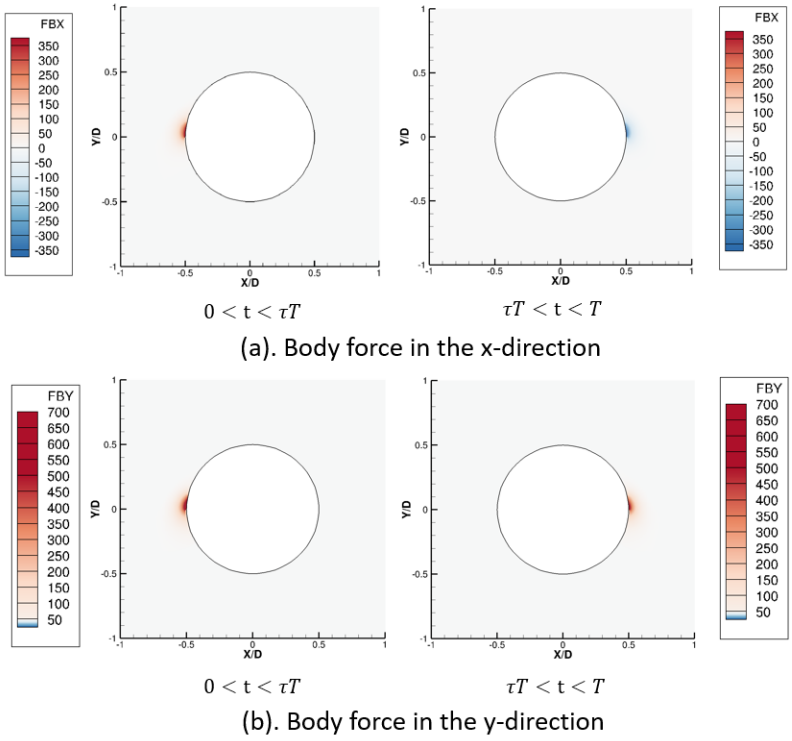

Figure 5.13: Plasma body force in one duty-cycle period.

The following results show the time-averaged body force contours and velocity fields under different duty-cycle ratios, ranging from $\tau = 0.01 - 0.99$. Obviously, the time-averaged body force is the same regardless of duty-cycle frequency and is only dependent on the duty-cycle ratio. Figure 5.14 shows the time-averaged body force field when $\tau = 0.01$. In this case, the left actuator is activated for only 1% of the time while the right actuator is activated for 99% of the time. As a result, the time-averaged body force on the left is almost negligible comparing to the time-averaged body force on the right.

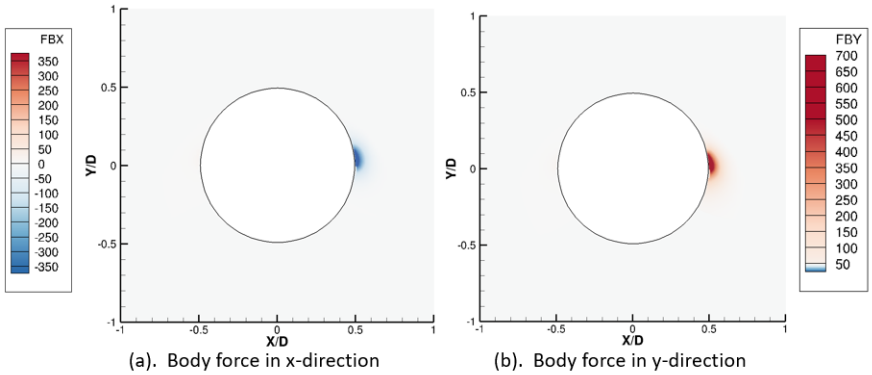

Figure 5.14: Time-averaged plasma body force contours for $\tau = 0.01$

Figure 5.15 shows the time-averaged flow fields under different frequencies when duty-cycle ratio $\tau = 0.01$. The time-averaged values are calculated from 1000 readings over 2 duty-cycle periods. At this duty-cycle ratio, the left actuator is too weak to induce any significant disturbance and the flow field is very similar to the steady-state right-on case. The red and blue contours of the vorticity on either side of the jet indicate the high opposite sign vorticity regions induced by the plasma body force. Regardless of frequency, this jet starts from the right-side, clinging to the surface of the cylinder as it travels upwards before separating from the wall. After the separation point, the jet travels almost horizontally to the left, getting wider as it travels downstream and the high-vorticity region slowly decays. The flow field does not show any significant difference under different duty-cycle frequencies except for one fact that the angle between the jet and the horizontal line is slightly bigger for lower

frequencies.

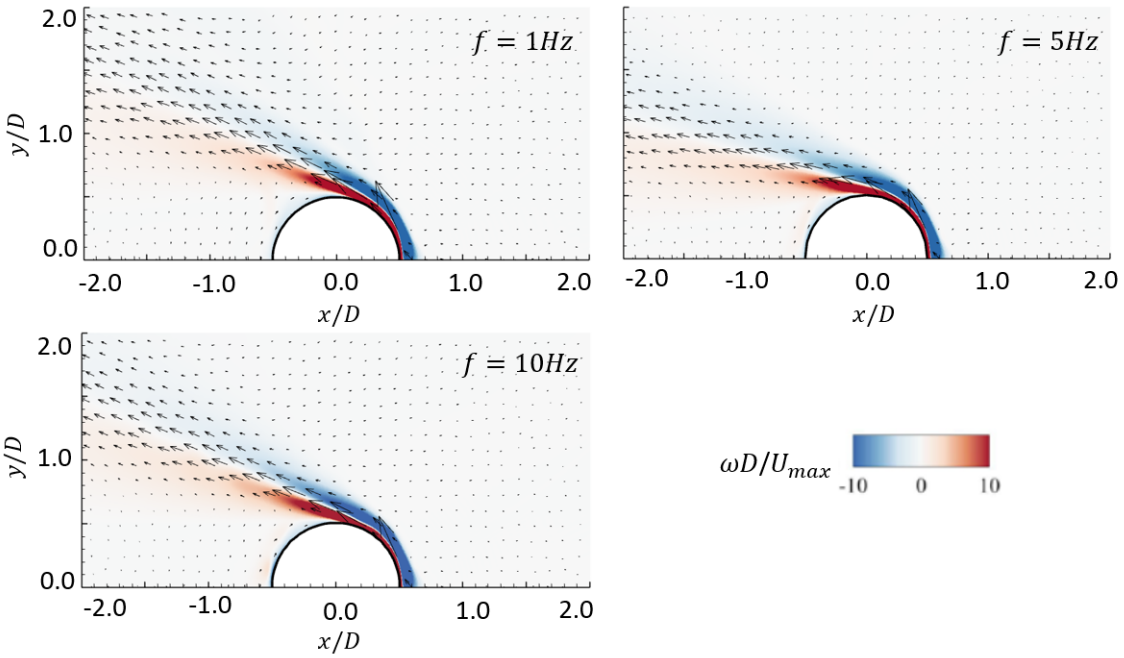

Figure 5.15: Time-averaged velocity vectors over vorticity contours for $\tau = 0.01$ at different frequencies

Figure 5.16 shows the time-averaged body force field when $\tau = 0.3$. In this case, the left actuator is activated for 30% of the time while the right actuator is activated for 70% of the time. Although the time-averaged body force on the left side is much stronger comparing to the previous case, it is still weaker than the body force on the right side. The stronger time-averaged body force on the right is able to induce stronger velocity and pressure on the right side, as can be seen in Figure 5.17(a).

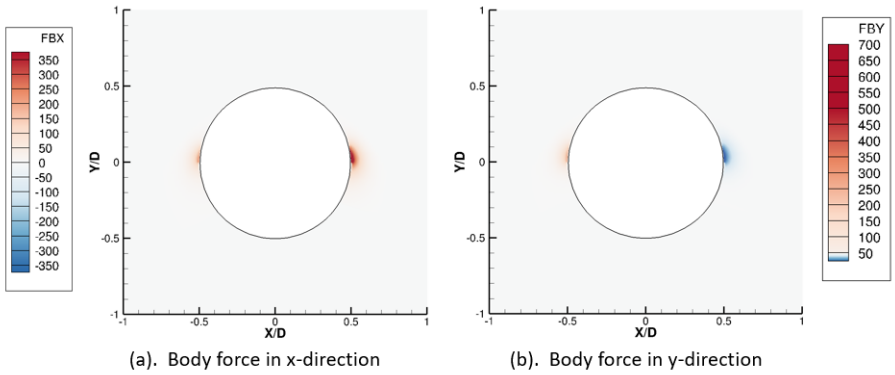

Figure 5.16: Time-averaged plasma body force contours for $\tau = 0.3$ at different frequencies

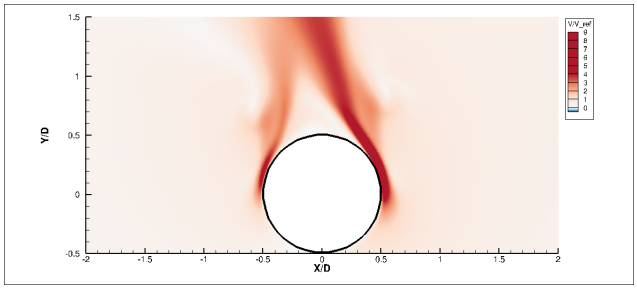

(a) Normalized velocity

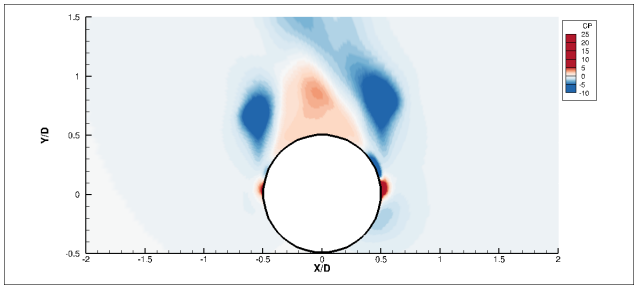

(b) Pressure coefficient

Figure 5.17: The pressure and velocity distribution for $f = 5Hz, \tau = 0.3$

Figure 5.18 shows the time-averaged flow field under different frequencies when $\tau = 0.3$. In this figure, two jets are generated on each side of the cylinder due to the plasma body force on both sides. Initially, two jets are able to cling to the surface due to the Conda effect. As the flow travels downstream, the curvature of the circular cylinder gets bigger and the jets start to separate from the wall. These two jets will eventually collide above the cylinder, generating a combined jet moving in the upper left direction due to the stronger wall jet on the right. Similar to the previous case, the combined jet slowly dissipates as it travels downstream. As the duty-cycle frequency increases, the wall jet hugs closer to the cylinder surface and the combined jet becomes thinner. The reason for this will be explained in details in the next subsection with the help of time-accurate contours. The time-averaged contours for $f = 100Hz$ and $f = 200Hz$ are the same, indicating the duty-cycle frequency can no longer affect the flow field beyond this point.

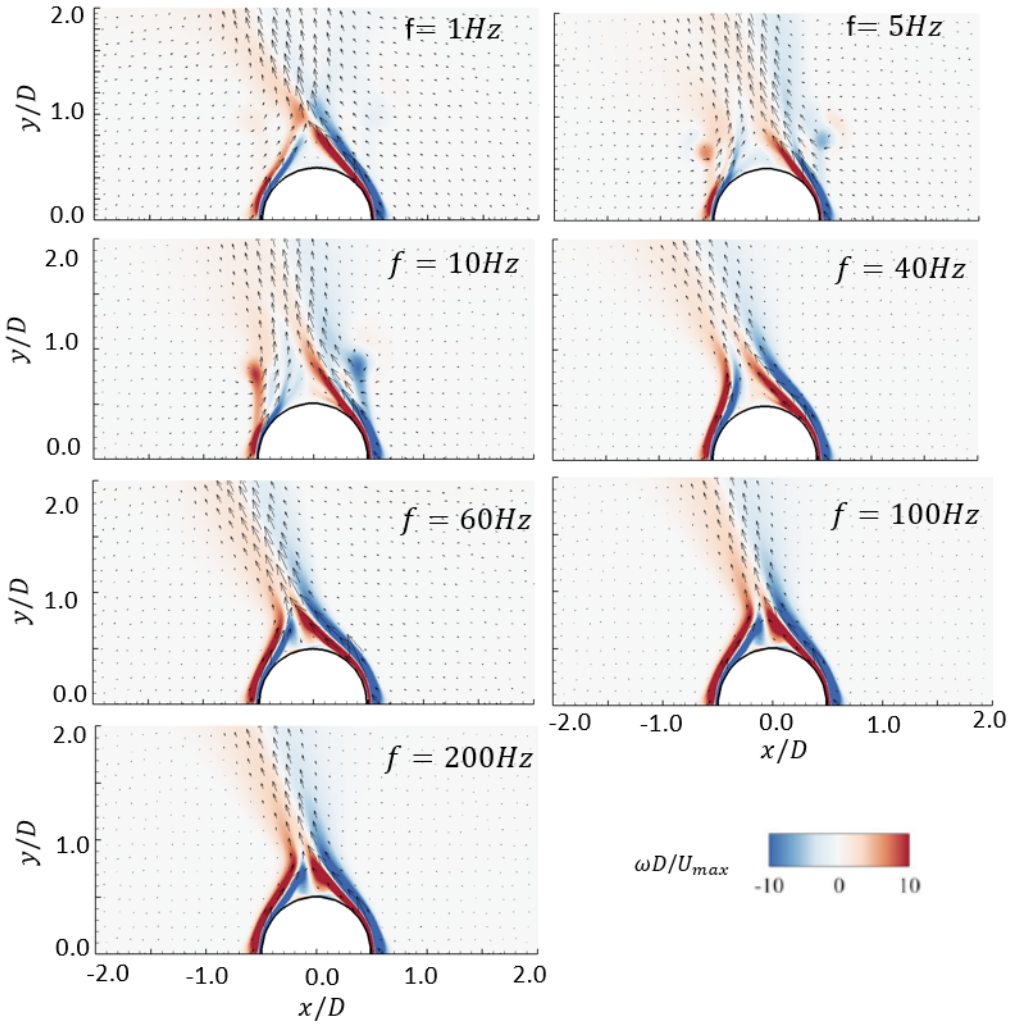

Figure 5.18: Time-averaged velocity vectors over vorticity contours for $\tau = 0.3$ at different frequencies

Figure 5.19 shows the streamlines when the duty-cycle ratio $\tau = 0.3$. The streamlines look similar for different frequencies, originating from below the circular cylinder, traveling along the cylinder surface before flow separation occurs on top. Then one or two vortices are formed on top of the circular cylinder due to flow separation. The combined jets above the cylinder surface travels in the upper left direction. Under very low duty-cycle frequencies such as $f = 1Hz$, no coherant vortex is formed on top of the cylinder. When the frequency increases to $f = 5Hz$, one small vortex appears on the top left region. When the frequency increases further to $f = 10Hz$, an additional vortex is generated on the top right region.

When the duty-cycle frequency increases even further, there are always two vortices on top of the cylinder with the vortices under higher frequencies being smaller. Since the strength of the wall jets are similar under low and high frequencies, the reason why vortices do not exist when $f = 1Hz$ is probably because when the frequency is too low, the duty-cycle period is very long and the vortex generated initially by the flow separation breaks down after some time.

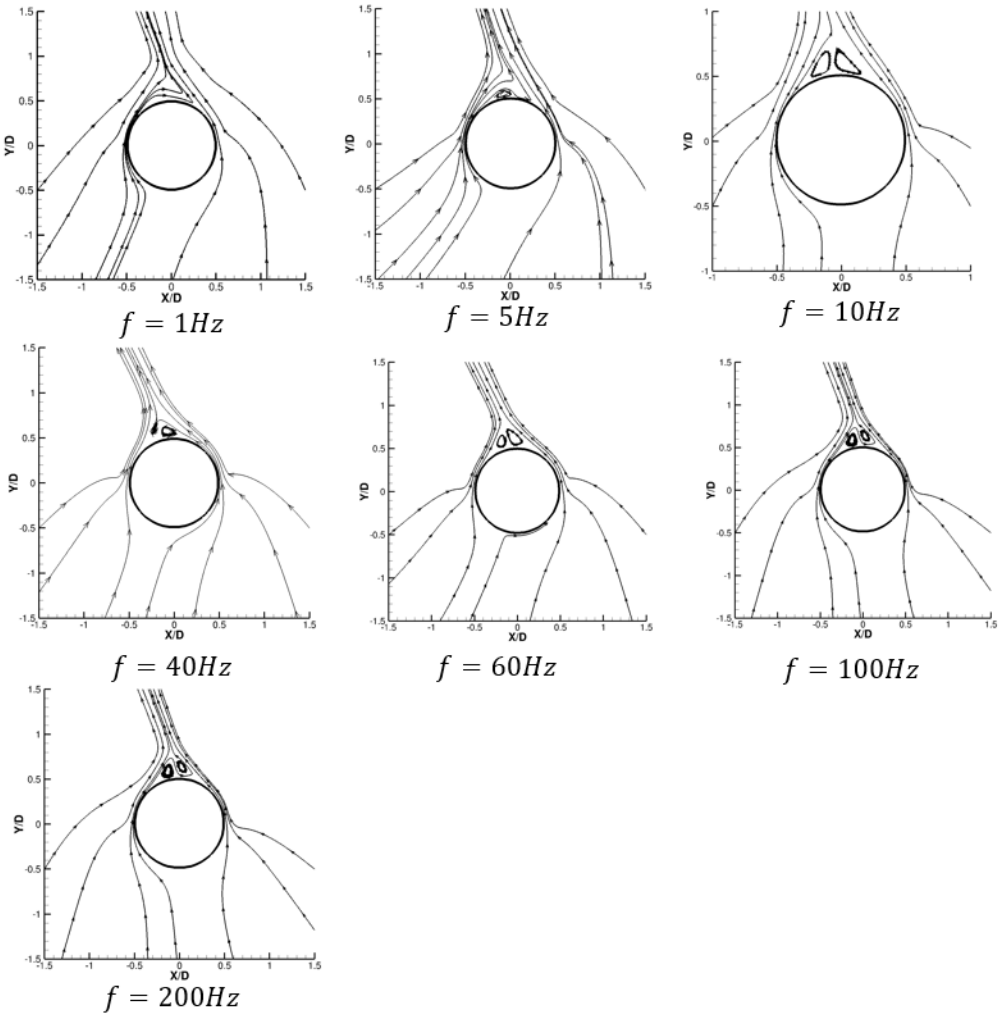

Figure 5.19: Time-averaged streamlines for $\tau = 0.3$

Figure 5.20 shows several different time-averaged parameters when the duty-cycle ratio $\tau = 0.3$ under different duty-cycle frequencies. Figure 5.20(a) shows the time-averaged plasma

body force along the cylinder. As expected, the right peak is higher than the left peak due to longer plasma activation time on the right side. The stronger body force on the right is able to induce stronger friction and pressure peak, as evidenced in Figures 5.20(b) and 5.20(c). Obviously, the magnitude of the friction coefficient is much smaller than the magnitude of the pressure coefficient, indicating that the pressure effect is the dominant effect in this case. The pressure and friction distribution along the cylinder does not show significant variance at different duty-cycle frequencies, indicating that the flow field near the cylinder wall is highly dependent on the duty-cycle ratio, but not the duty-cycle frequency.

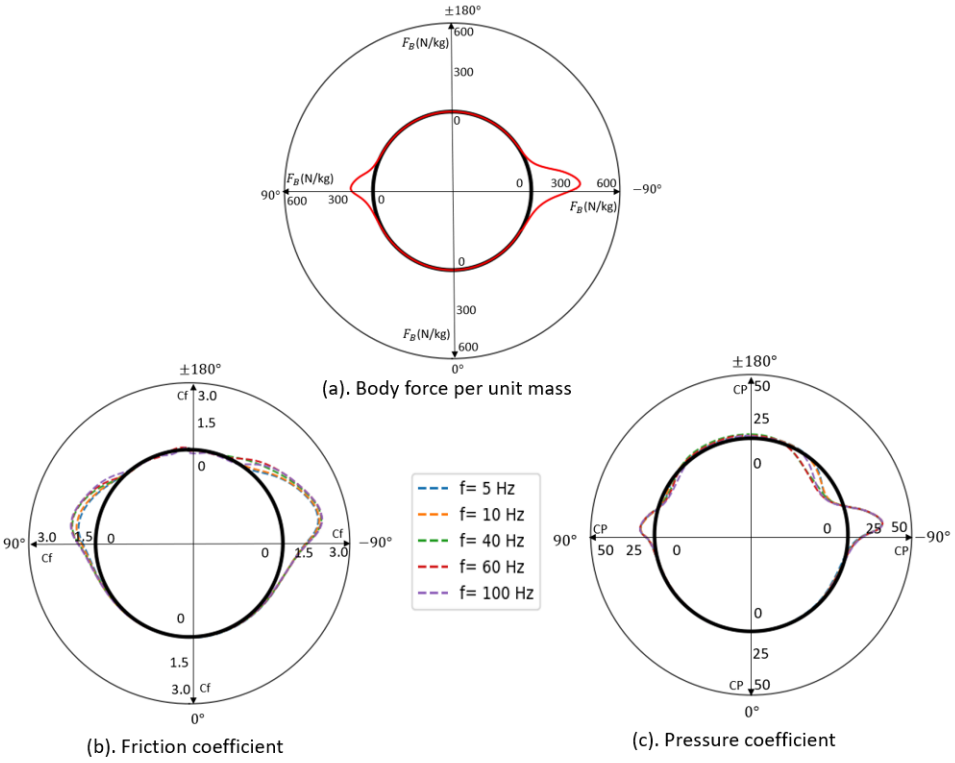

Figure 5.20: Parameters along the cylinder surface for $\tau = 0.3$ at different frequencies

Figure 5.21 shows the time-averaged momentum and maximum velocity when $\tau = 0.3$. The time-averaged momentum and maximum velocity does not show much variation with respect to the duty-cycle frequency. Because the combined jet above the cylinder travels in the upper left direction, the momentum in the x-direction is always negative while the momentum in

the y-direction is always positive. The maximum time-averaged velocity increases with respect to duty-cycle frequency. This is because under higher frequency, the previous vortex does not have enough time to travel downstream when the new vortex is generated. In the vicinity of the plasma actuator, the velocity increase induced by the previous vortex still exists when the next vortex is generated. As a result, the velocity equals to the combination of the velocity induced by the plasma body force and the velocity induced by the previous vortex. Surprisingly, although the simulated maximum velocity is bigger, the simulated time-averaged momentum is smaller than the experimental values. The reason for the smaller momentum in the simulation is the shorter combined jet above the circular cylinder, as evidenced in Figure 5.22. The shorter combined jet is caused by the vortices dissipating faster as they travel downstream in the simulation, the details of which will be explained in the next section.

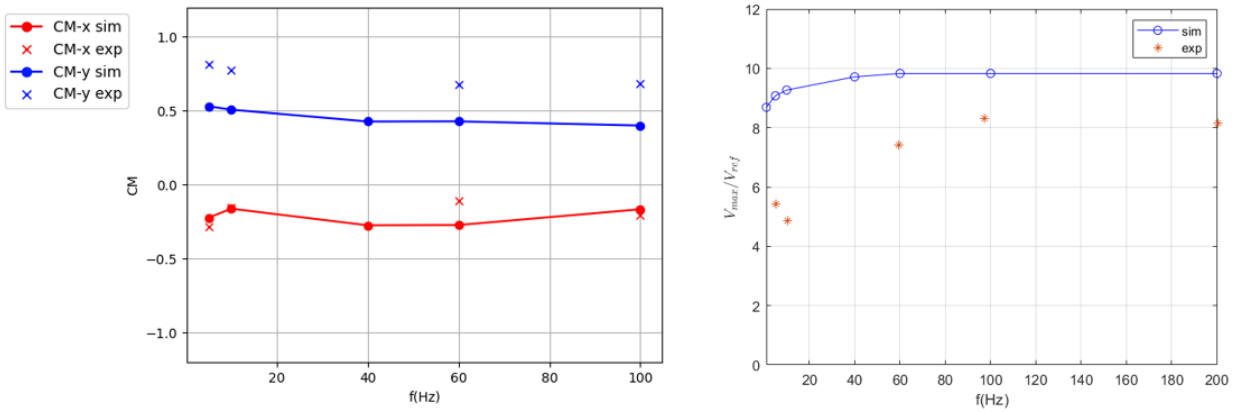

(a). Momentum (b). Maximum velocity

Figure 5.21: Time-averaged momentum and maximum velocity when $\tau = 0.3$

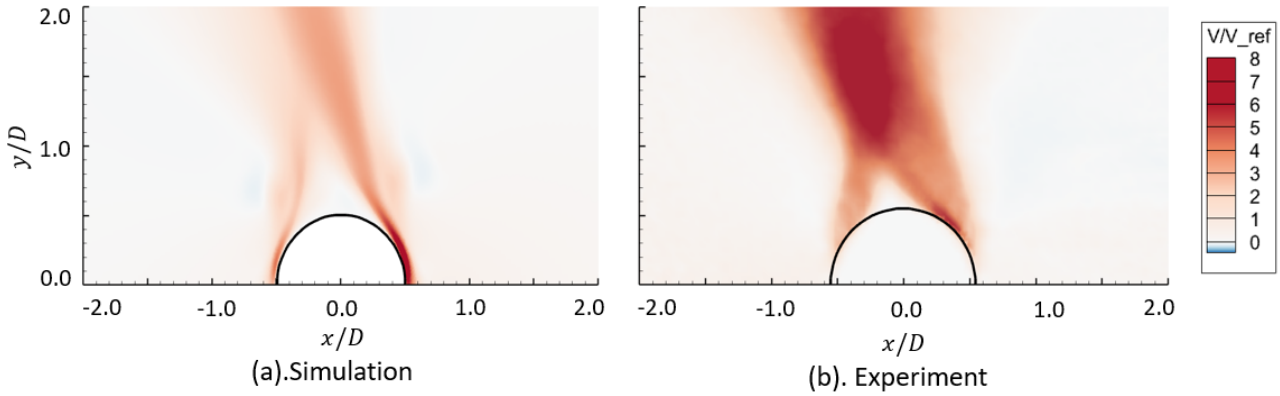

Figure 5.22: Comparison between the simulation and experimental time-averaged velocity contours for $f = 5Hz, \tau = 0.3$.

Figure 5.23 shows the time-averaged body force contour when the duty-cycle ratio $\tau = 0.5$. In this case, the left actuator is activated for the first 50% of the duty-cycle period while the right actuator is activated for the second 50% of the duty-cycle period. As a result, the time-averaged body force has equal strength on both sides. Figure 5.24 shows the velocity and pressure contour when $f = 5Hz$, $\tau = 0.5$. In this case, the velocity on both sides of the circular cylinder are equal to each other due to the equal time-averaged body force strength on both sides.

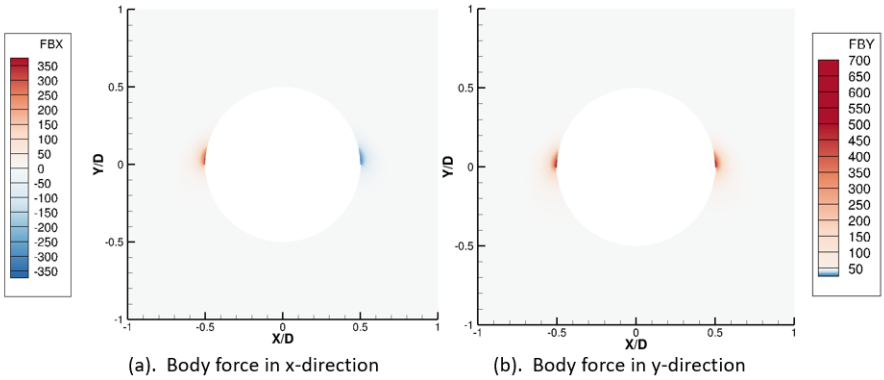

Figure 5.23: Time-averaged plasma body force contours for $\tau = 0.5$ at different frequencies

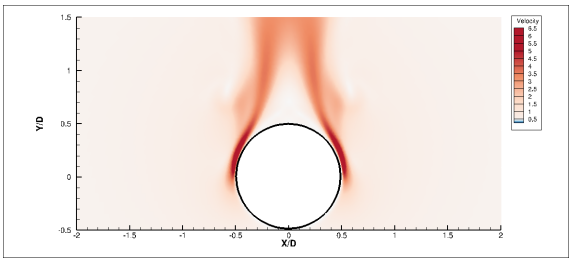

(a) Normalized velocity

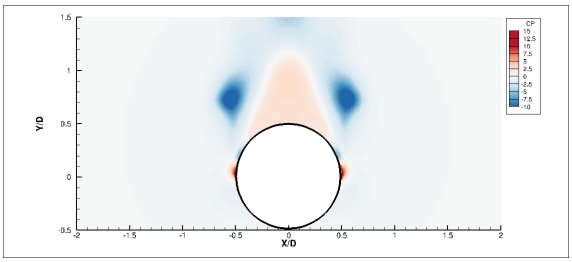

(b) Pressure coefficient

Figure 5.24: The time-averaged pressure and velocity distribution when $f = 5Hz$, $\tau = 0.5$

Figures 5.25 and 5.26 show the time-averaged flow fields and streamlines for $\tau = 0.5$ under different duty-cycle frequencies. Similar to the previous results, the two wall jets on both sides of the cylinder combine into a wider jet above the cylinder, which slowly dissipates as it travels upwards. Under this duty-cycle ratio, the flow field is symmetric due to the equal time-averaged plasma body force on both sides.

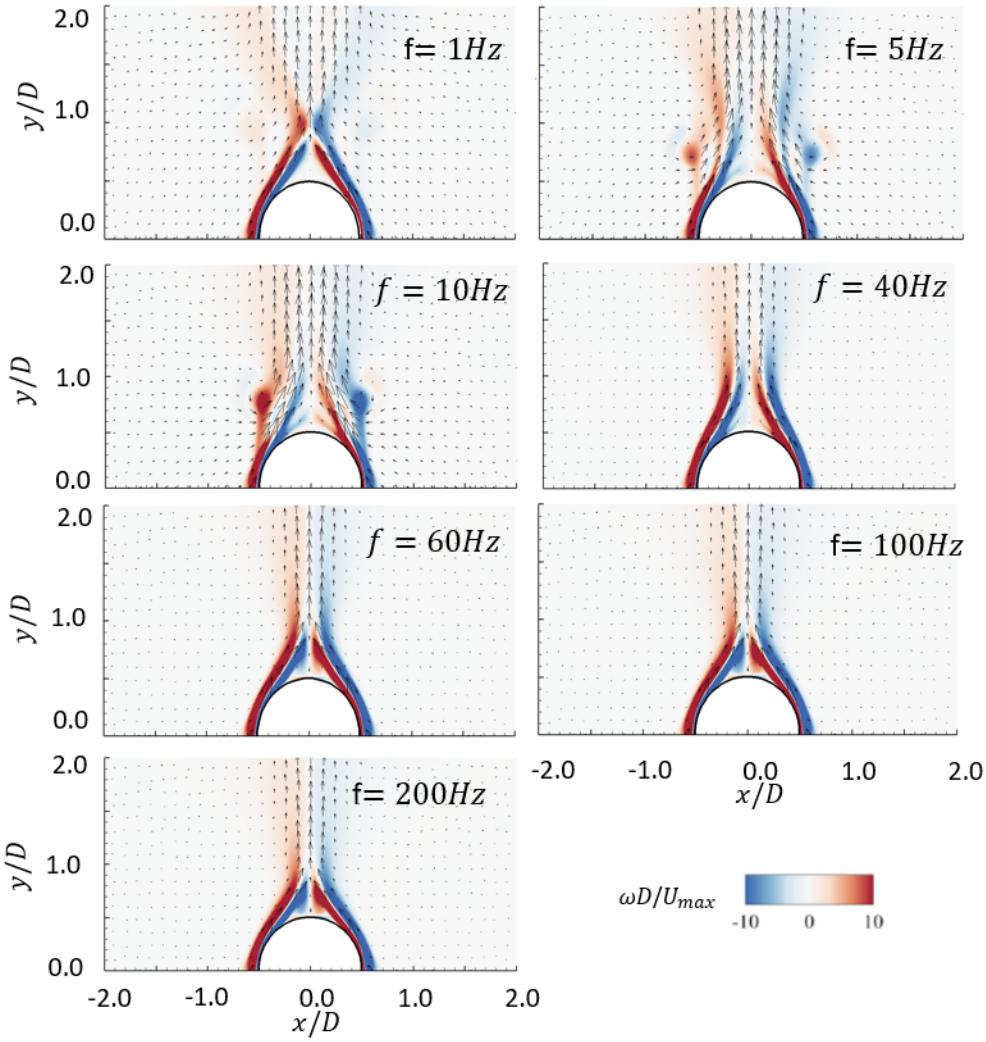

Figure 5.25: Time-averaged velocity vectors over vorticity contours for $\tau = 0.5$ at different frequencies

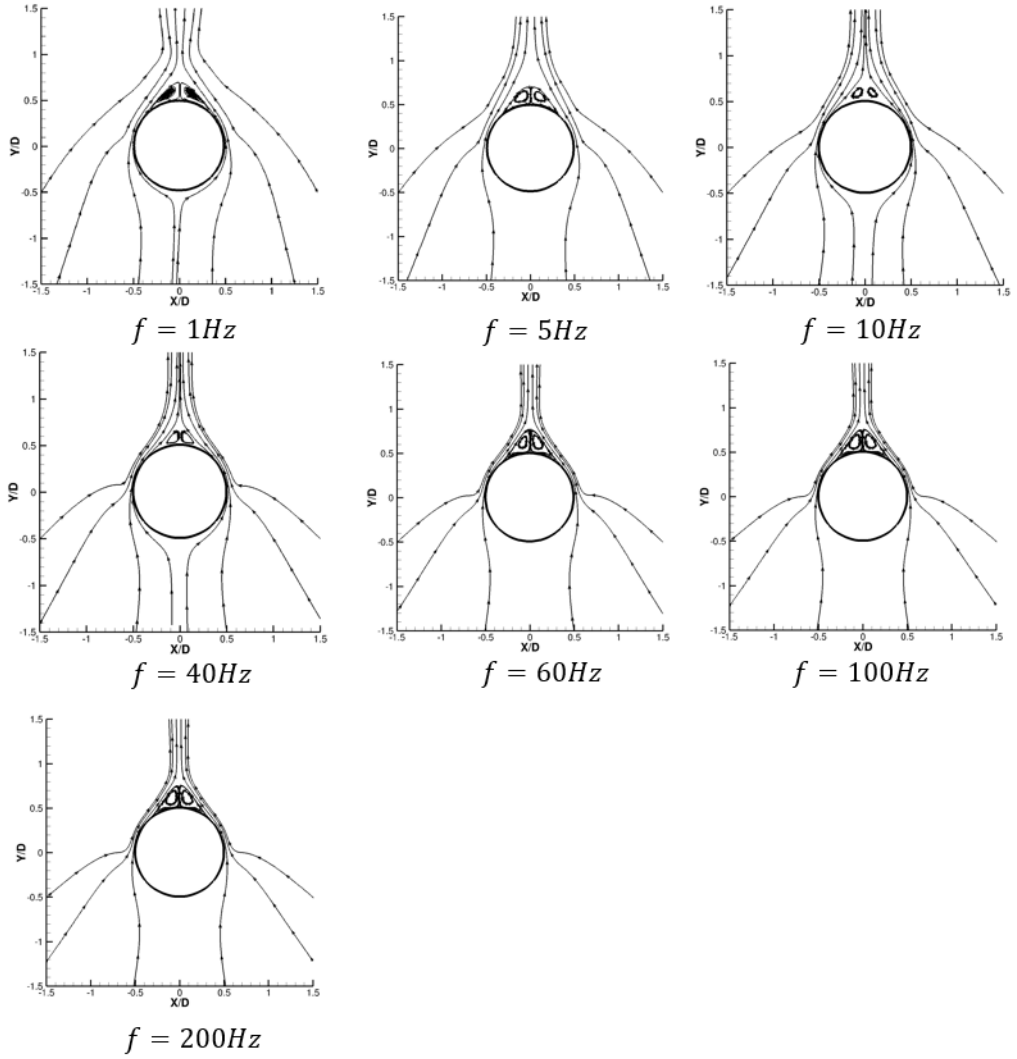

Figure 5.26: Time-averaged streamlines under different duty-cycle frequencies when $\tau = 0.5$

Figure 5.27 shows the time-averaged plasma body force, friction and pressure coefficient along the cylinder surface. All the parameters are symmetric and do not show much variation with respect to the duty-cycle frequency.

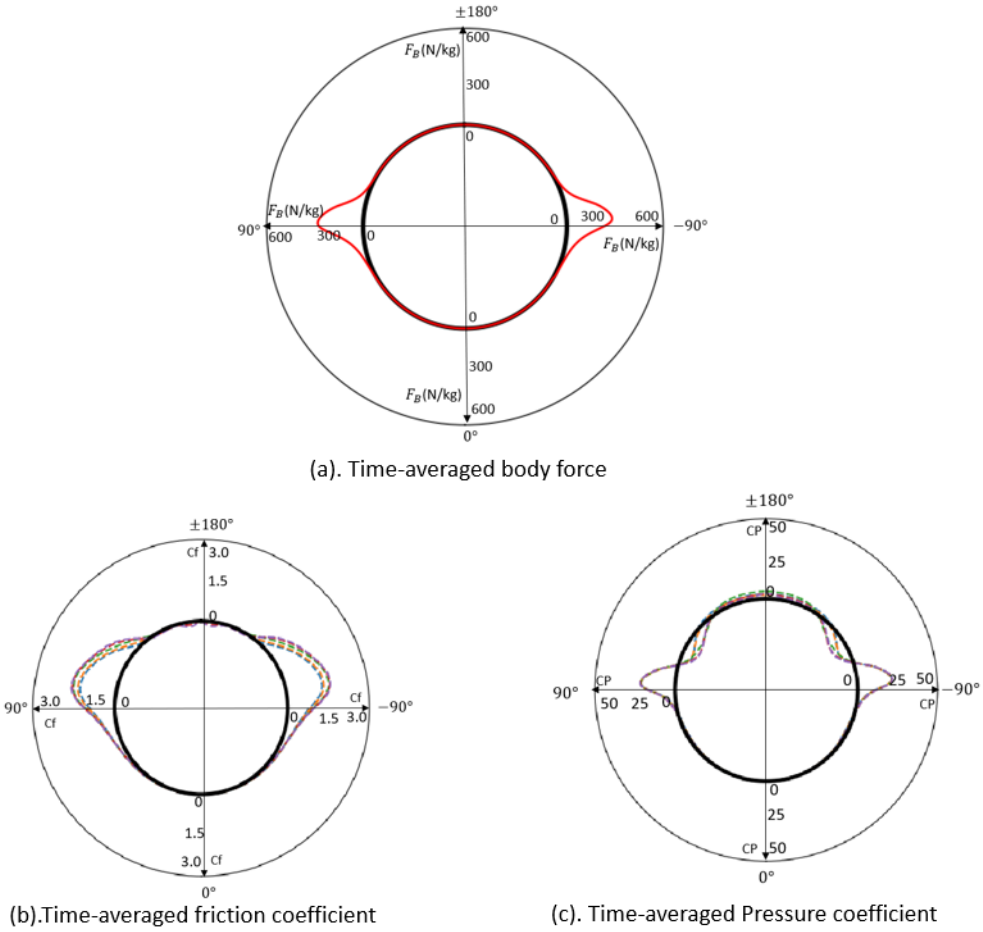

Figure 5.27: Parameters along the cylinder surface for $\tau = 0.5$ at different frequencies

Figure 5.28 shows the time-averaged momentum and maximum velocity when $\tau = 0.5$. The momentum in the x-direction is approximately zero since the momentum induced by the left and right wall jets cancel each other out. In the simulation, the maximum velocity is bigger due to the bigger plasma body force required to get accurate results. The momentum in the y-direction is smaller because the combined jet in the simulation travel a shorter distance comparing to the combined jet in the experiment, as evidenced in Figure 5.29. Comparing Figure 5.28(b) with Figure 5.21(b), we can see that the time-averaged velocity is higher when $\tau = 0.3$ because of the stronger time-averaged wall jet induced by the right actuator.

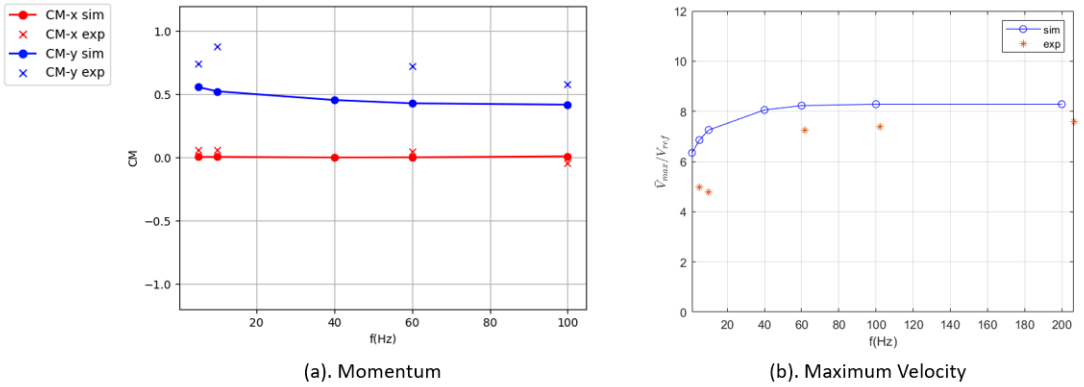

Figure 5.28: Time-averaged momentum and maximum velocity when $\tau = 0.5$

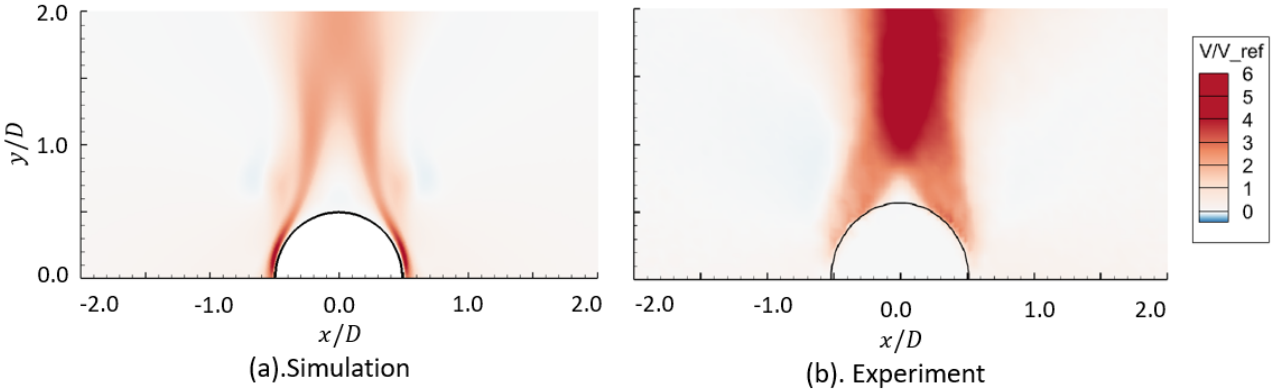

Figure 5.29: Comparison between the simulated velocity contours and the experimental velocity contours.

When the duty-cycle ratios $\tau = 0.7$ and $\tau = 0.99$, the body force fields are the mirror image of the cases when the duty-cycle ratio $\tau = 0.3$ and $\tau = 0.01$, as can be seen in Figures 5.30 and 5.31. In these two cases, the body force is stronger on the left side and weaker on the right side. As a result, the wall jet on the left side is stronger than the wall jet on the right side, as can be seen in Figures 5.30 and 5.31. The flow fields for $\tau = 0.7$ and $\tau = 0.99$ are also the mirror images of the flow fields for $\tau = 0.3$ and $\tau = 0.01$, as can be seen in Figure 5.32 and Figure 5.33.

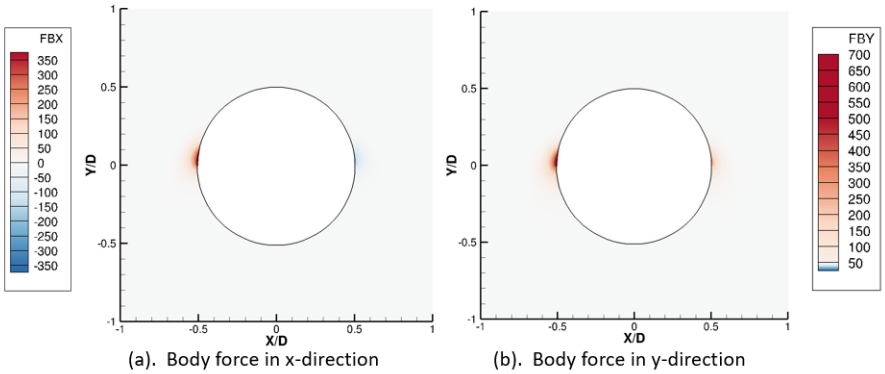

Figure 5.30: Time-averaged plasma body force contours for $\tau = 0.7$ at different frequencies

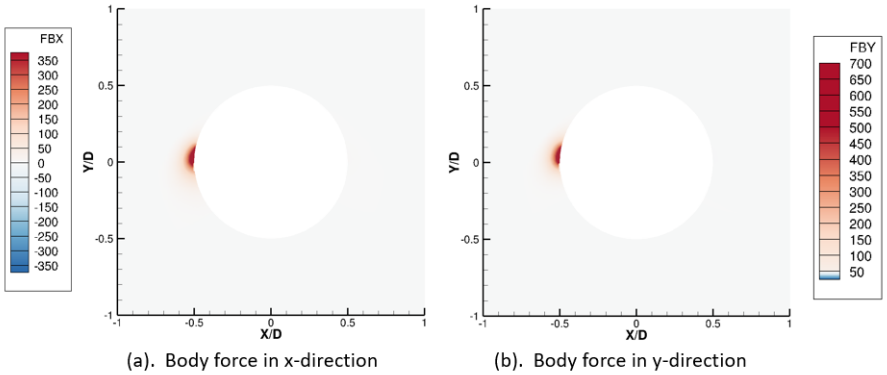

Figure 5.31: Time-averaged plasma body force contours for $\tau = 0.99$ at different frequencies

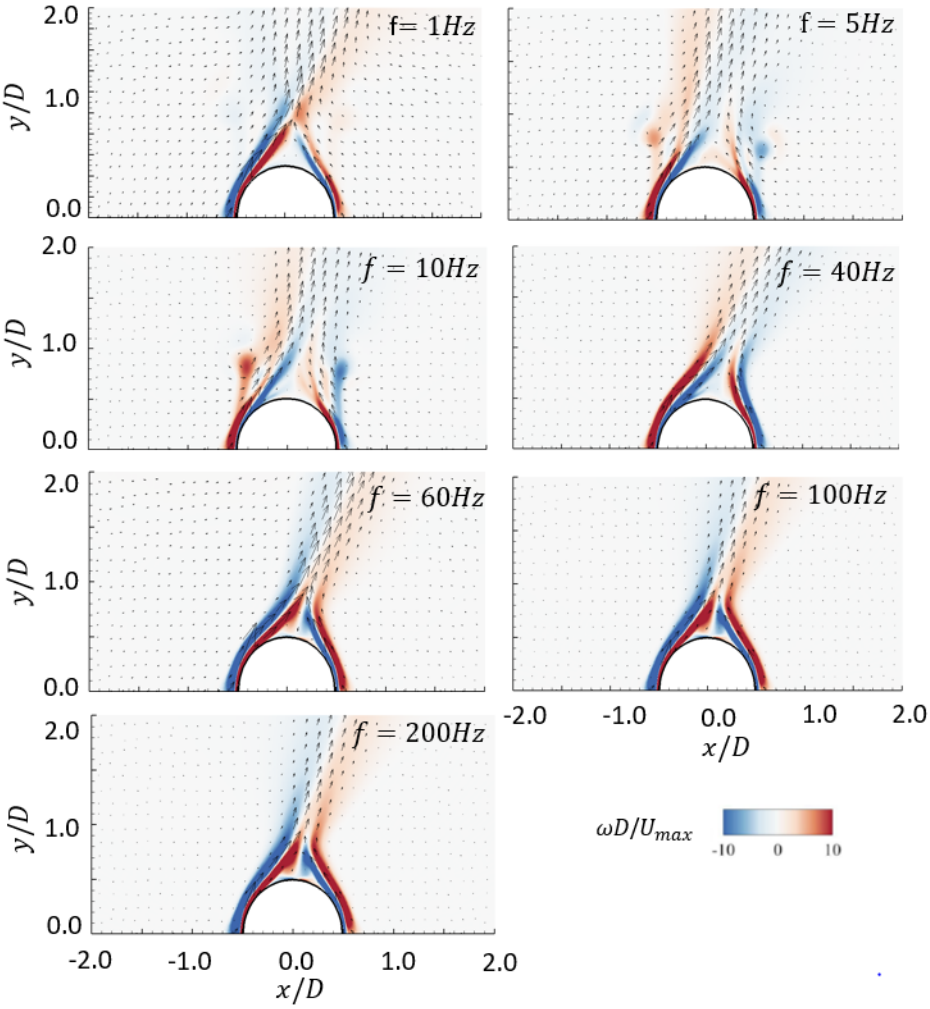

Figure 5.32: Time-averaged velocity vectors over vorticity contours for $\tau = 0.7$ at different frequencies

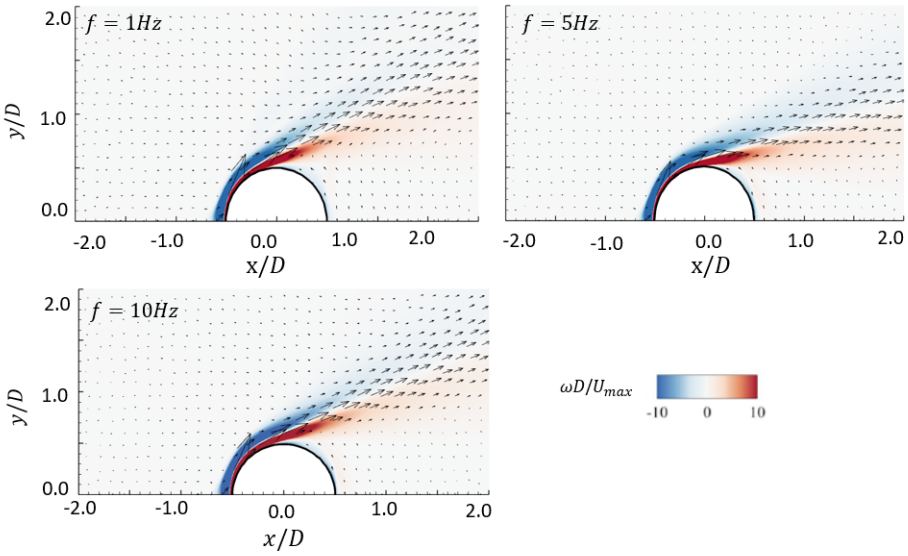

Figure 5.33: Time-averaged velocity vectors over vorticity contours for $\tau = 0.99$ at different frequencies

5.2.2 Vortex motion in one duty-cycle period

In this subsection, we study the time-accurate flow field under different plasma actuation signals. In each case, 6 pictures of the time-accurate velocity vectors on top of the vorticity contours are presented in one duty-cycle period. Then, the total plasma body force, momentum and surface force in the x and y directions are plotted and studied in details. The results were recorded after the flow field becomes stable, which is about 20 duty-cycle periods after starting. Upon reaching stability, the flow field does not show any significant changes from one period to another, despite some minor differences caused by the turbulence effect. In order to get rid of minor turbulent effects, the contours shown below are the phase-averaged results of 5 consecutive periods.

5.2.2.1 Time-accurate contours for different duty-cycle ratios at $f = 5Hz$

Figure 5.34 shows a comparison between the simulation results and experimental results for $\tau = 0.5$ and $f = 5Hz$ at different phases in one period. A wall jet is generated on the left side of the cylinder under plasma actuation. Due to the entrainment of air, this jet rolls up to form a vortex structure rotating in the counter clockwise direction while traveling upwards. At 50% of the duty-cycle period, the plasma actuator on the left side is switched to the plasma actuator on the right side. As a result, a similar vortex is generated on the right side which travels in the upper left direction. Eventually, both vortices will dissipate due to the viscosity of air. Since the strength of the plasma body force is equal on each side, the vortex motion on the left is the mirror image of the vortex motion on the right. The simulation results show good agreement with experimental results, providing validation for the CFD code's ability to simulate time-accurate flow fields. However, there is one small discrepancy, the vortices generated in the simulation is slightly smaller than those generated in the experiment, and the reason for this needs further study.

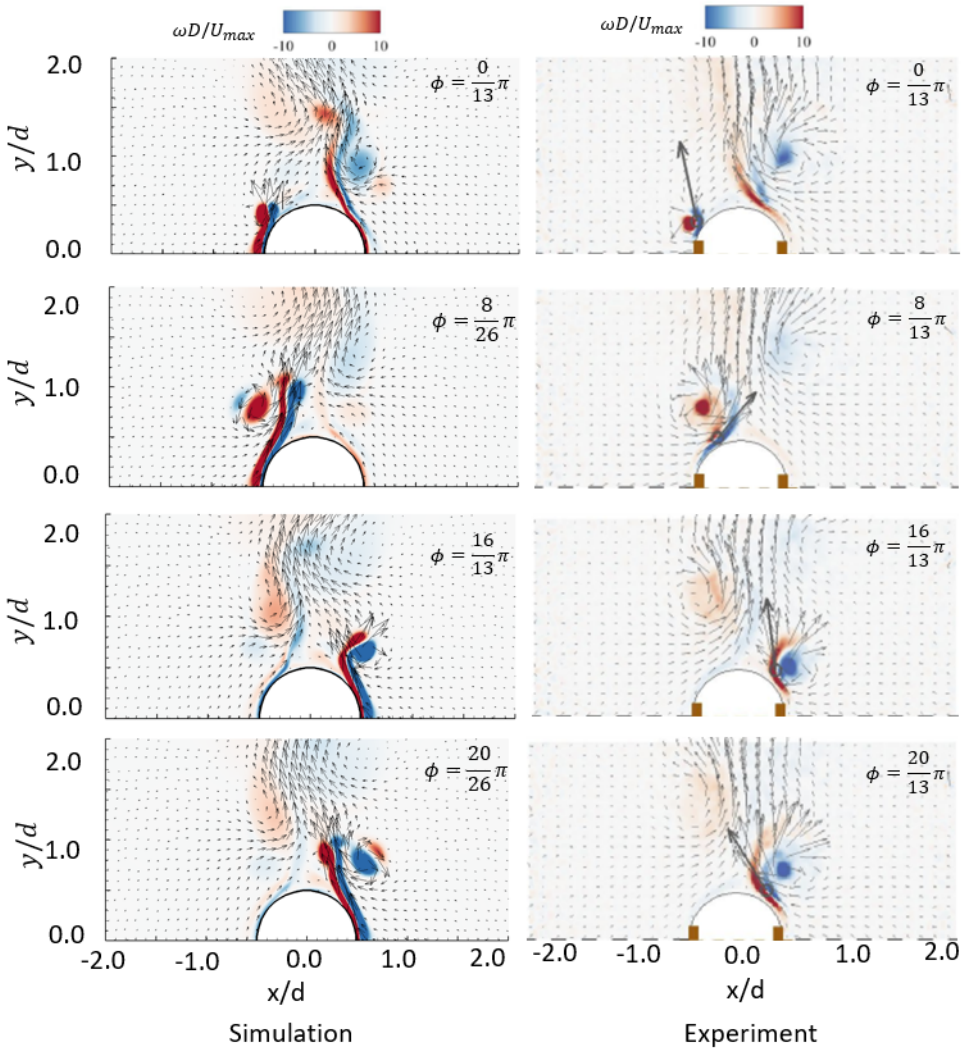

Figure 5.34: Numerical and experimental velocity vectors over vorticity fields for $f = 5Hz, \tau = 0.5$

Figure 5.35 shows the force and momentum when $\tau = 0.5$ and $f = 5Hz$. As we can see in Figure 5.35(a), the plasma body force in the y-direction is constant throughout the entire duty-cycle period. The plasma body force in the x-direction is positive for the first half of the duty-cycle period and negative for the second half. The momentum in the x-direction shows an arc shape while the momentum in the y-direction is almost a constant. In the first half of the period, the momentum in the x-direction increases due to the right-running vortex generated on the left side. In the second half of the period, the momentum in the x-direction

decreases due to the left-running vortex generated on the right side. The momentum in the y-direction is always positive because the vortices on both sides are always traveling upwards no matter which actuator is turned on. The behavior of the pressure force on the cylinder surface is much more complicated with multiple peaks and valleys. When the left actuator is turned on, a high pressure region is created on the left, inducing a sharp peak in the pressure force. Later on, the pressure decreases as the pressure energy transforms into the kinetic energy of the wall jet. When the vortex travels away from the wall, the pressure slowly starts to recover and the pressure force in the x-direction slowly starts to become positive again. When $t/T = 0.5$, the left actuator is switched to the right actuator, creating a high pressure region on the right side which is able to induce a pressure force pointing in the negative x-direction. Then the same process is repeated on the right side of the cylinder. For most part of the duty-cycle period, the body force in the y-direction is negative due to the high pressure region induced by the plasma actuators on the upper surface of the cylinder a short distance downstream of the plasma actuator. The friction force in the x-direction shows large variation throughout one period while the friction force in the y-direction is always positive with smaller oscillations. In the first half of the period, a right-running wall jet is induced by the left vortex traveling to the right. As the vortex travels downstream, the wall jet along the cylinder surface becomes longer and the friction force becomes higher. In the second half of the period, the motion of the flow field mirrors the first half, resulting in a decreasing friction force in the x-direction. The two peaks in Figure 5.35(e) are induced by the sudden plasma actuation on both sides.

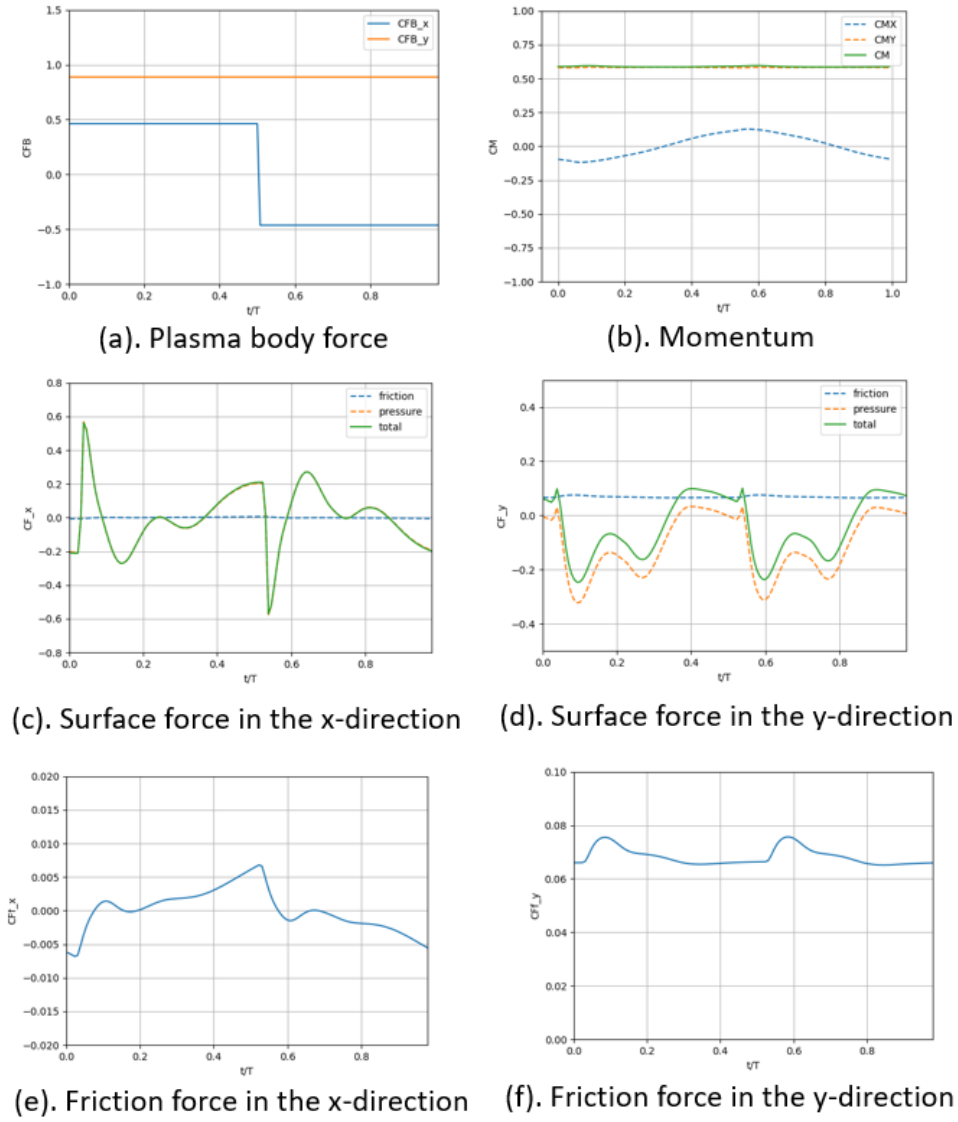

Figure 5.35: Force and momentum throughout one period when $f = 5Hz, \tau = 0.5$

Figure 5.36 shows the Fourier analysis results of the momentum, friction force and pressure force. The Fourier analysis of all parameters are conducted after subtracting their corresponding time-averaged values. Due to the plasma body force being a step function, the amplitude of the Fourier transformation of the plasma body force in the x-direction shows gradually decaying peaks at $f = 5, 15, 25Hz$, with the second peak approximately equaling to 1/3 of the first peak. Since the plasma body force in the y-direction is just a flat line, no

peaks are generated in its Fourier results. The Fourier transformation of the x-momentum shows one large peak at $f = 5Hz$, dwarfing the peaks at all other frequencies, indicating that the x-momentum is mostly dependent on the duty-cycle signal. In comparison, all the peaks in the y-momentum are very small because the fluctuations in the y-direction are negligible. For the friction force in the x-direction, the dominant frequency equals to $f = 5Hz$ and the peaks of the x-friction force resembles the peaks of the x-body force, indicating that the friction force is highly dependent on the plasma body force. Surprisingly, for the x-pressure force, the peak at $f = 25Hz$ is much higher than the peak at the duty-cycle frequency. This is likely to be caused by the five summits in one duty-cycle period, as shown in Figure 5.35(e). The dominant frequency for the pressure and friction force in the y-direction equals to $10Hz$ because its pattern repeats twice in every duty-cycle period, as shown in Figure 5.35(d) and (f). Although the direction and the magnitude of the plasma body force does not change, its location switches twice in every duty-cycle period, and the signal created by the switching effect is $f = 10Hz$. So, it is safe to conclude that the oscillations of the y-friction force is caused by the actuation signal of the switching effect.

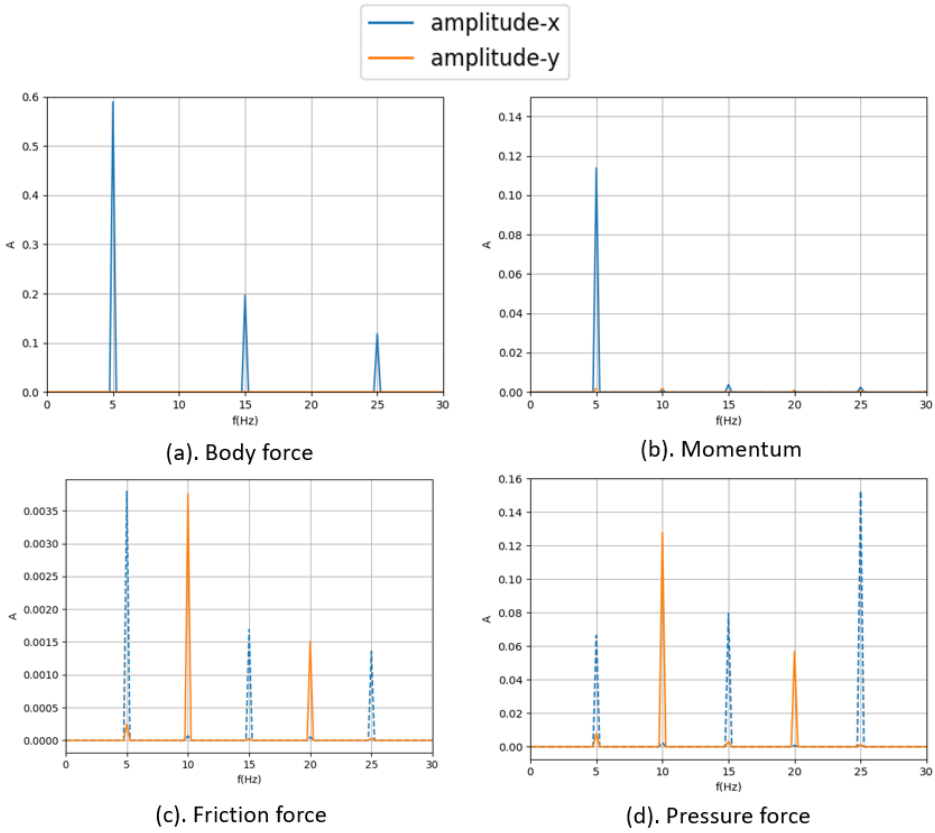

Figure 5.36: The amplitude for $f = 5Hz, \tau = 0.5$

Figure 5.37 shows the contours appearing at the five peaks of the x-pressure force. The first peak is induced by the vortex generated on the left side. The second peak is induced by the separation of the shear layer attached to the primary vortex. The third peak is induced by the generation of the right vortex. The fourth peak is induced by the separation of the shear layer attached to the primary vortex. The fifth peak is induced by the primary vortex breaking down into several small vortices.

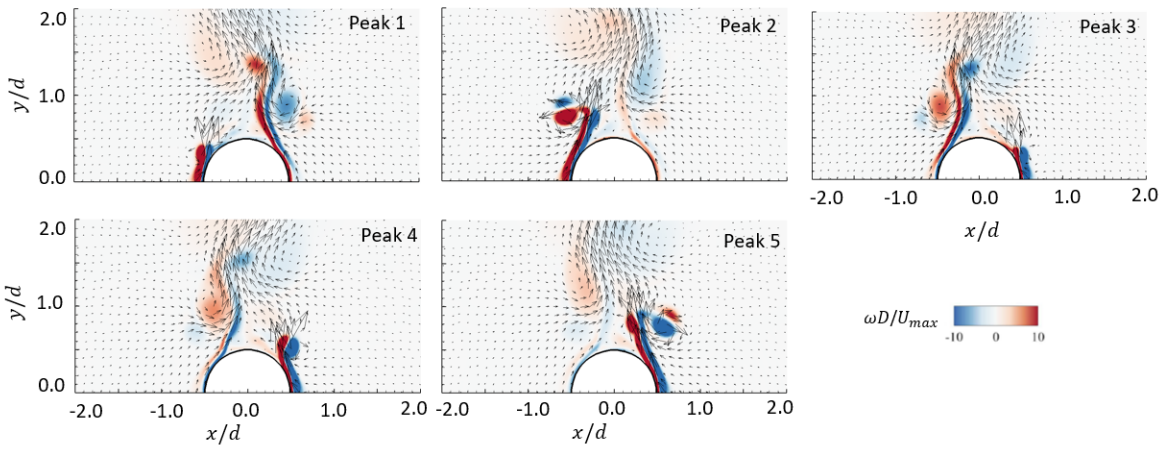

Figure 5.37: The contours at the peaks of the x-pressure force

Figure 5.38 shows the phases of the plasma body force and the phase delays of the momentum, pressure force and friction force. The phase delays are calculated by the phases of each parameter minus the phase of the plasma body force, and only the phase delays of the major frequencies (Frequencies whose peak is larger than 10% of the dominant peak) will be studied. For the x-body force, the phases are approximately the same at every major frequency due to the force being a step function. For the x-momentum, the phase shift of the major frequency equals to about $-90°$, indicating a time delay of around 1/4 of the duty-cycle period between the momentum and body force in the x-direction. The phase shifts of the friction force in the x-direction are approximately zero at all major frequencies, indicating that the friction forces are able to react instantly to the plasma body force. The friction force in the y-direction shows a phase shift of about 300° at the dominant frequency. Since the actuation signals for the position switch of the y-plasma body force are also caused by the duty-cycle signal, the phase of the switching effect is likely to be similar to the phase of the plasma body force in the x-direction. Since the fluctuations of the y-friction force is induced by the switching effect, it is normal for the phase of the friction force to approximate the phase of the plasma body force in the y-direction. The phase shifts of the pressure force are complicated because the pressure force is influenced not only by the plasma body force,

but also by the mutual interaction of the vortices. The study of the phase shifts for the pressure force is beyond the scope of this thesis.

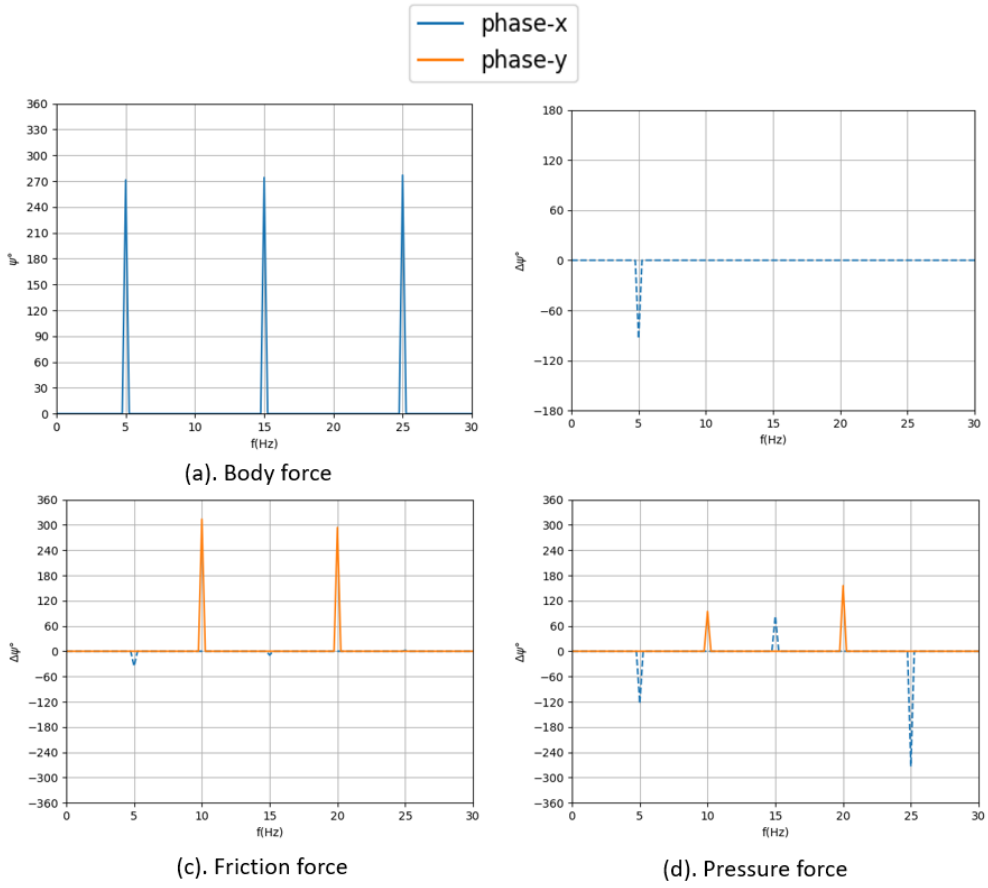

Figure 5.38: The phase for $f = 5Hz, \tau = 0.5$

Figure 5.39 shows the comparison between the force and momentum between the phase-averaged values and the values of the last duty-cycle period. Generally speaking, these results show good agreement, indicating that the flow field has reached stability on a quantitative level.

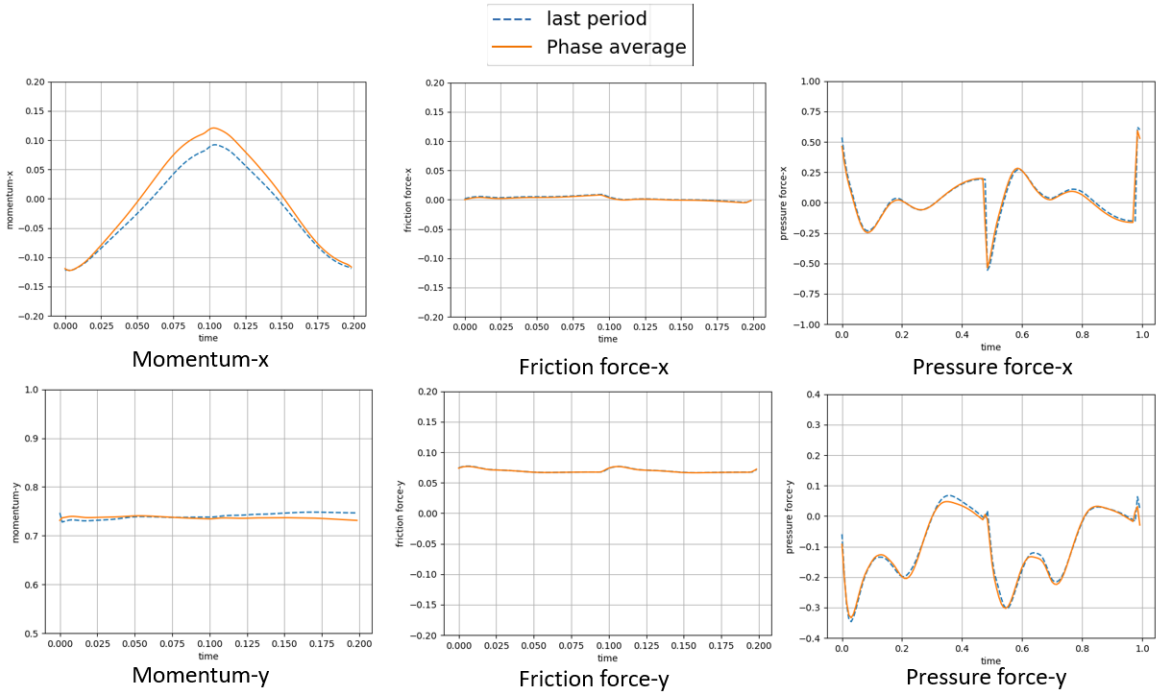

Figure 5.39: Force and momentum throughout one period when $f = 5Hz, \tau = 0.5$

Figure 5.40 shows the vortex propagation at different phases when $f = 5Hz, \tau = 0.3$. Similar to the previous case, a vortex is generated on the left side of the cylinder and travels in the upper right direction. At around 30% of the period, another vortex is generated from the right side of the cylinder, traveling in the upper left direction. Eventually, both vortices dissipate due to the viscosity of air, leaving a combined jet traveling to the upper left direction throughout the period. The combined jet is tilted to the left due to the stronger wall jet on the right side.

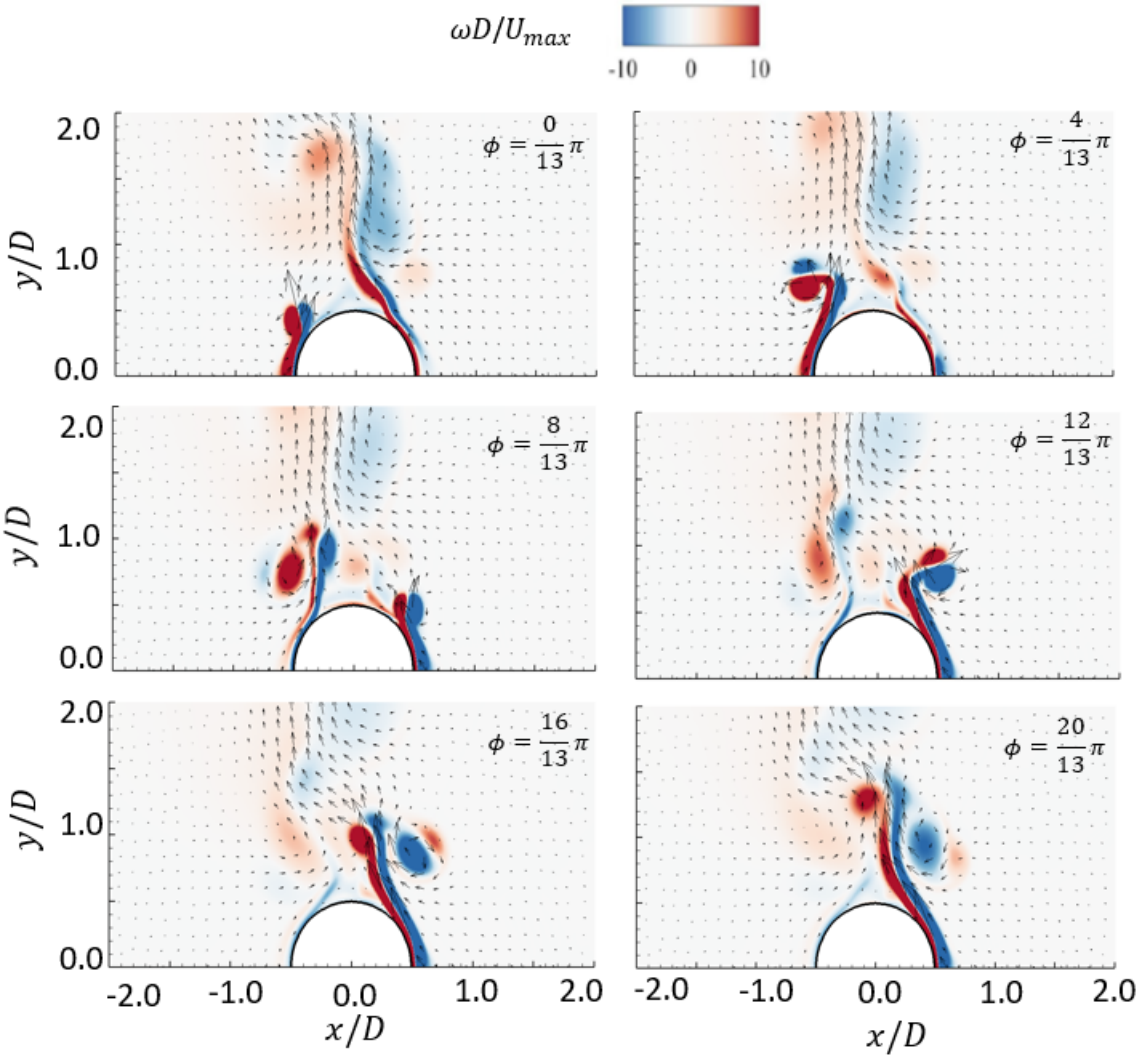

Figure 5.40: Velocity-vectors over vorticity contours for $f = 5Hz, \tau = 0.3$

Figure 5.41 shows the force and momentum when $f = 5Hz$ and $\tau = 0.3$. The behaviors of the time-accurate force and momentum are very similar to the previous case when $\tau = 0.5$, except this time the change in direction occurs at 30% of the period.

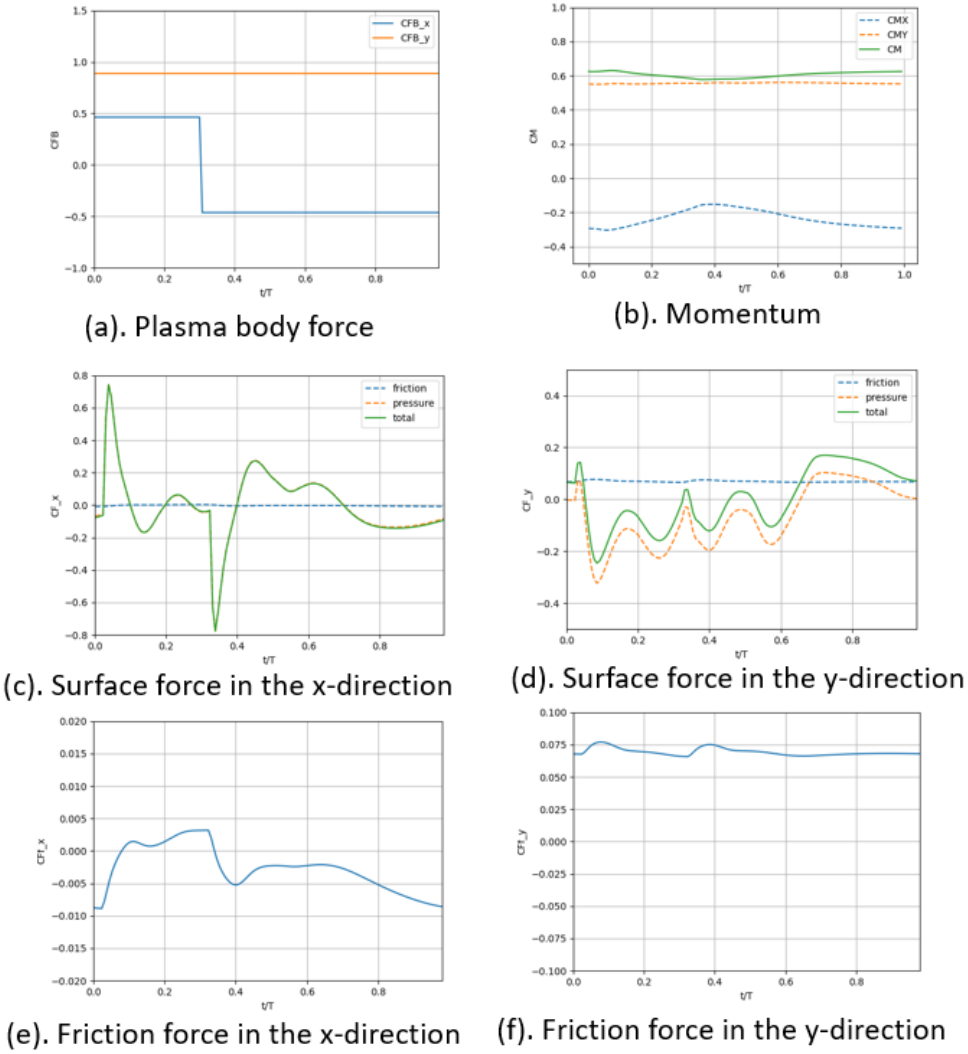

Figure 5.41: Force and momentum throughout one period when $f = 5Hz, \tau = 0.3$

Figure 5.42 shows the amplitudes of the Fourier transformation of the force and momentum. The plasma body force shows different phases at different major frequencies due to the lower duty-cycle ratio. For the momentum, although the duty-cycle frequency is still the dominant frequency, the peak at $f = 10Hz$ is much higher comparing to the previous case, indicating

the higher frequency signal is much stronger when $\tau = 0.3$. Since the higher frequency signals are the result of vortex interaction, this figure indicates that the mutual interaction between the vortices are stronger when $\tau = 0.3$. This is because under smaller duty-cycle ratios, the right vortex appears sooner after the generation of the left vortex. As a result, the left vortex is stronger and closer to the cylinder when the right vortex is formed, increasing their mutual interaction. The Fourier results of the x-friction force resembles that of the plasma body force, indicating that this force is still highly dependent on the plasma body force. For the friction force in the y-direction, the highest peak appears at $f = 15Hz$. This peak is likely to be induced by the two summits in Figure 5.41 and the mutual interaction between the vortices on both sides of the cylinder. The Fourier results of the x-pressure force show two major peaks at $f = 10, 25Hz$. The peak at $f = 25Hz$ is the result of the five crests shown in Figure 5.41, and the peak at $f = 10Hz$ is the result of the interaction between the vortices on both sides. The highest peak for the pressure force in the y-direction appears at $f = 5Hz$, indicating the plasma actuation signal is the dominant signal.

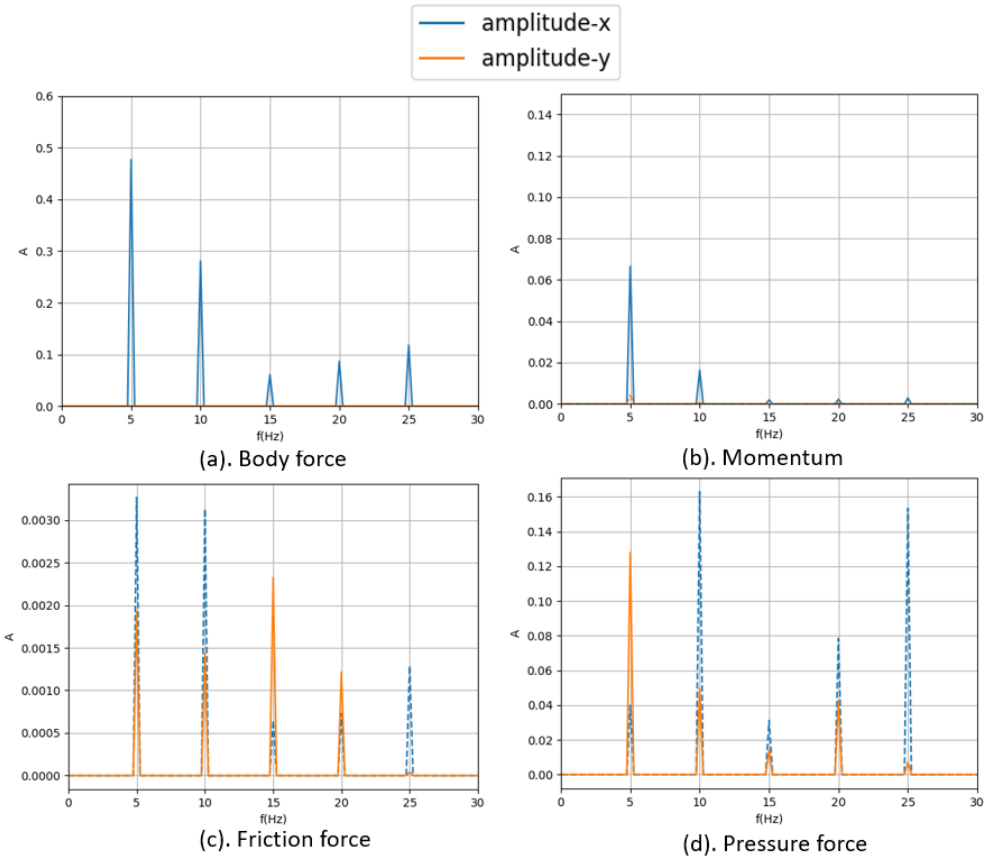

Figure 5.42: The amplitude domain for $f = 5Hz, \tau = 0.3$

Figure 5.43 shows the phases of the plasma body force, momentum, friction and pressure force. The most noticeable difference is that the plasma body force shows different peaks at different frequencies due to the plasma body force no longer being a square wave. For the momentum in the x-direction, the phase shift of the dominant frequency is still $-90°$, indicating that the time delay of the momentum is still approximately $1/4$ of the period. The phase shift is still approximately zero for the friction force in the x-direction, indicating the friction force is still highly dependent on the plasma body force at $\tau = 0.3$.

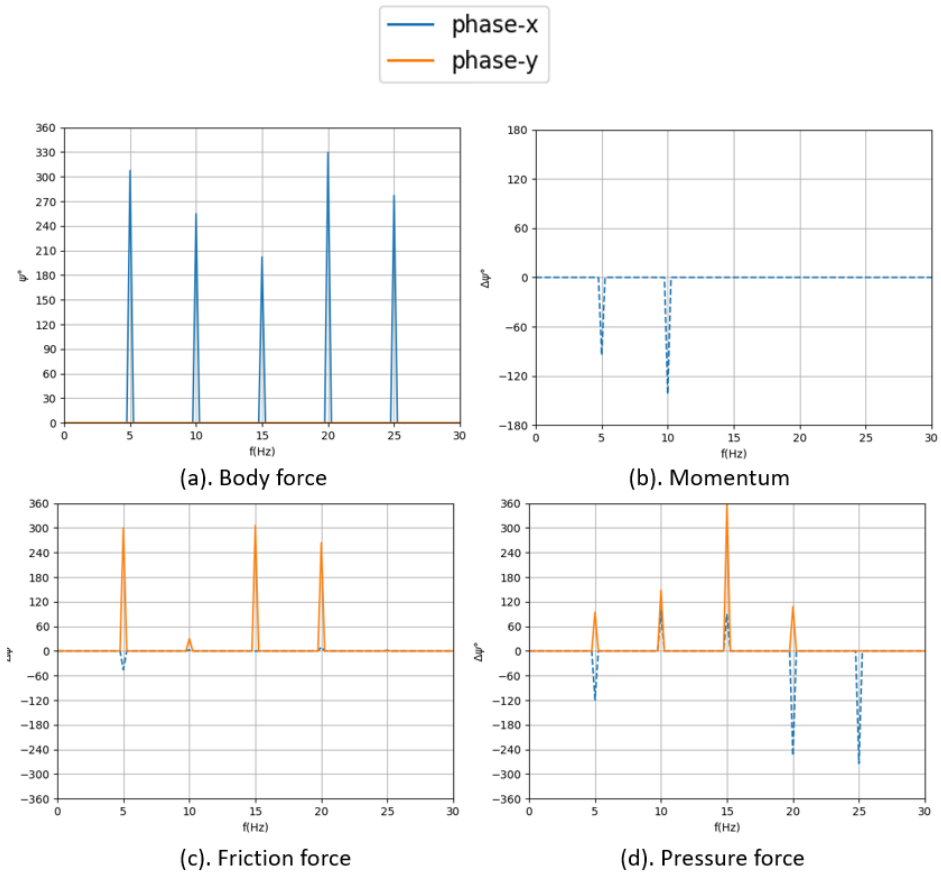

Figure 5.43: The phase domain for $f = 5Hz, \tau = 0.3$

For both duty-cycle ratios, the fast Fourier results show more major peaks for the pressure and friction force and less peaks for the momentum. This is because the momentum is dependent on the flow field of the entire domain while the friction and pressure force on the cylinder surface is mostly dependent on the flow field in the vicinity of the wall, where the plasma body force is much stronger. The multiple peaks shown in the Fourier results for pressure and friction force are the result of the multiple actuation signals present in the plasma body force. Since the plasma effect is much weaker in outer regions away from the wall, the weaker signals of the plasma body force can no longer show noticeable influence on the outer region and only the strongest signal remain, which is the duty-cycle actuation signal.

When the duty-cycle ratio $\tau = 0.7$, the vortex propagation is the mirror image of the case for $\tau = 0.3$ with the combined jet traveling in the upper right direction, as shown in Figure 5.44.

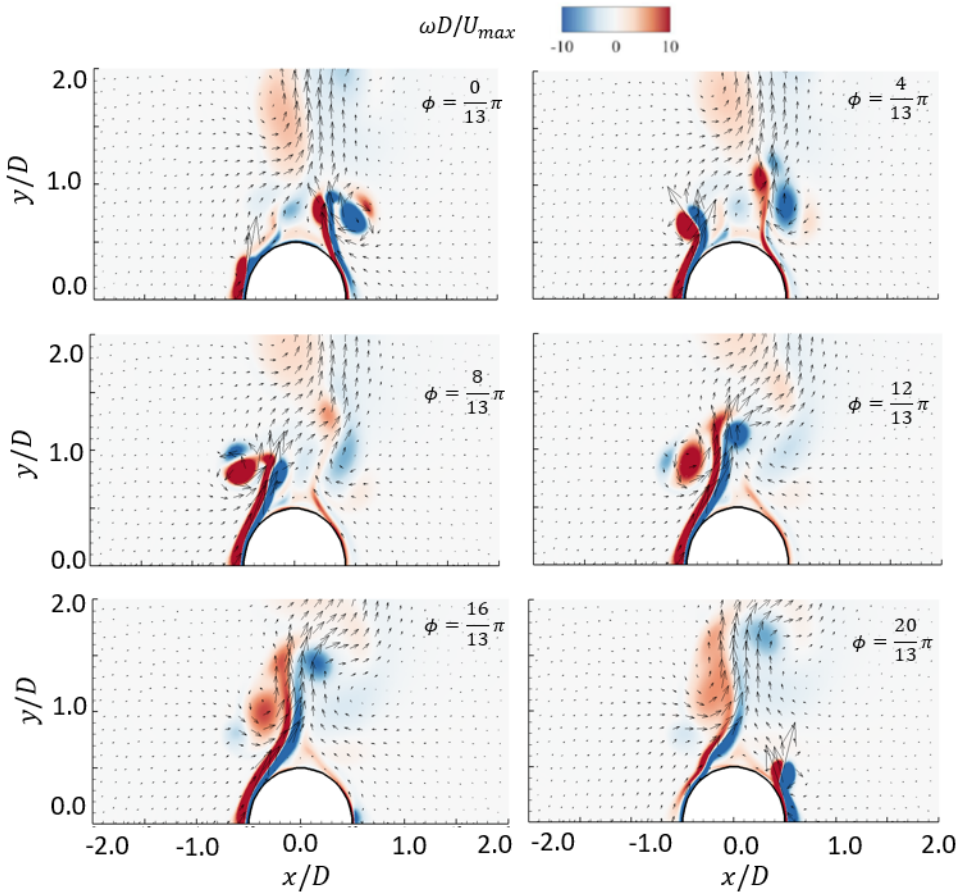

Figure 5.44: Velocity vectors overlapped with vorticity contours for $f = 5Hz, \tau = 0.7$

5.2.2.2 Time-accurate contours for different duty- cycle frequencies when duty-cycle ratio $\tau = 0.3$

The following plots show the time-accurate flow fields under different frequencies when $\tau = 0.3$. Figure 5.45 shows the time-accurate flow field when $f = 1Hz$. Similar to the case when $f = 5Hz$, one vortex is generated on each side of the cylinder. The vortex generated from the left travels in the upper right direction while the vortex generated from the right travels in the upper left direction, slowly dissipating due to the viscosity of air. Comparing to the results at $f = 5Hz$, the vortices are able to travel further downstream at this frequency because the duty-cycle period is longer for lower frequencies. When the duty-cycle ratio is fixed at $\tau = 0.3$, longer duty-cycle period implies longer plasma actuation time in one period. As a result, the vortices are able to travel further downstream.

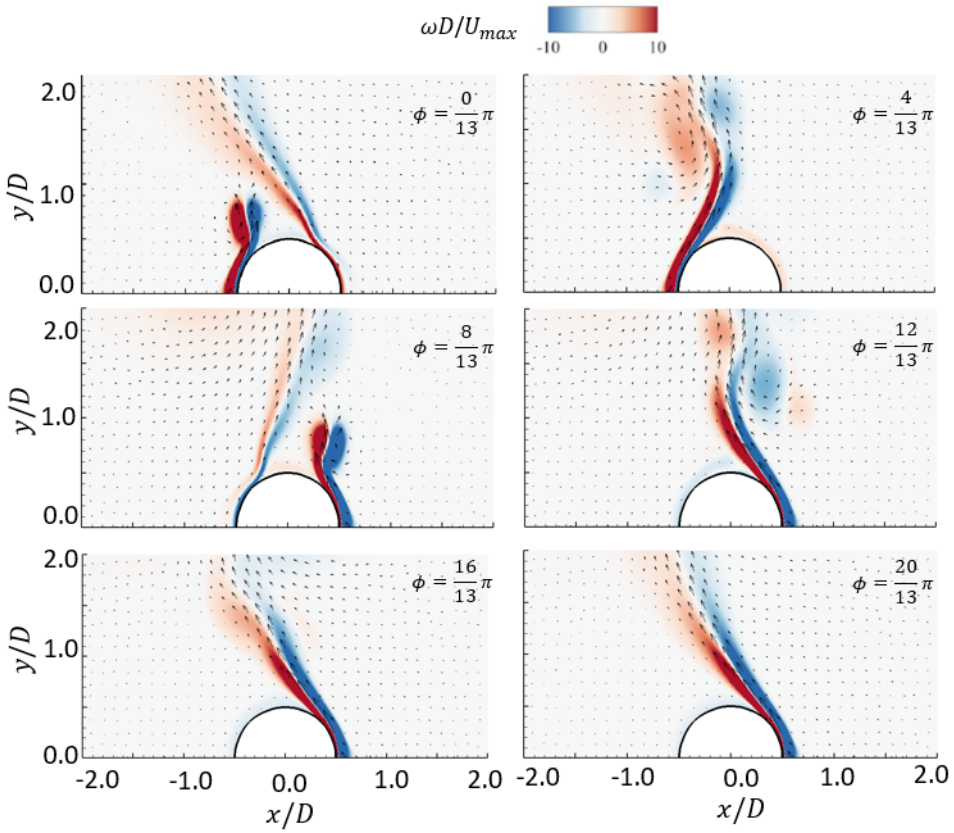

Figure 5.45: Velocity vectors over vorticity contours at $f = 1Hz, \tau = 0.3$

Figure 5.46 shows the time-accurate contours when $f = 10Hz$, where two distinct vortices are generated on both sides of the cylinder and they travel in the upper left direction, slowly dissipating due to the viscosity of air. Due to the shorter duty-cycle period at this frequency, two vortices can co-exist on each side of the cylinder. Since the distance between two vortices are still reasonably large, they do not interact with each other in any significant way.

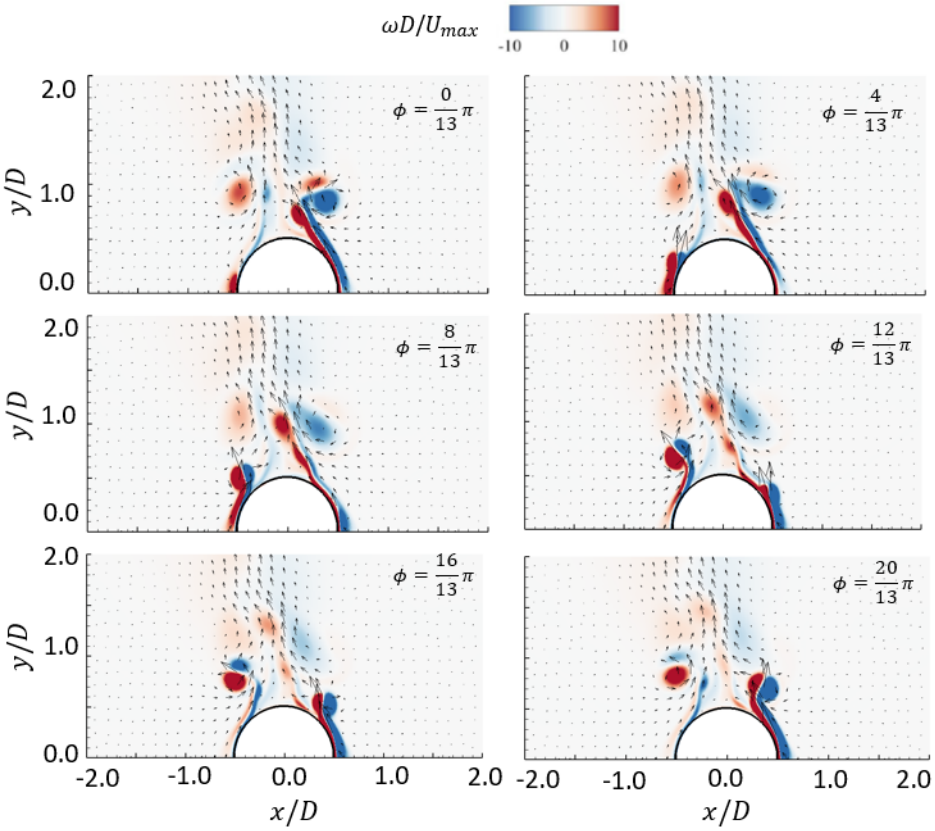

Figure 5.46: Velocity vectors over vorticity contours at $f = 10Hz, \tau = 0.3$

Figure 5.47 shows the time-accurate contours when frequency increases to $f = 40Hz$. At this frequency, the duty-cycle period becomes much shorter so the previous vortex can only travel a short distance before the next vortex is generated. As a result, the vortices are clamped together and two vortex trains are generated on both sides of the cylinder. The vortices eventually merge into one big jet above the cylinder. This jet is tilted to the left because the right jet on the right is much stronger. The vortices are much smaller compared

to the cases at lower frequencies because the plasma actuation time in each period is much smaller, leaving no time to generate bigger vortices.

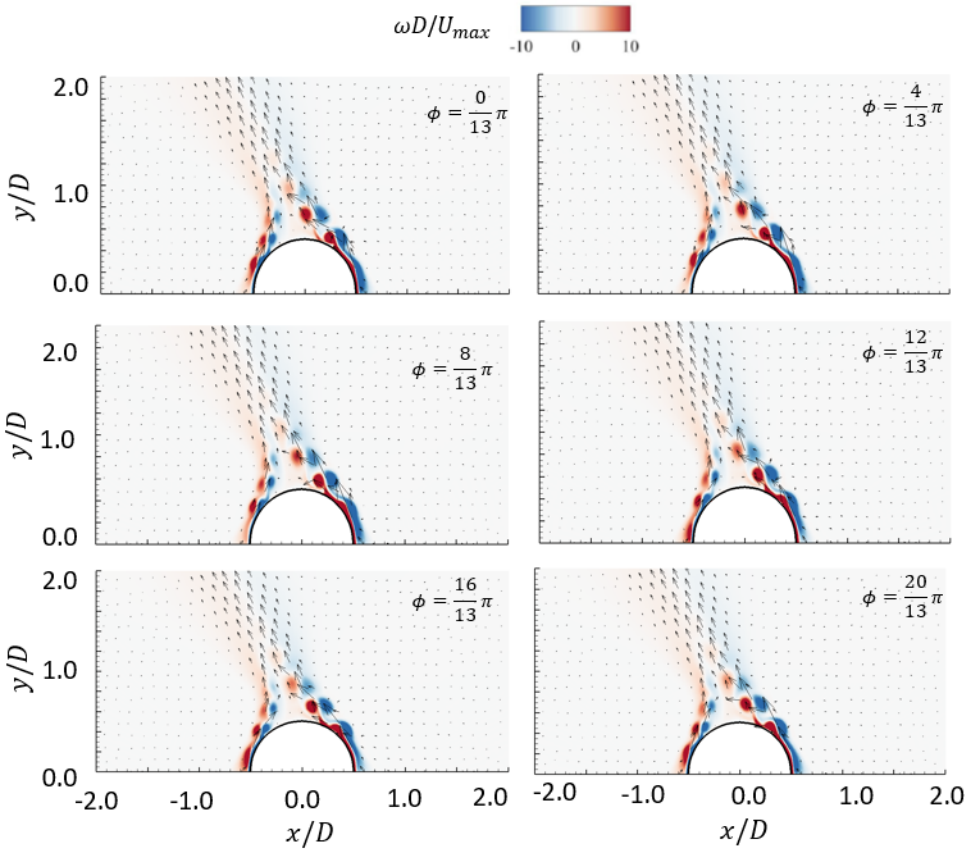

Figure 5.47: Velocity vectors over vorticity contours at $f = 40Hz, \tau = 0.3$

Figure 5.48 shows the time-accurate contours when the frequency increases to $f = 60Hz$. At this frequency, the duty-cycle period becomes even shorter and the small vortices in the wall jets start to lose their individuality and merge together. Comparing to the previous case, the two vortex trains hug closer to the cylinder surface and the combined jet is even thinner.

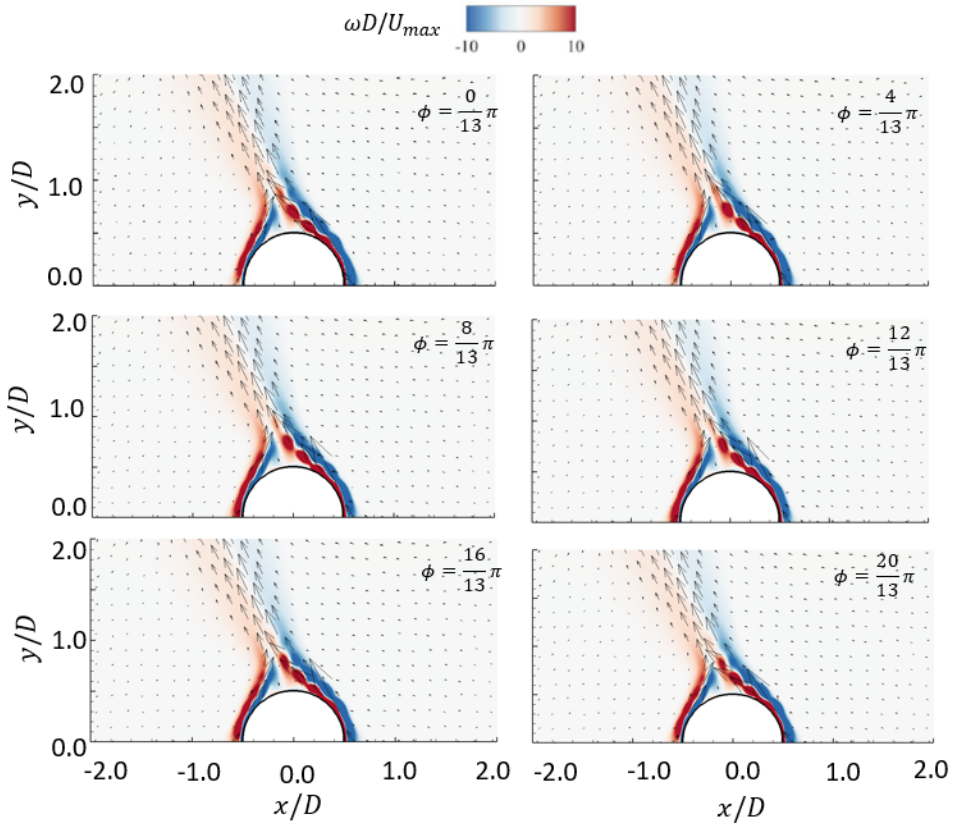

Figure 5.48: Velocity vectors over vorticity contours at $f = 60Hz, \tau = 0.3$

Figure 5.49 shows the time-accurate contours when the frequency increases to $f = 100Hz$. At this high frequency, the flow field does not have sufficient time to respond to the periodic changes in plasma actuation. As a result, the contours for $f = 200Hz$ are the same as those for $f = 100Hz$, as illustrated in Figure 5.50.

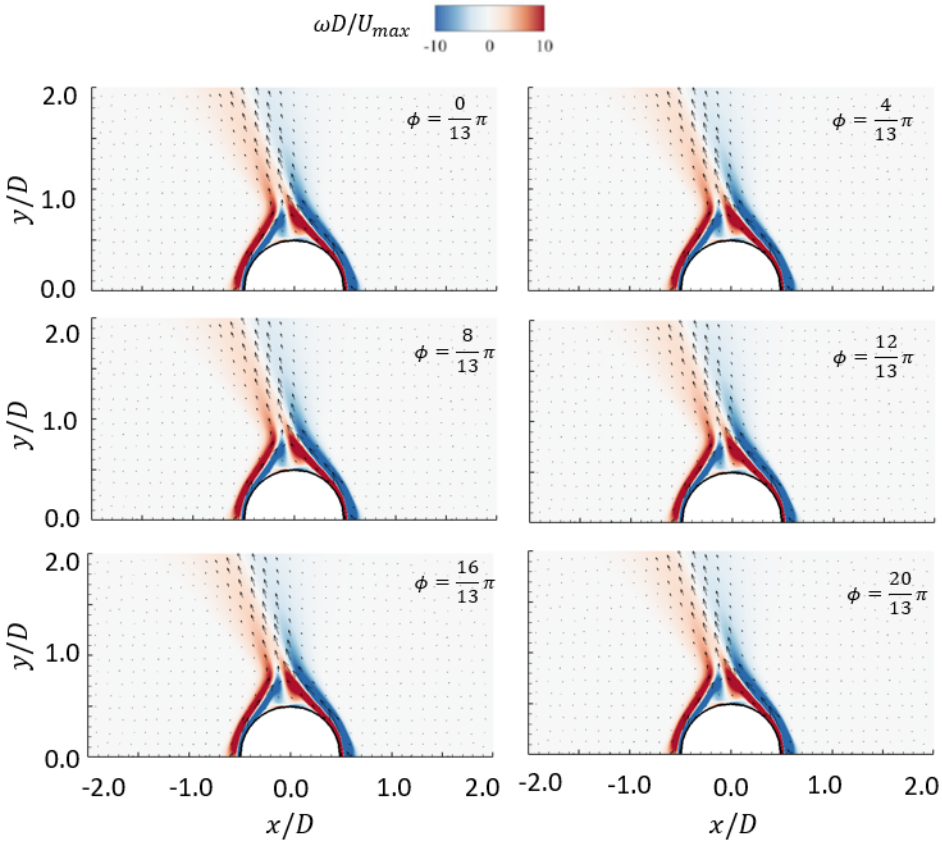

Figure 5.49: Velocity vectors over vorticity contours at $f = 100Hz, \tau = 0.3$

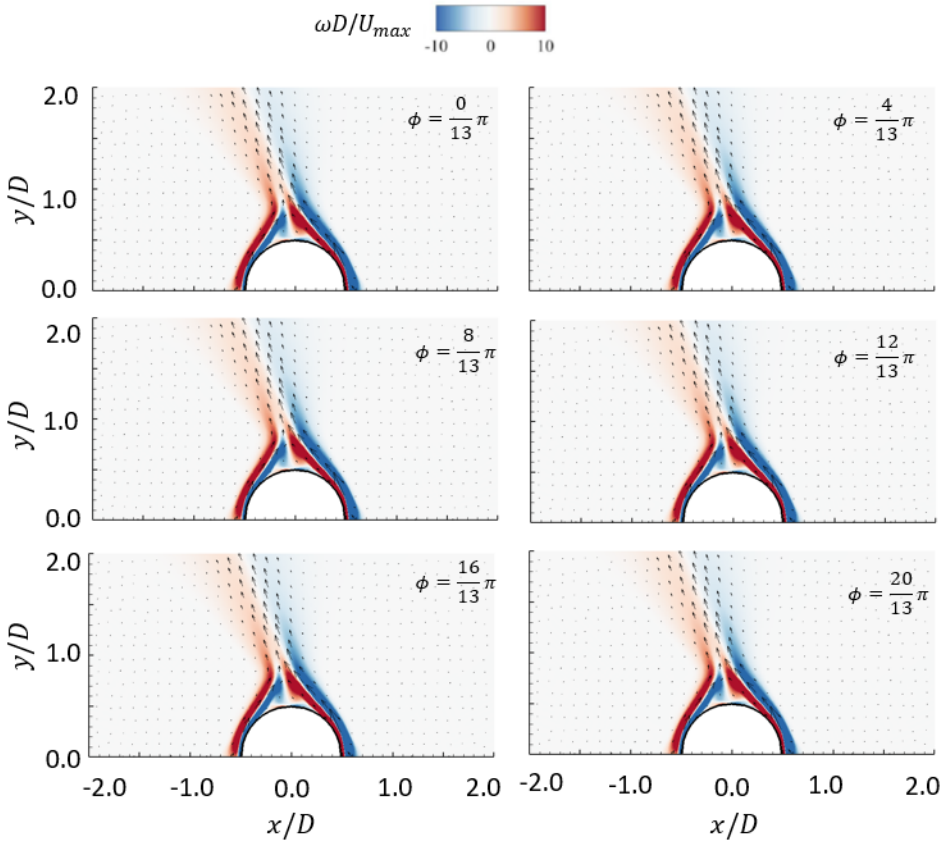

Figure 5.50: Velocity vectors over vorticity contours at $f = 200Hz, \tau = 0.3$

Figure 5.51 shows the time-accurate force and momentum under different duty-cycle frequencies when the duty-cycle ratio $\tau = 0.3$. Under lower frequencies, the momentum in the x-direction shows much larger variation in one duty-cycle period because the vortices are able to dance in sync with the plasma actuation. As a result, the overall flow field is able to shift from right-running to left-running in one duty-cycle period, resulting in the arc shape of the momentum in the x-direction. Under higher frequencies, the vortex shedding is replaced by two vortex trains on both sides of the cylinder and the flow field is relatively more stable. Consequently, the momentum and friction fluctuation in one period is much smaller under higher duty-cycle frequencies. Under lower frequencies, the pressure force in the x-direction shows a sharp peak at the beginning of the period and a sharp valley at 30% of the period. Under higher frequencies, the pressure force is positive for the first 30% of the

period and negative for the remaining 70% of the period. Both the peak and valley decays much slower for higher frequencies. The pressure oscillations for the higher frequencies are smaller than the oscillations for the lower frequencies. The pressure force in the y-direction is complicated regardless of the duty-cycle frequency.

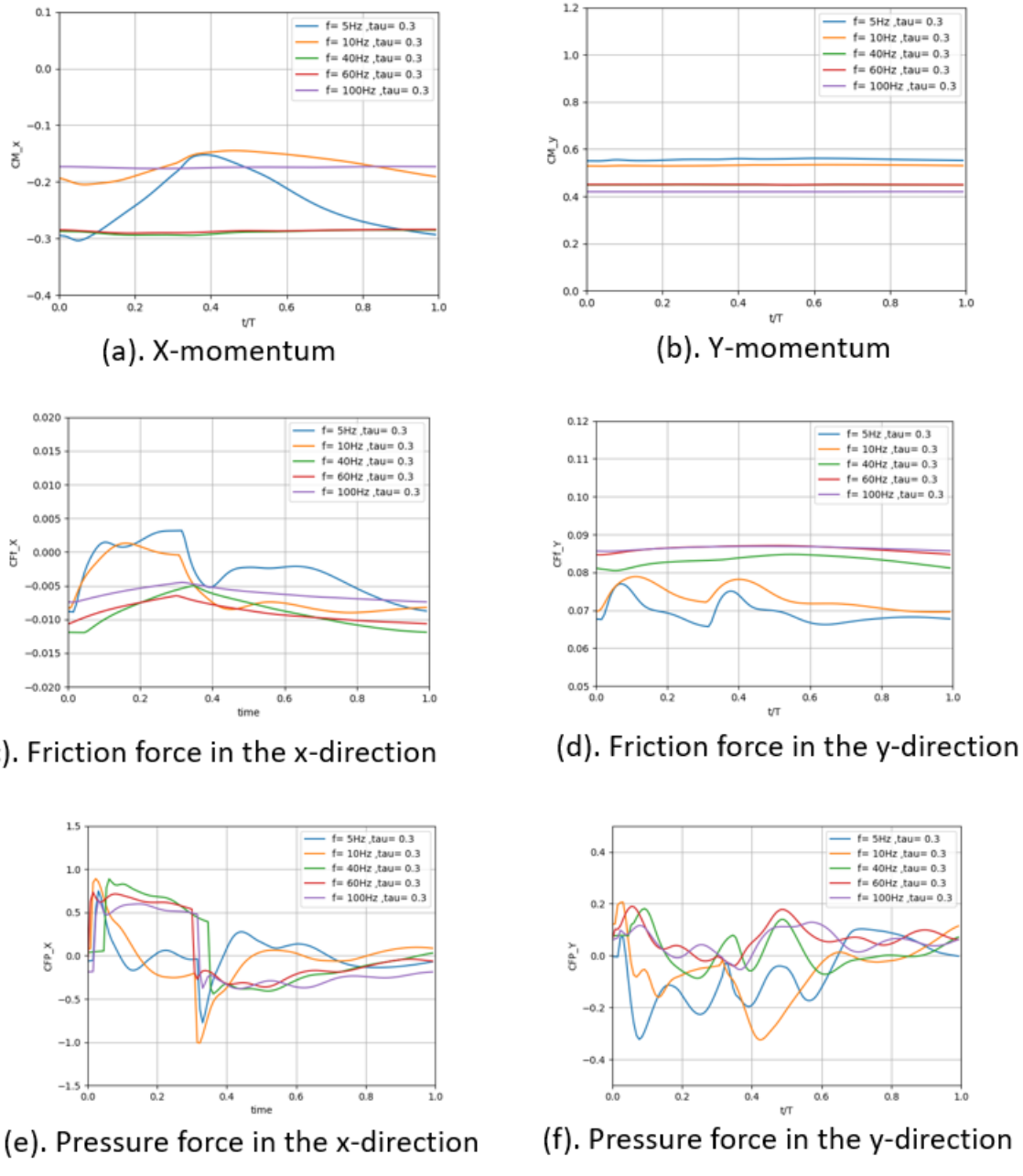

Figure 5.51: Time-accurate force and momentum when $\tau = 0.3$

5.2.2.3 Time-accurate contours for different duty- cycle frequencies when duty-cycle ratio $\tau = 0.5$

The following pictures show the time-accurate flow fields under different frequencies when $\tau = 0.5$. Figure 5.52 shows the time-accurate flow field when $f = 1Hz$. Similar to the case when $f = 5Hz$, one vortex is generated on each side of the cylinder. The vortex generated from the left travels in the upper right direction while the vortex generated from the right travels in the upper left direction. The vortices start to dissipate as they travel downstream due to the viscosity of air.

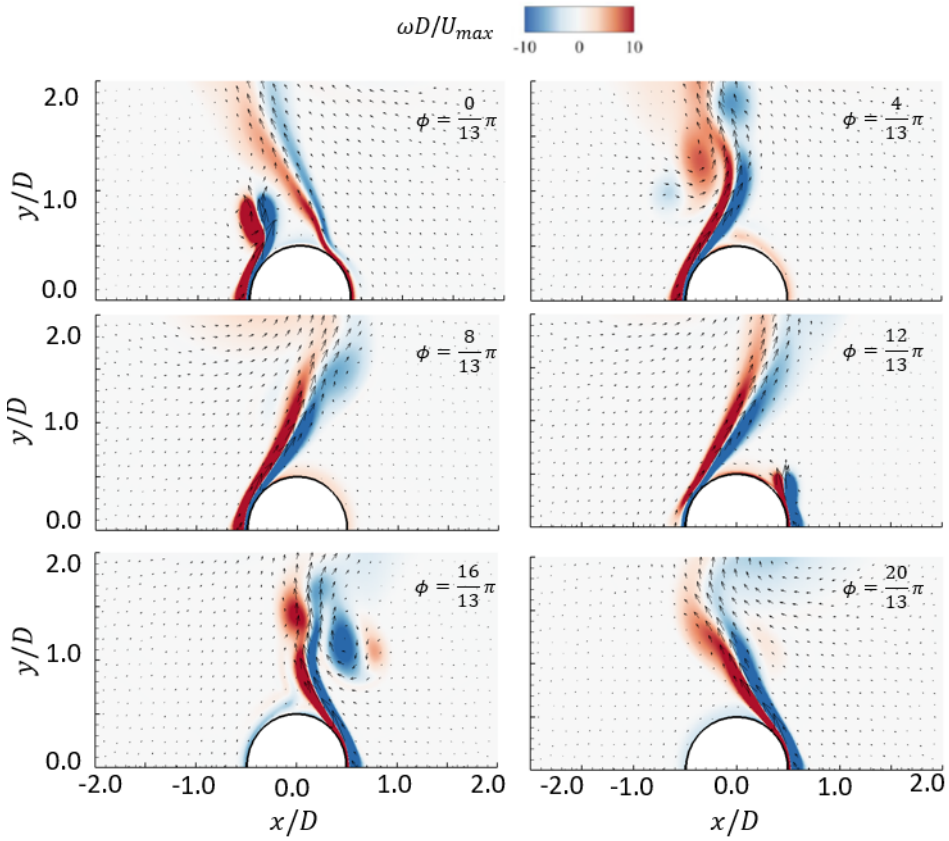

Figure 5.52: Velocity vectors over vorticity contours at $f = 1Hz, \tau = 0.5$

Figure 5.53 shows the time-accurate flow field when $f = 10Hz$. At this frequency, two distinct vortices are generated on each side of the cylinder. Comparing to lower frequency

cases, the biggest difference is that the two vortices appear simultaneously on each side of the cylinder because each duty-cycle period is shorter and the previous vortex is not fully dissipated when the new vortex is generated. Since these two vortices are far apart, they do not interact with each other in any significant way.

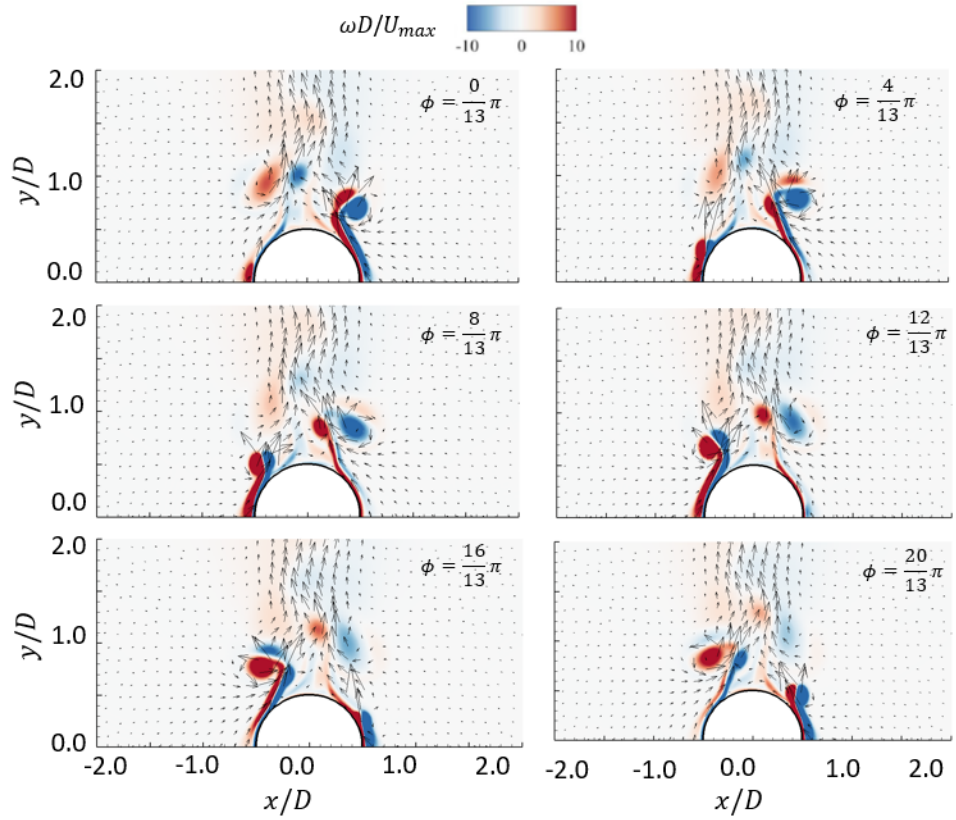

Figure 5.53: Velocity vectors over vorticity contours at $f = 10Hz, \tau = 0.5$

Figure 5.54 shows the time-accurate contours when frequency increases to $f = 40Hz$. At this frequency, the duty-cycle period becomes much shorter and the previous vortex can only travel a short distance before the next vortex is generated. As a result, the vortices are clamped together and two vortex trains are generated on both sides of the cylinder. The vortices slowly dissipate as they travel downstream and merge into one big jet. This jet is tilted to the left because the right jet on the right is much stronger than the left side jet on the left. As we can see from the chapter6 folder, the vortices are much smaller compared

to the cases at lower frequencies because the plasma actuation time in each period is much smaller, leaving no time to generate bigger vortices.

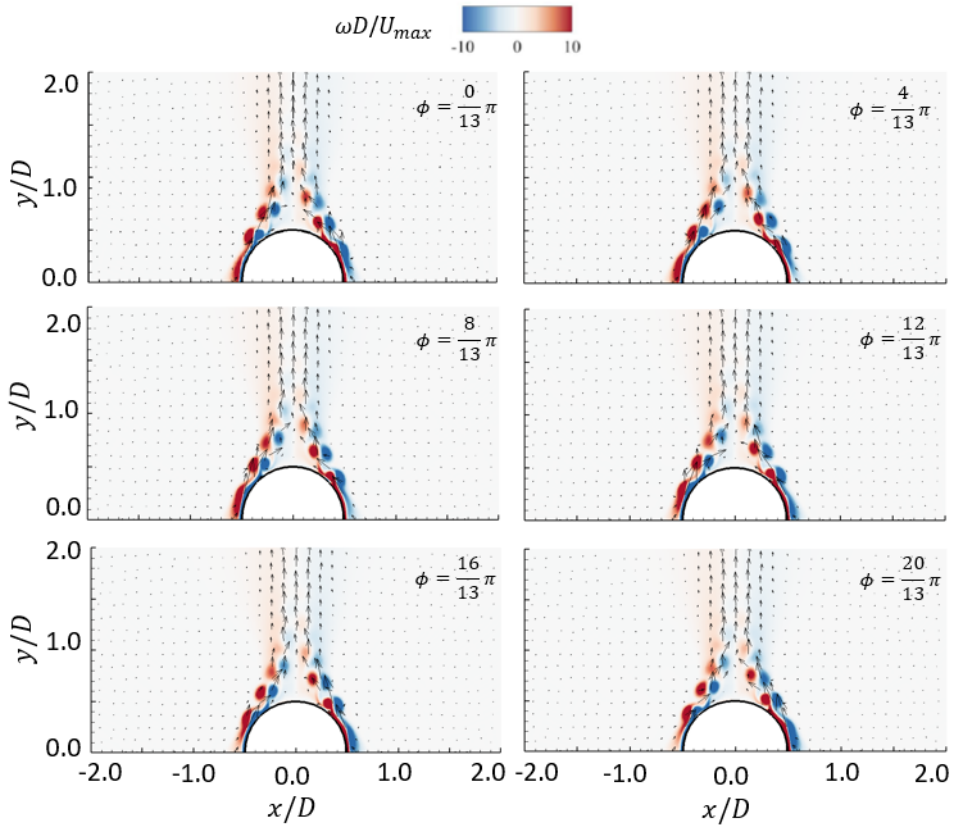

Figure 5.54: Velocity vectors over vorticity contours at $f = 40Hz, \tau = 0.5$

Figure 5.55 shows the time-accurate contours when frequency increases to $f = 60Hz$. At this frequency, the duty-cycle period becomes even shorter and the vortices in the wall jets start to lose their individuality and merge together. The combined jet is still tilted to the left just like the previous case but it becomes slightly narrower. The two vortex trains hug closer to the cylinder surface comparing to the $f = 40Hz$ case.

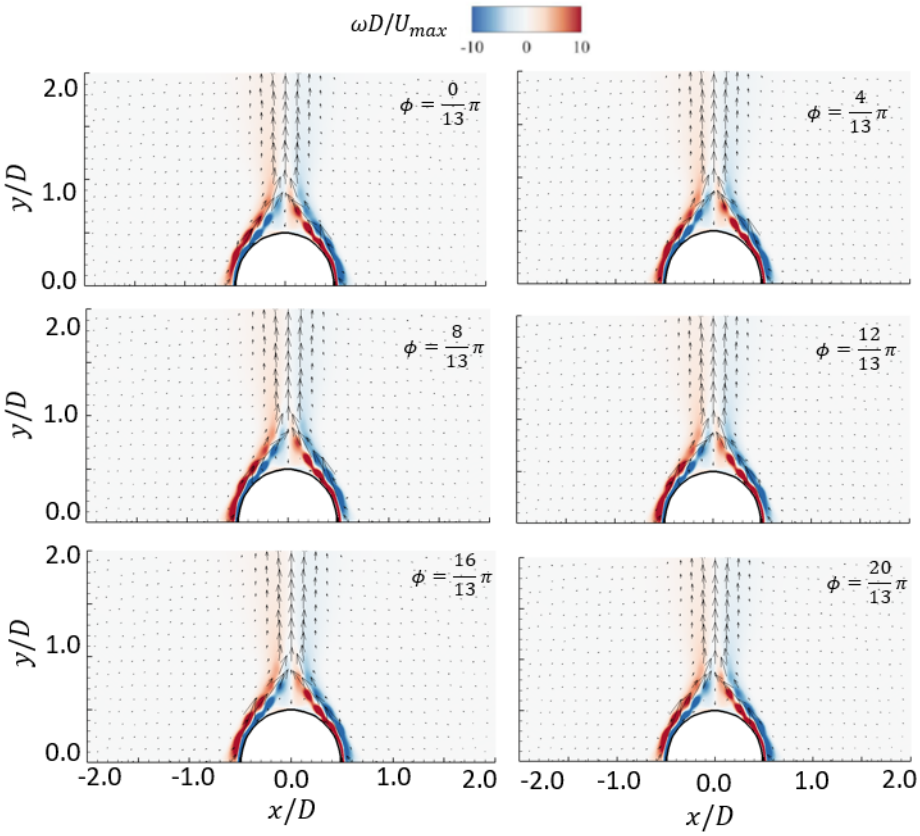

Figure 5.55: Velocity vectors over vorticity contours at $f = 60Hz, \tau = 0.5$

Figure 5.56 shows the time-accurate contours when the frequency increases to $f = 100Hz$. At this frequency, the individual vortices disappear completely and two wall jets are generated on both sides of the cylinder. Compared to $f = 60Hz$, the two jets hugs closer to the cylinder due to the Conda effect. When the duty-cycle frequency becomes this high, the flow field does not have time to react to the periodic change of the plasma actuation so the flow field no longer changes with the duty-cycle frequency. As a result, the results for $f = 200Hz$ is the same, as can be seen in Figure 5.57.

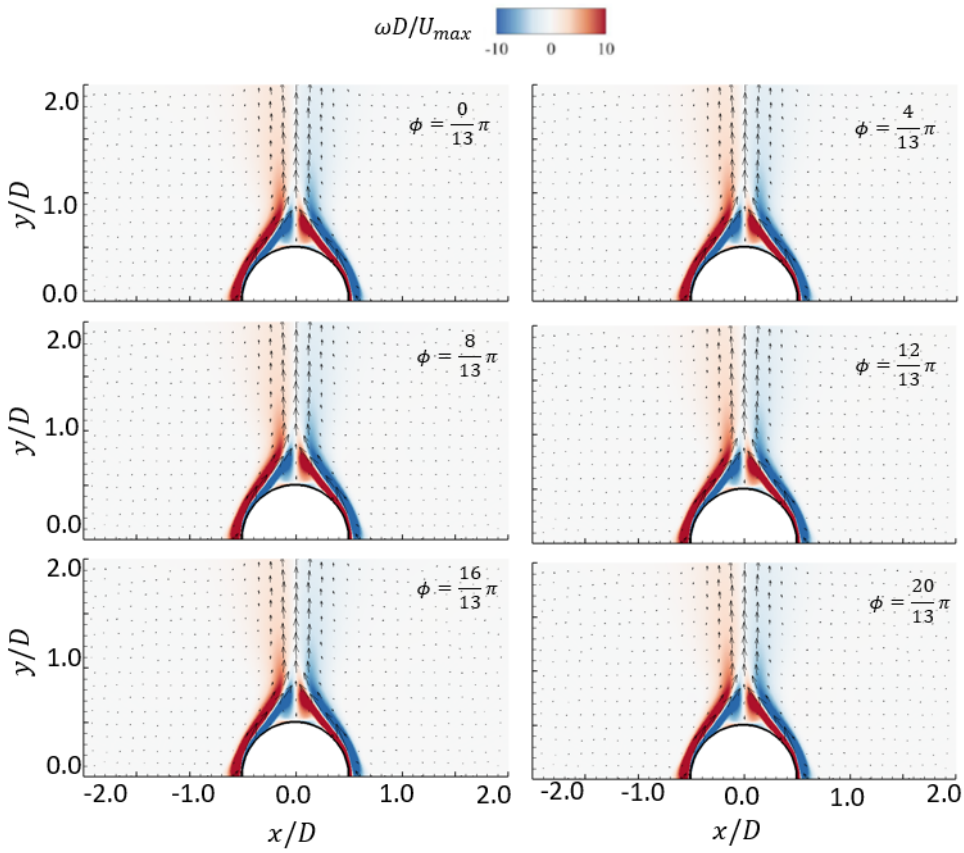

Figure 5.56: Velocity vectors over vorticity contours at $f = 100Hz, \tau = 0.5$

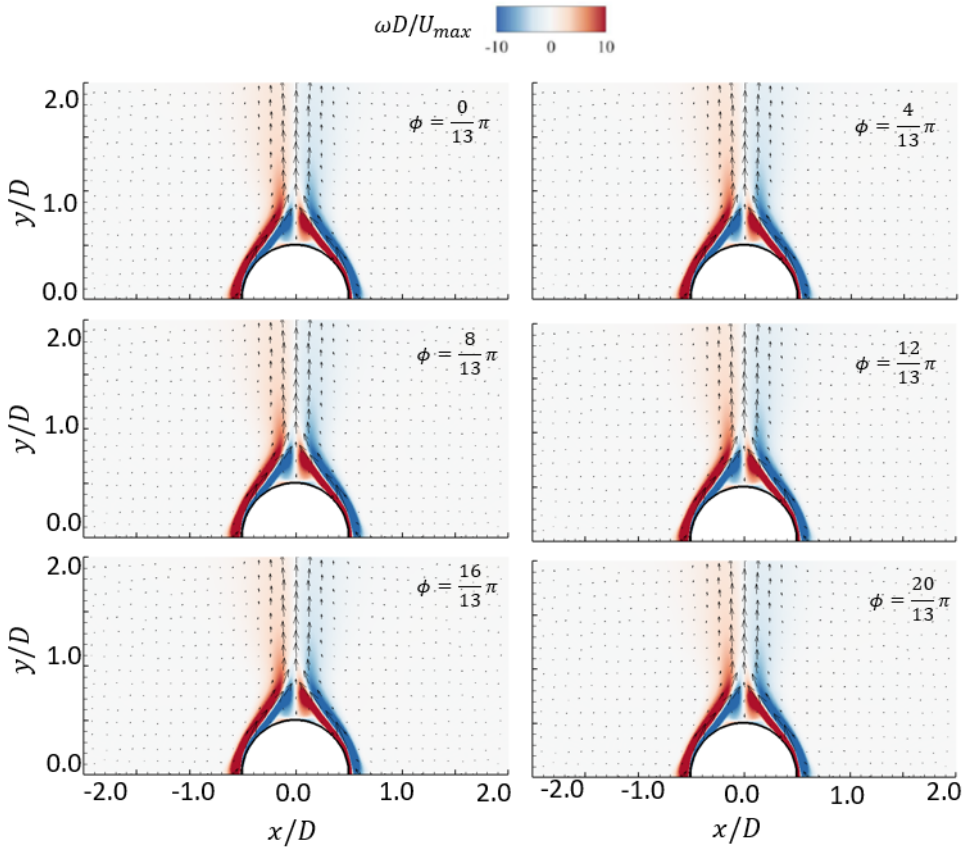

Figure 5.57: Velocity vectors over vorticity contours at $f = 200Hz, \tau = 0.5$

Figure 5.58 shows the time-accurate force and momentum when the duty-cycle ratio $\tau = 0.5$. The results are similar to the cases when $\tau = 0.3$, except for the fact that major changes happen at 50% of the period instead of 30% of the period.

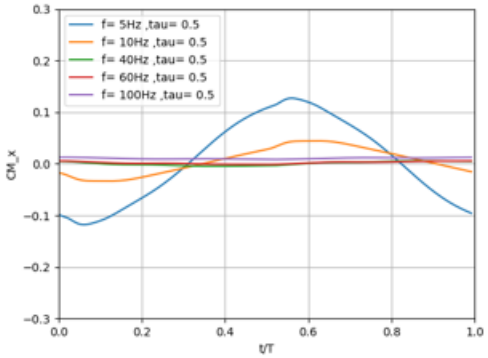

(a). X-momentum

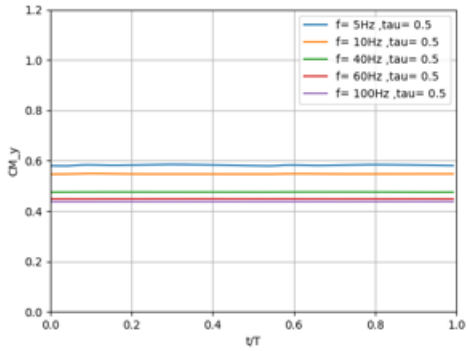

(b). Y-momentum

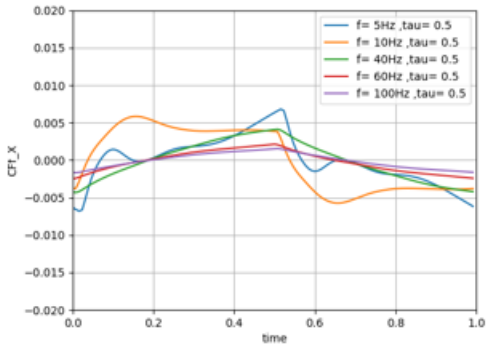

(c). Friction force in the x-direction

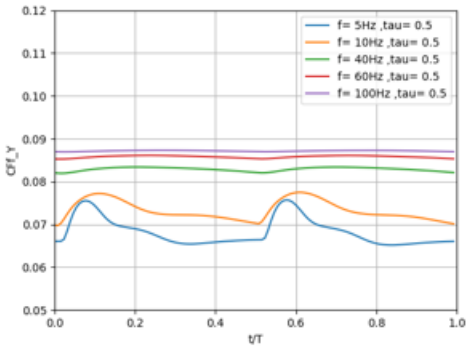

(d). Friction force in the y-direction

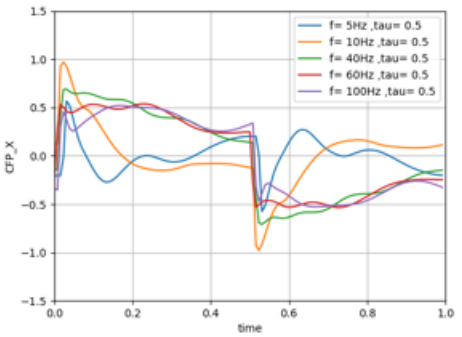

(e). Pressure force in the x-direction

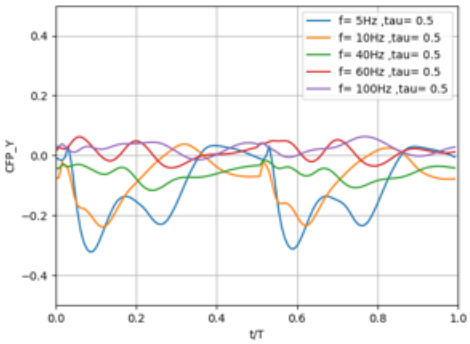

(f). Pressure force in the y-direction

Figure 5.58: Time-accurate force and momentum when $\tau = 0.5$

5.2.2.4 Time-accurate contours for different duty- cycle frequencies when duty-cycle ratio $\tau = 0.7$

Figures 5.59 to 5.63 show the time-accurate flow fields when the duty-cycle ratio $\tau = 0.7$ for different duty-cycle frequencies. Since the flow fields are the mirror images of the cases for $\tau = 0.3$, they will not be explained in detail.

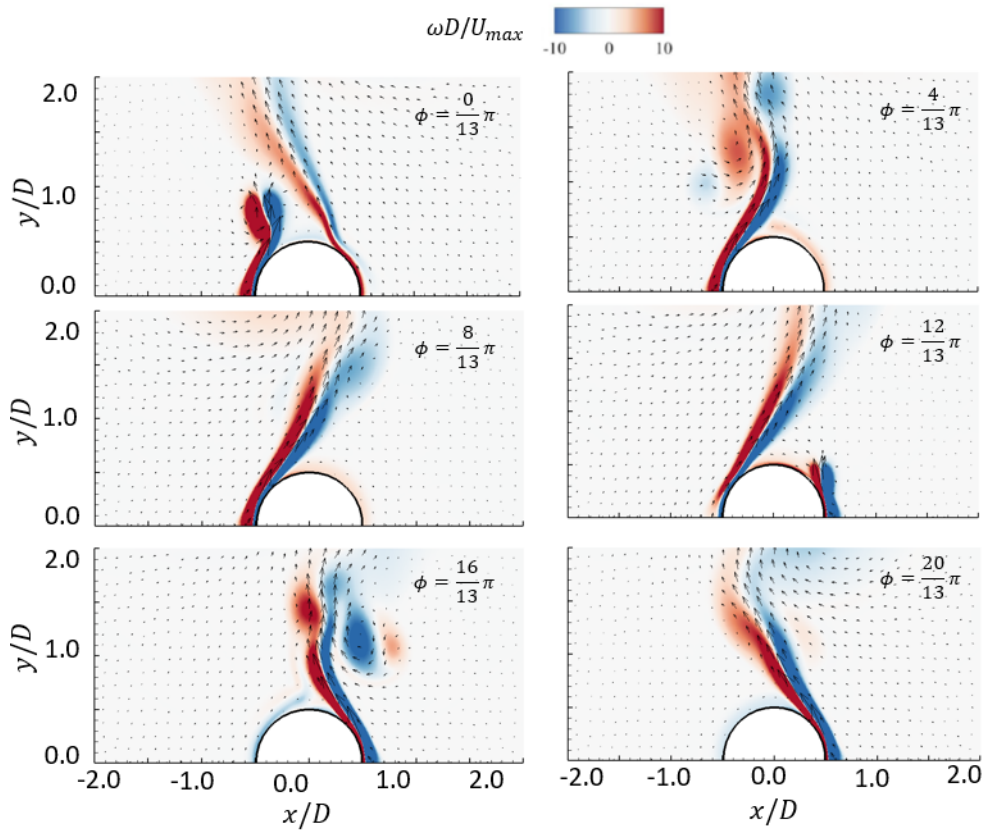

Figure 5.59: Velocity vectors over vorticity contours at $f = 1Hz, \tau = 0.7$

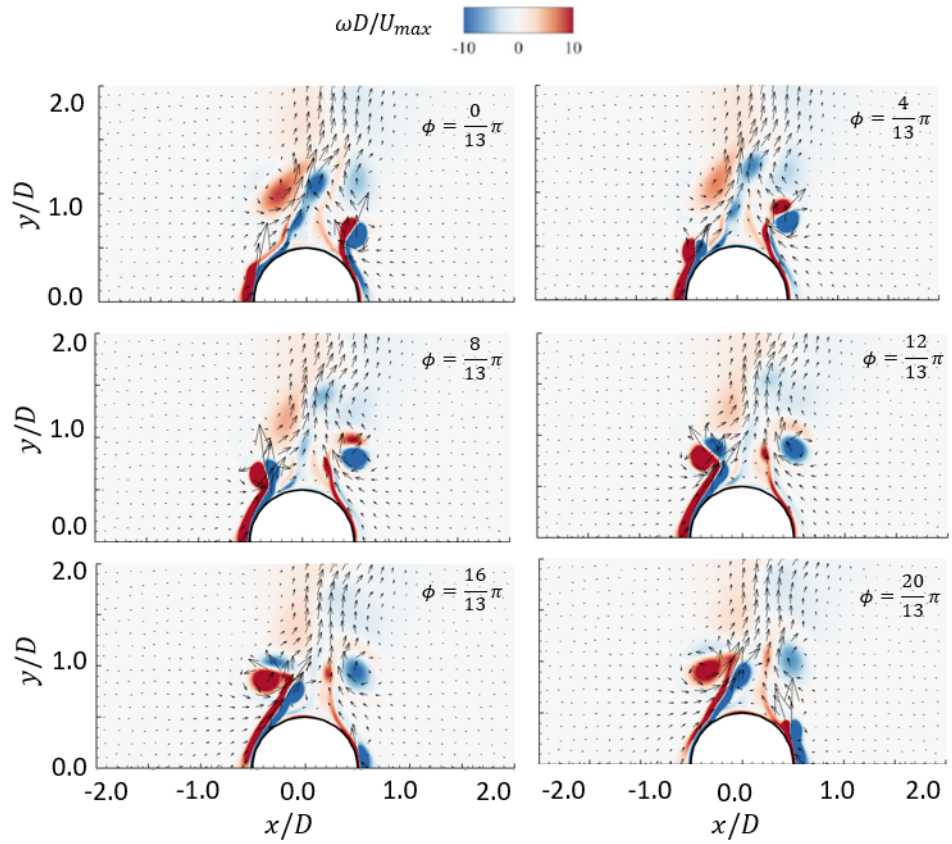

Figure 5.60: Velocity vectors over vorticity contours at $f = 10Hz, \tau = 0.7$

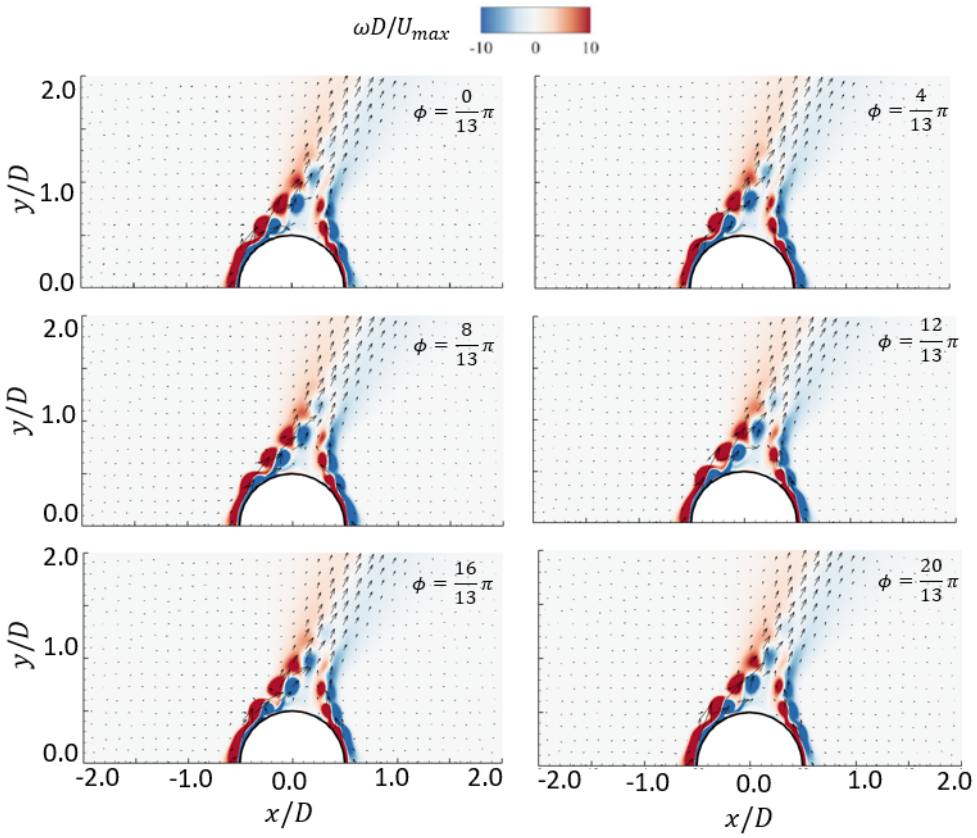

Figure 5.61: Velocity vectors over vorticity contours at $f = 40Hz, \tau = 0.7$

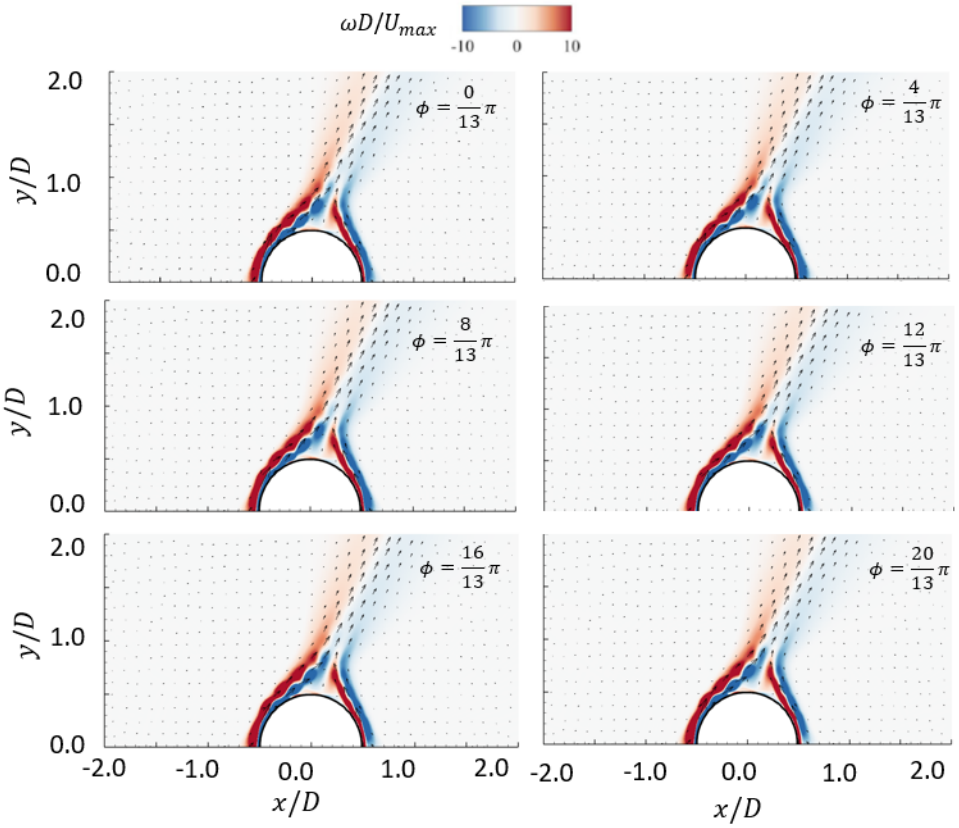

Figure 5.62: Velocity vectors over vorticity contours at $f = 60Hz, \tau = 0.7$

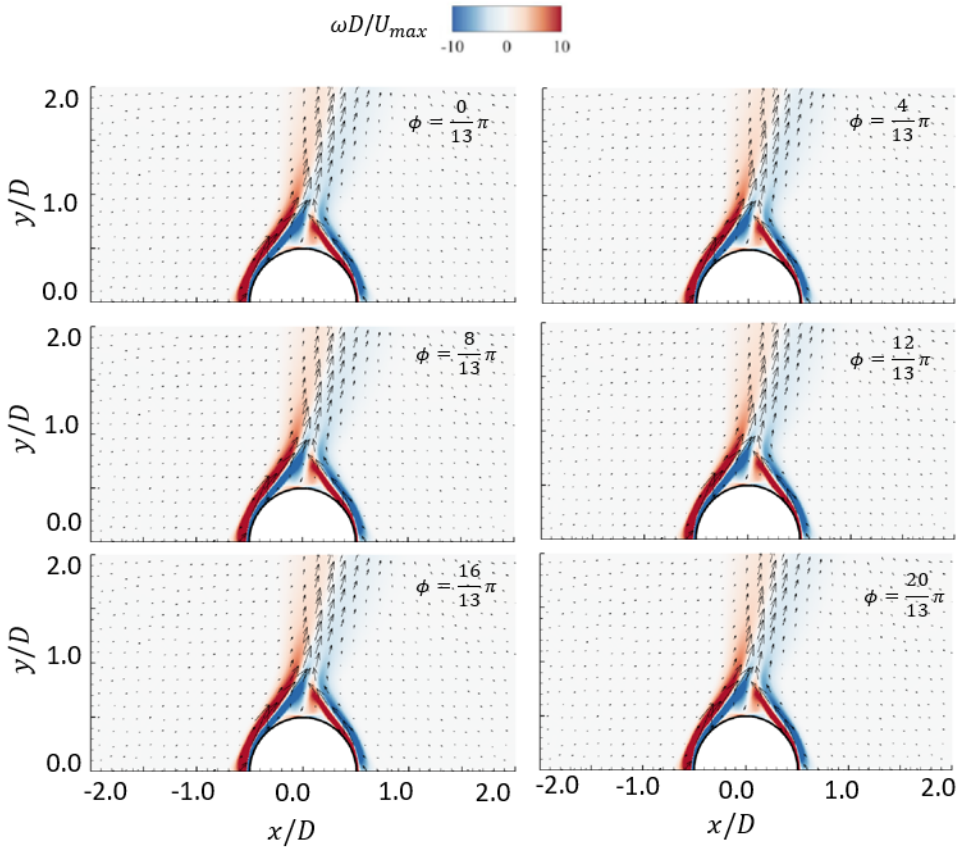

Figure 5.63: Velocity vectors over vorticity contours at $f = 100Hz, \tau = 0.7$

5.2.2.5 Vortex trajectory

Figure 5.64 shows the trajectories of the vortex cores under different actuation signals. For lower frequencies $f = 5, 10Hz$, both the simulated vortex trajectories and the experimental vortex trajectories are shown in the figure. For $f = 40Hz$, only the simulated vortex trajectories are shown because there are no experimental data available at this frequency. Beyond this frequency, the vortices start to lose their individuality and merge together, making it impossible to track the vortex trajectory. A vortex core is defined as the location of maximum vorticity within a vortex. For all frequencies, the vortex trajectory for $\tau = 0.3$ is tilted to the left while the vortex trajectory for $\tau = 0.5$ is symmetric. For lower frequencies, the trajectories are longer comparing to higher frequencies because the vortices under lower frequencies are much larger and harder to dissipate. Overall, the simulated vortex trajectories show good agreement with their experimental counterparts, once again providing validation for the fidelity of the simulation. However, we do notice that the simulated trajectories are shorter due to the simulated vortices dissipating faster. This is likely to be caused by the inaccuracy of the plasma body force model.

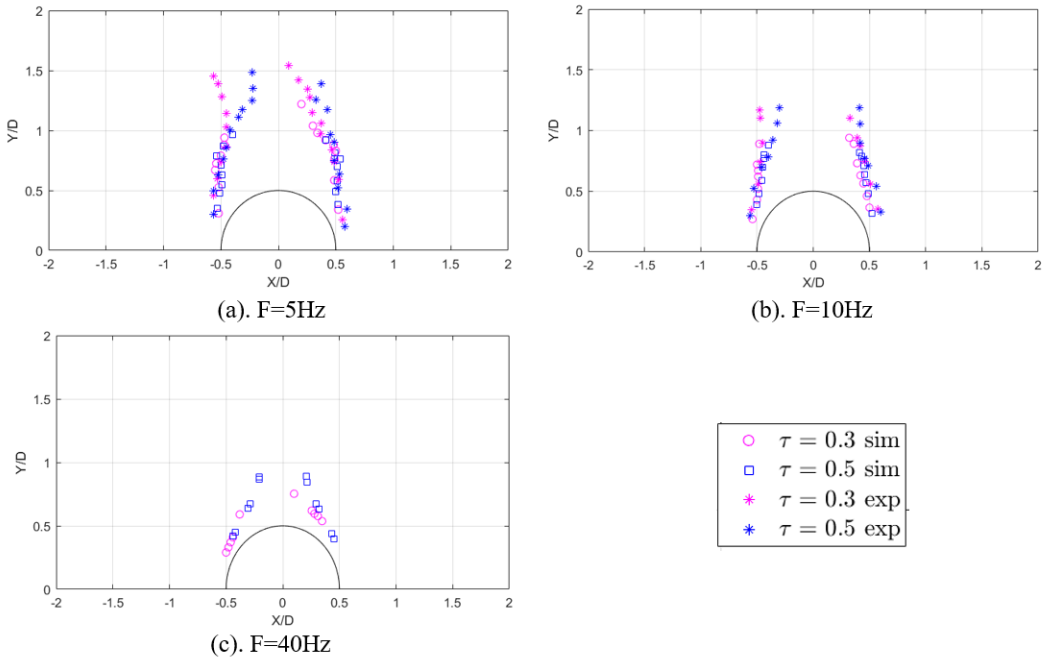

Figure 5.64: Vortex trajectories under different actuation signals

Chapter 6

Conclusions

The DBD plasma actuator has been identified as a very effective active flow control device with many advantages, such as being easy to install, fast acting capibilities and having no need for moving mechanical parts. Although many experimental researches have been done to investigate the plasma control effect, simulation methods still have their unique advantages. For example, simulations are usually cheaper and less dangerous comparing to experimental methods. They can capture high speed flow with better accuracy because they are not limited by the frequency of the camera. They can also simulate parameters that are hard to measure experimentally, such as the body force field and the pressure field away from the wall.

This research consists of three projects. In the first project, the flow field induced by the duty-cycle plasma actuation on a flat plate is simulated and compared with experimental results for validation and calibration purposes. The flow field is simulated by solving the Navier-Stokes equations with the SIMPLE algorithm while the plasma body forces are simulated by the Suzen and Huang's model. Essential parameters in this model are obtained by calibrating with experimental results. After obtaining the essential parameters, the simulated contours

show very good agreement with experimental contours. This project not only provides validation for the CFD code and the plasma body force model, but also provides essential parameters for high-fidelity simulation.

The second project studies the flow field around a square cylinder under plasma control. In the first step, the lift and drag coefficients as well as their Fourier transformation results are obtained and documented for Reynolds number ranging from 1 to 300. The flow field is steady for low Reynolds numbers and vortex shedding only starts to occur when $Re > 57$. These results are validated against the limited experimental and computational data in open literature. They serve as reference data for future research and as base data for flow control. After validating the code, a body force model for the DBD plasma actuator was coupled with the Navier-Stokes equation to study the effectiveness and the mechanisms of flow control by a pair of the DBD actuators. Three different cases are investigated, where the plasma actuators are installed in a different position in each case.

In Case 1, one DBD plasma actuator each was installed on the top and bottom surfaces of the cylinder, generating two jets parallel to the surfaces that could successfully reduce the fluctuations of both lift and drag. The flow experiences maximum reduction in fluctuation when the two actuators were installed at the end of the top and bottom surfaces. Although the fluctuations were successfully reduced, the increased velocities on the top and bottom surfaces significantly increased the skin friction drag on the cylinder surface. In Case 2, two actuators were installed on the front surface of the cylinder and two cross stream jets were induced on the front surface of the cylinder. These two jets increased the degree of flow separation at the two leading edge corners of the cylinder. As a result, the lift fluctuation and average drag coefficients were increased in this case, making it a failure.

In Case 3, two actuators were installed on the rear surface of the cylinder, inducing two jets running towards each other along the rear surface. These jets could reduce the unsteadiness and size of the separation vortices in the wake. Both the lift fluctuation and the average drag

coefficient were significantly reduced, making it the most effective case. The reduction of the average drag came mostly from the reduced pressure drag due to the increased stagnation pressure in the base region of the cylinder. In this case, the actuators did not increase the skin friction drag on the side surfaces of the cylinder. For a given location of the actuators, increasing actuator power decreased the lift fluctuation and average drag coefficient. The most effective configuration was for the actuators to be mounted near the top and bottom edges of the rear surface. With this configuration, it was possible to completely suppress the lift fluctuation when the power coefficient of the actuators was increased to 0.7 for $Re = 100$. However, completely suppressing the oscillations is impossible for $Re = 200$, when the flow suffered from separation on the top and bottom surfaces of the cylinder in addition to those at the trailing edges of the back surface. At higher Reynolds numbers, the lift fluctuation no longer increases when the power coefficient C_{pow} reaches 0.4 while the average drag continues to decrease due to the added kinetic energy of the flow from the plasma actuators. For both $Re = 100$ and $Re = 200$, the drag reduction efficacy η is always bigger than 1.0, indicating that the plasma actuator can always produce a net energy saving. The efficacy is also higher for $Re = 100$, indicating this device is more energy efficient for lower Reynolds numbers.

The third project studied the plasma induced flow field around a circular cylinder where a pair of DBD plasma actuators were installed symmetrically on the left and right sides of the cylinder. The flow field under both steady-state and duty-cycle actuation were studied in detail. The flow field was simulated by solving the Reynolds Averaged Navier Stokes (RANS) Equations with the SA one-equation model. The plasma body force was simulated by a model developed in our own lab, where the potential distribution was assumed to be linear and the net-charge density was calculated by solving the Gauss Equation. Three cases were simulated to study steady-state plasma control effect. In case 1, only the starboard actuator was activated. In case 2, only the port actuator was activated. In case 3, the actuators on both sides of the circular cylinder were activated simultaneously. For unsteady control, the duty-cycle frequencies range from $f = 1Hz - 200Hz$ while the duty-cycle ratios range from

$\tau = 0.01 - 0.99$. This paper provided three accomplishments. First, a high-fidelity body force model was created. Second, the velocity contours under different actuation signals were created and some of them were compared with experimental results for validation purposes. Third, the pressure distribution, shear stress distribution, velocity profiles and momentum in the observation window were studied in details.

For the starboard-on case, only the starboard actuator was activated, inducing a left running jet. When the duty-cycle ratio $\tau = 0.01$, the wall jet generated by the port actuator was almost negligible comparing to the wall jet generated by starboard actuator and the flow field was very similar to the starboard-on case. When the duty-cycle ratio increased to $\tau = 0.3$, the influence of the port actuator became much stronger and two wall jets were generated on both sides of the cylinder. These two jets merged into a bigger jet traveling in the upper left direction above the circular cylinder. When the duty-cycle ratio increased to $\tau = 0.5$, the flow field was similar to that of $\tau = 0.3$ except that the combined jet travels vertically upwards due to the equal actuation time on both sides. When the duty-cycle ratio $\tau = 0.7, 0.99$, the velocity contours were the mirror images of the velocity contours for $\tau = 0.3, 0.01$. All these velocity contours showed good agreement with experimental results.

The simulation revealed that the maximum time-averaged velocity increased with the duty-cycle frequency until $f = 100Hz$. The x-momentum is linearly dependent on the duty-cycle ratio τ and the y-momentum variation with τ takes a dome shape with its maximum at $\tau = 0.5$. The simulation results agreed mostly well with experimental results despite some minor differences. The differences were caused by the inaccuracy of the plasma body force model. The body force contour started right from the plasma actuator in the simulation but a distance away from the plasma actuator in the experiment. The body force in the experiment was able to generate bigger vortices comparing to the body force in the simulation and these vortices were able to bring more fluid upwards, inducing stronger y-momentum.

Apart from the discoveries already made in the experiment, this paper has made many new

discoveries as well. It is discovered that the time-accurate x-momentum took a dome shape with respect to time in one period, and the height of the dome decreases with duty-cycle frequency. The y-momentum shows much smaller oscillations throughout the entire period, almost negligible comparing to the oscillations in the x-direction. It is also discovered that the magnitude of the time-accurate pressure force is much larger than the magnitude of the time-accurate friction force, making the friction force almost negligible. The pressure force in one period is much more oscillatory than the momentum due to the mutual interaction between vortices near the circular cylinder. According to the Fourier transformation results at $f = 5Hz, \tau = 0.5$, the body force in the x-direction has multiple peaks with the maximum peak located at $f = 5Hz$. The momentum in the x-direction reflects the global changes in the flow field. It only has one peak at $f = 5Hz$ because the influence of weaker signals in the plasma body force are damped out in a global scale. The pressure and friction forces have several peaks at different frequencies. The peaks of the friction force are very similar to the peaks of the plasma body force and their phase differences are zero at every major frequency, indicating that the friction force can react instantly to the plasma body force. The peaks for the pressure force in the x-direction is much more complicated due to the mutual interaction between the vortices near the cylinder.

Although this research has made many amazing discoveries, there is still considerable room for improvement. The plasma body force model is based on a mathematical model instead of directly simulating the ionization process. Second, since we have been using a 2D code in the second project, higher Reynolds number flows cannot be studied due to the flow solver's inability to simulate the 3D turbulent effects. In the future, we plan to use a more accurate plasma model that can directly simulate the ionization process in air. We also plan to use a $3D$ flow field to simulate the plasma flow control effects at higher Reynolds numbers.

Bibliography

[1] A. Seshagiri, E. Cooper, and L.W. Traub. Effects of vortex generators on an airfoil at low reynolds numbers. *Journal of Aircraft*, 46(1), 2009.

[2] C.H. Bruneau and I. Mortazavi. Passive control of the flow around a square cylinder using porous media. *International Journal for Numerical Methods in Fluids*, 46, 2004.

[3] D. Gao, Y. Huang, and W. Chen. Control of circular cylinder flow via bilateral splitter plates. *Physics of Fluids*, 31, 2019.

[4] B. Smith and A. Glezer. The formation and evolution of synthetic jets. *Physics of Fluids*, 10(9), 1998.

[5] J. Donovan, L. Kral, and A. Gary. Characterization of a lorentz force actuator. *AIAA Journal*, 1997.

[6] J. Roth and X. Dai. Optimization of the aerodynamic plasma actuator as an electrohydrodynamic (ehd) electrical device. *44th AIAA Aerospace Sciences Meeting and Exhibit*, 2006.

[7] M. Taghizadeh, A. Ghaffari, and F. Najafi. Modeling and identification of a solenoid valve for pwm control applications. *Elsevier*, 2009.

[8] F. Giuliani, M. Stütz, N. Paulitsch, and L. Andracher. Forcing pulsations by means of a siren for gas turbine applications. *International Journal of Tubomechinery Propulsion and Power*, 2020.

[9] J. Wang, P. Liu, T. Qiu, and S Ding. An investigation into the flow of rotating orifices with euler angle and the calculation model of discharge coefficient considering the effect of comprehensive incidence angle. *Aerospace*, 2022.

[10] E.K. Straub, H.T. Ngo, V Anand, and D.B. Domzalski. Development of a piezoelectric actuator for trailing edge flap control of full scale rotor blades. *Smart Materials and Structures*, 1999.

[11] J.R. Roth and D.M. Sherman. Electrohydrodynamic flow control with a glow- discharge surface plasma. *AIAA Journal*, 38(7), 2000.

[12] M. Xue and C. Gao. "vortices induced by a dielectric barrier discharge plasma actuator under burst-mode actuation". *AIAA Journal*, 58(6), 2020.

[13] I. Moralev and V. Sherbakova. Effect of the discharge constriction in dbd plasma actuator on laminar boundary layer. *International Journal of Heat and Mass Transfer*, 116, 2018.

[14] X. Huang and X. Zhang. "streamwise and spanwise plasma actuators for flow- induced cavity noise control". *Physics of Fluids*, 20(3), 2008.

[15] Y. Wang and C. Gao. "simulation of flow around cylinder actuated by dbd plasma". *Physics of fluids*, 20(3), 2008.

[16] A. Singhal and D. Castañeda. "control of dynamic stall over a naca 0015 airfoil using plasma actuators". *AIAA Journal*, 56(1), 2018.

[17] Mazaheri K., Omidi J., and Kiani K.C. Simulation of dbd plasma actuator effect on aerodynamic performance improvement using a modified phenomenological model. *Computers and Fluids*, 140, 2016.

[18] T.C. Corke, C.L. Enloe, and S.P. Wilkinson. Dielectric barrier discharge plasma actuators for flow control. *Annual Review Fluid Mechanics*, 42, 2010.

[19] Pasquale L., Durante D., and Broglia R. Flow separation prevention around a naca0012 profile through multivariable feedback controlled plasma actautors. *Computers and Fluids*, 182, 2019.

[20] T.N. Jukes and K.S. Choi. Active control of a cylinder wake using surface plasma. *IUTAM Symposium on Unsteady Separated Flows and their Control*, 14, 2009.

[21] T.N. Jukes and K.S. Choi. Flow control around a circular cylinder using pulsed dielectric barrier discharge surface plasma. *Physics of Fluids*, 29, 2009.

[22] Kopiev V.F., Kazansky P.N., Kopiev V.A., Moralev I.A., and Zaytsev M Yu. Hf dbd plasma actuators for reduction of cylinder noise in flow. *Journal of Physics D: Applied Physics*, 50, 2017.

[23] R.D. Whalley and K.S. Choi. "the starting vortex in quiescent air induced by dielectric-barrier-discharge plasma". *Journal of Fluid Mechanics*, 703, 2013.

[24] L.X. Zhao, Z.L. Xiao, and F. Liu. Simulation of flow induced by single-dielectric- barrier-discharge plasma actuator using a high-order flux-reconstruction scheme. *Physics of fluids*, 33, 2021.

[25] Y. Anzai and K. Fukagata. Numerical simulation and sensitivity analysis of a low-reynolds-number flow around a square cylinder controlled using plasma actuators. *Physical Review Fluids*, 2017.

[26] W. Shyy, B. Jayaraman, and A. Andersson. Modeling of glow discharge-induced fluid dynamics. *Journal of Applied Physics*, 92(11), 2002.

[27] W. Hui, X. Meng, H. Li, and F. Liu. Flow induced by a pair of plasma actuators on a circular cylinder in still air under duty-cycle actuation. *Physics of fluids*, 34, 2022.

[28] C.L. Enloe, G.I. Font, T.E. McLaughlin, and D.M. Orlov. Surface potential and longitudinal electric field measures in the aerodynamic plasma actuator. *AIAA Journal*, 46(11), 2008.

[29] R. Erfani, H.Z. Behtash, C. Hale, and K. Kontis. Development of dbd plasma actuators: The double encapsulated electrode. *Acta Astronautica*, 109, 2015.

[30] R. Vidmar and K. Stalder. Air chemistry and power to generate and sustain plasma: Plasma lifetime calculations. *41st Aerospace Sciences Meeting and Exhibit*, 2003.

[31] J.P. Boeuf, Y. Lagmich, and T. Unfer. Electrohydrodynamic force in dielectric barrier discharge plasma actuators. *Journal of Physics*, 40, 2007.

[32] C.L. Enloe, T.E. McLaughlin, R.D. VanDyken, K.D. Kachner, E.J. Jumper, and T.C. Corke. Mechanisms and responses of a single dielectric barrier plasma actuator: Plasma morphology. *AIAA Journal*, 42(3), 2004.

[33] C.L. Enloe, T.E. McLaughlin, R.D. VanDyken, K.D. Kachner, E.J. Jumper, T.C. Corke, M. Post, and O. Haddad. Mechanisms and responses of a single dielectric barrier plasma actuator: Geometric effects. *AIAA Journal*, 42(3), 2004.

[34] D.M. Orlov, G.I. Font, and D. Edelstein. Characterization of discharge modes of plasma actuators. *AIAA Journal*, 46(12), 2008.

[35] W. Hui, X. Meng, H. Li, and F. Liu. Plasma discharges in atmospheric pressure oxygen for boundary layer separation control. *AIAA Fluid Dynamics Conference Exhibit*, 2005.

[36] Y.B. Suzen and P.G. Huang. Simulations of flow separation control using plasma actuators. *44th AIAA Aerospace Sciences Meeting and Exhibit*, 2006.

[37] B. Mertz and T. Corke. Single-dielectric barrier discharge plasma actuator modelling and validation. *Journal of Fluid Mechanics*, 669, 2011.

[38] H. Nishida1, T. Nonomura, and T. Abe. Numerical study of plasma dynamics and electrohydrodynamic effect in dbd plasma actuator. *International Journal of Plasma Environmental Science Technology,*, 10(1), 2016.

[39] McLaughlin T.E. VanDyken R.D. Kachner K.D. Jumper E.J. Corke T.C. Post M. Haddad O. Enloe, C.L. Mechanisms and responses of a single dielectric barrier plasma actuator: Geometric effects. *AIAA Journal*, 42(3), 2004.

[40] H.K. Versteeg and W. Malalasekera. *An Introduction to Computational Fluid Dynamics.* Bell Bain Limited, 1995.

[41] A. Jameson, W. Schmidt, and E. Turkel. Numerical solutions of the ruler equations by finite volume methods using runge-kutta time-stepping schemes. *AIAA 14th Fluid and Plasma Dynamics Conference*, 1981.

[42] M. Breuer, J. Bernsdorf, T. Zeiser, and F. Durst. Accurate computations of the laminar flow past a square cylinder based on two different methods: Lattice-boltzmann and finite-volume. *International Journal of Heat and Fluid Flow*, 21, 2000.

[43] A. Okijima. Numerical analysis of the flow around an oscillating cylinder. *Proceedings of the 6th International Conference on Flow-Induced Vibration*, 1995.

[44] Sohankar A., Noberg C., and Davidson L. Simulation of three-dimensional flow around a square cylinder at moderate reynolds numbers. *Physics of Fluids*, 11(2), 1999.

[45] C. Noberg. Flow around rectangular cylinders: Pressure forces and wake frequencies. *Journal of Wind Engineering and Industrial Aerodynamics*, 49, 1993.